



**UCGE Reports
Number 20179**

Department of Geomatics Engineering

Calibration of Airborne Laser Scanners
(URL: <http://www.geomatics.ucalgary.ca/links/GradTheses.html>)

by

Kristian Walker Morin

November 2002



UNIVERSITY OF CALGARY

Calibration of Airborne Laser Scanners

by

Kristian Walker Morin

A THESIS

SUBMITTED TO THE FACULTY OF GRADUATE STUDIES
IN PARTIAL FULFILMENT OF THE REQUIREMENTS FOR THE
DEGREE OF MASTER OF SCIENCE

DEPARTMENT OF GEOMATICS ENGINEERING

CALGARY, ALBERTA

November, 2002

© Kristian Walker Morin 2002

Abstract

This research details the calibration of a Leica Geosystems ALS40 airborne laser scanner (ALS). An ALS measures spot heights on the surface of the Earth for the purposes of deriving a Digital Terrain Model (DTM). To achieve consistent accuracy however, careful attention must be paid to the calibration of the system and the relationship of the components. Physical restrictions prevent the direct measurement of angular misalignment between the navigation and scanning components of an ALS, thus calibration parameters must be derived from the data. The primary goal of this thesis is to develop and implement a new calibration method for airborne laser scanners. The new method will address shortcomings in current manual methods by eliminating a need for ground control points, providing a rigorous stochastic model, modeling additional sources of error and improving the speed of a calibration. Using the presented methods, a calibration solution was calculated without ground control, with an elevation accuracy of 10cm.

Acknowledgement

I would like to express my gratitude to my supervisor Dr. Naser El-Sheimy. Through thick and thin he has been a kind mentor and continues to be an example of professionalism and dedication. Dr. Michael Chapman and Dr. Brian Ballantyne are also thanked for their guidance and a sympathetic ear during long conversations. Steve Barnett and Alex Osborne of TransCanada Pipelines are thanked for their early patronage of my research; and Scott Miller, Ron Roth and Paul Galla of Leica Geosystems are thanked for their much assistance over the past year.

To my friends and colleagues, much appreciation is given. Many thanks to Cameron Ellum my long time travelling companion through academia and lands abroad. Thanks to Lynn Raaflaub and DonnaLouise Watts for their patience while working next to me and for their endless amusements. Thanks to Peter Tate and Bruce Wright for their consultation and conversation.

Thanks are given to my family. To my Grandfather and Father, who both passed away during my studies, much love and gratitude is given for your guidance and care. To my Grandmother and Mother, I can never fully express my thanks or love – I simply would not be who I am without you.

Finally, to my love Sophia, endless gratitude is given for your companionship during late nights in front of the computer, your unremitting faith and your brilliant heart.

Table of Contents

Approval page.....	ii
Abstract.....	iii
Acknowledgement.....	iv
Table of Contents.....	v
List of Tables.....	vii
List of Figures.....	viii
Chapter 1 Introduction.....	1
1.1 Airborne Laser Scanners.....	2
1.2 Laser Scanning Applications.....	3
1.3 The Calibration Problem.....	5
1.4 Research Objectives.....	8
1.5 Thesis Outline.....	8
Chapter 2 Airborne Laser Scanner Design.....	10
2.1 Laser Scanner Components.....	10
2.1.1 Laser Ranging.....	10
2.1.2 Scanning.....	15
2.1.3 Control and Navigation Unit.....	20
2.2 Observation Models and Errors.....	21
2.2.1 Atmosphere Model.....	24
2.2.2 Clock Error.....	26
2.2.3 Scanner Error.....	26
2.2.4 Scanner Torsion.....	28

2.2.5	Encoder Latency	34
2.2.6	Navigation System	36
2.2.7	Integration Errors	39
2.3	Summary	39
Chapter 3	Calibration Methods.....	41
3.1	Pre-Flight Calibration	41
3.2	Post-Flight Processing	43
3.3	Proposed Method and Data Requirements.....	50
3.4	Observations and Flight Planning.....	55
3.5	Pseudo-Observations.....	59
3.6	Filtering the Data	61
3.6.1	Morphological Filters.....	62
3.6.2	Slope Based Filters	63
3.6.3	Least Squares Estimators	64
3.6.4	Filtering Consideration for Tie Point Selection	65
3.7	Summary	66
Chapter 4	Methodology	68
4.1	Test Data	68
4.2	Pseudo Observation Collection.....	72
4.3	Coordinate Systems	75
4.4	Observation Weighting.....	76
4.5	Solution Evaluation and Testing.....	78
Chapter 5	Results.....	81
5.1	Adjustment Solution: Boresight Angles Only	84
5.2	Adjustment Solution: Torsion with Fixed Angles	89
5.3	Adjustment Solution: Torsion and Angles.....	94
5.4	Terrain Effects	99
5.5	Summary of Results.....	103
5.6	Scanner Operating Parameters Effect on the Calibration Parameters	104
5.7	Remaining errors.....	106
Chapter 6	Conclusions and Recommendations	108
6.1	Conclusions.....	108
6.2	Specific Contributions	110
6.3	Future Investigations.....	111
References	113
Appendix A	Histogram Analysis Details.....	121

List of Tables

Table 2-1: Summary of ALS Errors.....	40
Table 5-1: Initial Tie Point Differences	82
Table 5-2: Calibration Solution for Angles Only	84
Table 5-3: Tie Point Differences Solving for Angles Only	85
Table 5-4: Torsion Solution.....	89
Table 5-5: Tie Point Differences with Torsion Correction.....	90
Table 5-6: Misalignment Solution with Angles and Torsion.....	95
Table 5-7: Tie Point Differences (Combined Solution).....	95
Table 5-8: Solution Comparison.....	103

List of Figures

Figure 1-1: Overlap Discrepancy Caused by Poor Calibration	5
Figure 1-2: Contour Generation in Overlapping, Mis-calibrated ALS Data	6
Figure 1-3: A Profile of an ALS Data Strip Exhibiting Bowing	7
Figure 2-1: Pulse and Continuous Wave Modulation.....	12
Figure 2-2: Multiple Echo from a Laser Signal.....	14
Figure 2-3: Constant Velocity Scan Pattern.....	16
Figure 2-4: Oscillating Mirror Pattern	17
Figure 2-5: Nutating Scanner Pattern	18
Figure 2-6: Elliptical Scanner Pattern.....	18
Figure 2-7: Scanner Angle and Distance Measurement	22
Figure 2-8: Intensity Image in a Forested Area,	23
Figure 2-9: Atmosphere Refraction	25
Figure 2-10: Scan Angle Encoder.....	27
Figure 2-11: Scan Mirror Components.....	28
Figure 2-12: Velocity and Acceleration of the Scan Mirror.....	29
Figure 2-13: Torsion on a Shaft.....	31
Figure 2-14: Component Lag.....	32
Figure 2-15: Scanner Error	33
Figure 2-16: Parabolic Effect of a Linear Angle Correction	34
Figure 2-17: ‘Bow Tie’ Effect from Latency Error	35
Figure 2-18: Misalignment Errors	38
Figure 3-1: Roll and Pitch Misalignment Plot over a Flat Surface.....	45
Figure 3-2: Strip Coordinate Frame.....	49
Figure 3-3: Effects of Roll Error on Overlapping Data	56
Figure 3-4: Effects of Pitch Error on Overlapping Data.....	57

Figure 3-5: Effects of Heading Error on Overlapping Differences	58
Figure 3-6: Optimal Flight Pattern for Calibration	59
Figure 3-7: Filtering Outlier Points.....	66
Figure 4-1: Intensity Image of Sitterdorf Airstrip and Surrounding Test Area	69
Figure 4-2: Colour Shaded Relief of the Test Area	70
Figure 4-3: Flight Line Layout	71
Figure 4-4: Attune Tie Point Selection	74
Figure 4-5: Attune Interactive Results.....	77
Figure 4-6: Surface Differences.....	79
Figure 5-1: Tie Point Distribution.....	82
Figure 5-2: Initial Control Point Difference Distribution	83
Figure 5-3: Profile of an Uncalibrated ALS dataset	84
Figure 5-4: Control Point Differences Distribution (Angle Solution Only).....	86
Figure 5-5: Distribution of Relative Elevation Differences Between Adjusted Laser Strips (Angle Only Solution).....	87
Figure 5-6: ALS Elevation Data Profile (Angle Only Solution)	88
Figure 5-7: Elevation Difference Plot - Angle Only Solution	89
Figure 5-8: Distribution of Control Point Differences (Torsion Correction)	91
Figure 5-9: Distribution of Relative Differences Between Adjusted Laser Strips (Torsion Correction)	92
Figure 5-10: ALS Elevation Data Profile (Torsion Correction)	93
Figure 5-11: Elevation Difference Plot - Torsion Only Solution	94
Figure 5-12: Distribution of Control Point Differences (Combined Solution).....	96
Figure 5-13: Distribution of Relative Differences Between Adjusted Laser Strips (Combined Solution).....	97
Figure 5-14: ALS Elevation Data Profile (Combined Solution)	98
Figure 5-15: Elevation Differences Plot - Combined Solution.....	99
Figure 5-16: Pulse Returns from Sloped Terrain.....	100
Figure 5-17: Elevation Differences of Flat Terrain	101
Figure 5-18: Elevation Differences Over Sloped Terrain.....	102
Figure 5-19: Remaining Error Effects	106

Chapter 1

Introduction

Although science fiction may lead us to believe that laser scanners have been around for decades, the modern airborne laser scanner has only reached commercial maturity in the past 10 years (Ackermann 1999). The need for a description of the Earth however, begins at the very beginning of civilisation. Archaeological evidence and ancient histories both record the attempts of people to change the lay of the land to achieve agricultural, urban and military goals (Williams 1987). Their efforts required surveys of the terrain, which became one of the cornerstones of modern engineering.

In current times the tools have changed, but many of the goals remain the same. The methods for creating terrain maps or models remained largely the same from ancient times until 150 years ago. The terrain was mapped out using a theodolite and a survey pole that gave relative displacement values from a series of known points. This process was slow and often details of the terrain were filled in by hand sketches and estimates. With the advent of cameras and photography in 1839 (Kraus 2000), a new science was born: photogrammetry. Early terrain measurements from cameras were taken of mountaintops to gauge their height, or conversely, from mountaintops to the ground to map out features. By taking two or more

photographs, a stereo-model can be generated which allows for the measurement of features or the ground surface in 3-dimensions. With the invention of the airplane, this survey method was naturally extended to the air and modern airborne photogrammetry began.

With relatively fast, wide area coverage, the formation of dense, accurate terrain models became technically and economically feasible. Improvements in manufacturing methods and photo measurement techniques resulted in terrain elevation accuracies greater than 30cm. Photogrammetry is not without its own drawbacks however. As a passive sensor, a camera is subject to the conditions of the atmosphere and the sun. Clouds, rain, fog, haze or any number of atmospheric phenomena delay or interfere with collecting photogrammetric data. Also, as technology improvements increased the collecting speed and decreased acceptable processing delays, the time involved to derive a terrain model from photos (ranging widely from days to months) often becomes too great. A need for a direct, active sensor became apparent.

1.1 Airborne Laser Scanners

Airborne laser scanners (ALS) provide accuracy, speed and ease of deployment. They are classified as active digital sensors in that: they emit energy and record a returned signal, and the recorded signal is immediately converted to a digital representation and stored directly onto a computer. As active sensors, they are not dependent on sunlight and can conceivably operate 24 hours a day. However many technical challenges needed to be overcome before an operating system would be feasible. Among these were the needs for precise positioning and aircraft attitude. Positioning was accomplished with the introduction of the Global Positioning System (GPS) in the 1980's – followed by further refinements that allowed centimetre level positioning (Strang and Borre 1997). Advances in Inertial Navigation Systems (INS) have slowly made their way from the military domain to the commercial - this provided the orientation requirements of the laser scanner (Schwarz 2000). Finally the modern laser ranging profiler was investigated at the Stuttgart University from 1988-1993

(Ackermann 1999). It showed high accuracy ranging potential and further development introduced opto-mechanical components to provide scanning ability. Since that time several commercial ventures have created airborne laser scanning units. The most prominent are the ALTM scanner series from Optech Inc (Canada), the ALS40 sensor from Leica Geosystems (formerly the AeroScan from Azimuth Inc. USA) and the TopoSys sensor from TopoSys Inc (Germany).

1.2 Laser Scanning Applications

Given its application proximity to photogrammetry, it is clear that one of the primary uses of ALS systems would be to generate surface terrain models. ALS observations can have much more dense point spacing than is typically derived from photogrammetry; with current systems abilities exceeding 1 point / metre. Frequently ALS data is used to derive contour maps, despite the approximate nature of such a map. The raw or filtered observations are generally more accurate and more detailed than a contour representation. Thus previous Digital Elevation Model (DEM) applications such as hydrological modelling can be improved with the higher quality of data (Brandt and Vosen 2000, Cavazzini et al. 2000, Pereira and Wicherson 1999, Favey et al. 2000, Murtagh and Foote 1999, Briese and Pfeifer 2001, Brugelmann 2000, Roper 1999). Other common uses of DEMs include applying them in photogrammetry in order to rectify imagery (Kraus 1997, Flood and Gutelius 1997, Morin and El-Sheimy 2001-2). In addition, hyper-spectral sensors may benefit from an accurate terrain model that can be used to rectify the hyper-spectral data (Niemann 2002). A new but already common application of DEM data is visibility analysis. This can be used by the communications industry to help determine the best location for line-of-sight transmitters (Hill et al. 2000, El-Sheimy 1999), and urban planning applications to project the impact of new building structures on light distribution in dense urban areas, or impact of urban vistas (Mass and Vosselman 1999, Haala and Brenner 1997, Murakami and Nakagawa 1999, Haala and Brenner 1999, Masaharu and Hasegawn 2000, Geibel and Stilla 2000, Berg and Ferguson 2001, Che and Nakane 2001, McIntosh, Krupnik and Schenk 2000).

In addition to view sheds, ALS data can be used to derive features from the terrain. This is possible due to the hyper-dense nature of ALS observations. Depending on the size of buildings and the flight characteristics, buildings can often have hundreds of points observed along their roofs and potentially along their sides. This permits a 3-dimension modeling of the structure. When combined with imagery or existing urban GIS data, highly precise models of cities can be created (Axelsson 1999, Murakami 1999, Haala 1999, Maas 1999, Haala and Brenner 1997, Murakami and Nakagawa 1999, Haala and Brenner 1999). This application was grimly demonstrated in September 2001, when ALS data was used to survey and analyze the debris at the World Trade Centre site in New York City (Williamson and Baker 2002).

In addition to ‘block’ structures, ALS data has a unique ability to detect narrow linear features such as roads and rail lines (Gutelius 1998, Berg and Ferguson 2001, Hill, Graham and Henry 2000). Of particular note is the ALS ability to measure electrical transmission lines. This is possible because the power line, despite being small, has a very high reflectance with respect to laser energy. In addition to interacting with the power line, the transmitted energy can continue past the power line and reflect off of the ground. This multiple return feature of ALS systems permits accurate modeling of power lines with respect to the ground, and measurement of the transmission towers. The data can be used by transmission companies to determine the ‘health’ of the line and to track encroachments into the transmission right-of-way such as overgrown trees (Terrasolid 2002).

The multiple return ability of an ALS system can be leveraged to great benefit when applied to biometric analysis. This kind of analysis is usually in reference to forests, but can also include river flood plains and costal regions. In the forest context, the laser energy is transmitted towards the forest and will often hit the top of the tree canopy. Due to a designed divergence of the laser beam however, the signal will have a small footprint (depending on flying height: at 500m many systems have footprints of 30cm – Leica Geosystems 2002).

The gaps in the leaves allow the signal to continue to pass through the tree. In some cases the signal penetrates all the way to the forest floor. Thus with dense data, the observation set will describe the top and shape of the tree canopies and the forest floor. Measuring the ground in forest regions has always been difficult for photogrammetry due to the lack of visibility between the trees. The top and bottom information however permits the derivation of additional information including tree species determination, volume, health and the ability to count trees (Elberink and Maas 2000, Hyyppa J et al. 2000, Kraus and Reiger 2000, Kraus and Pfeifer 1998, Popescu and Wynne 2000, Samberg and Hyyppa 1999, Weishampel et al. 2000, Ziegler et al. 2001). This new data can then be integrated with existing data sources to supplement existing methods, and eventually supplant them.

1.3 The Calibration Problem

Data integration can only occur if the products are spatially consistent. A frequent problem with ALS data is that it shows systematic shifts in elevation and horizontal position when compared to other data sources, such as map products, and systematic differences between overlapping sections of data from the same sensor. Although random errors exist in all sensor measurements, systematic types of errors are largely due to an incorrect or incomplete calibration. With ALS systems, the most offending parameters are the misalignment between the navigation and laser components. The effects of the errors are illustrated in Figure 1-1.

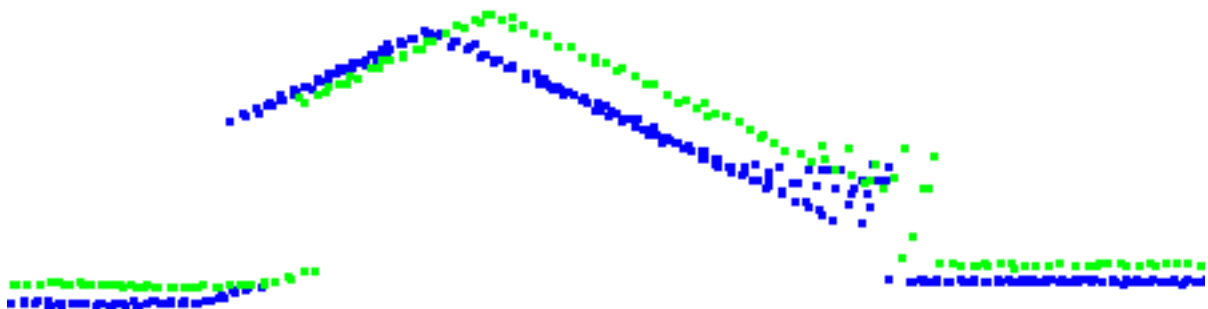


Figure 1-1: Overlap Discrepancy Caused by Poor Calibration

Figure 1-1 shows a cross-section profile of a building that was in an overlapping scan area. The different flight lines (shown in green and blue) show that the building appears shifted from one flight line to the other and the ground is not consistent. When using feature extraction on the data, the misalignment of the two strips will cause errors to result in the products derived from ALS data.

When viewed from above, the overlapping areas of strips can be seen by the higher density of points on the ground. When determining the ground in the overlap area however, the elevation discrepancies mask where the true ground may lie. This can be illustrated by generating contours (Figure 1-2).

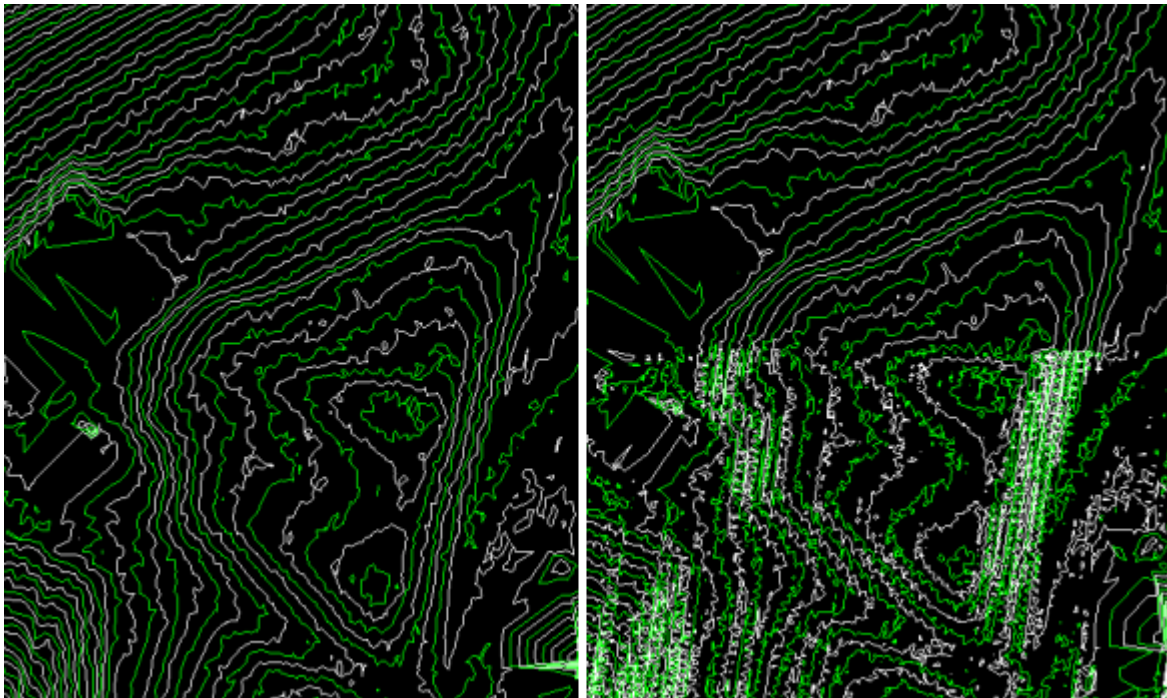


Figure 1-2: Contour Generation in Overlapping, Mis-calibrated ALS Data

The overlapping area (right image, bottom half) shows jagged and confused contours, whereas the strips by themselves (left image) show smooth and regular contours. For

applications such as terrain modeling or forest biometrics, such inconsistencies can make it impossible to derive accurate information. Thus, without a proper calibration, ALS data is handicapped.

The most common calibration method used in industry is a simple manual adjustment of the misalignment angles (Morin and El-Sheimy, 2002). Although practical, this method is time consuming, biased prone and requires ground control. Data derived from this method is often quoted with an accuracy of 15cm (Baltsavias 1999-2). Despite shortcomings, this method of calibration has been effective enough to identify an additional source of error: a bowing distortion in the across track direction of the scanner data (Figure 1-3).

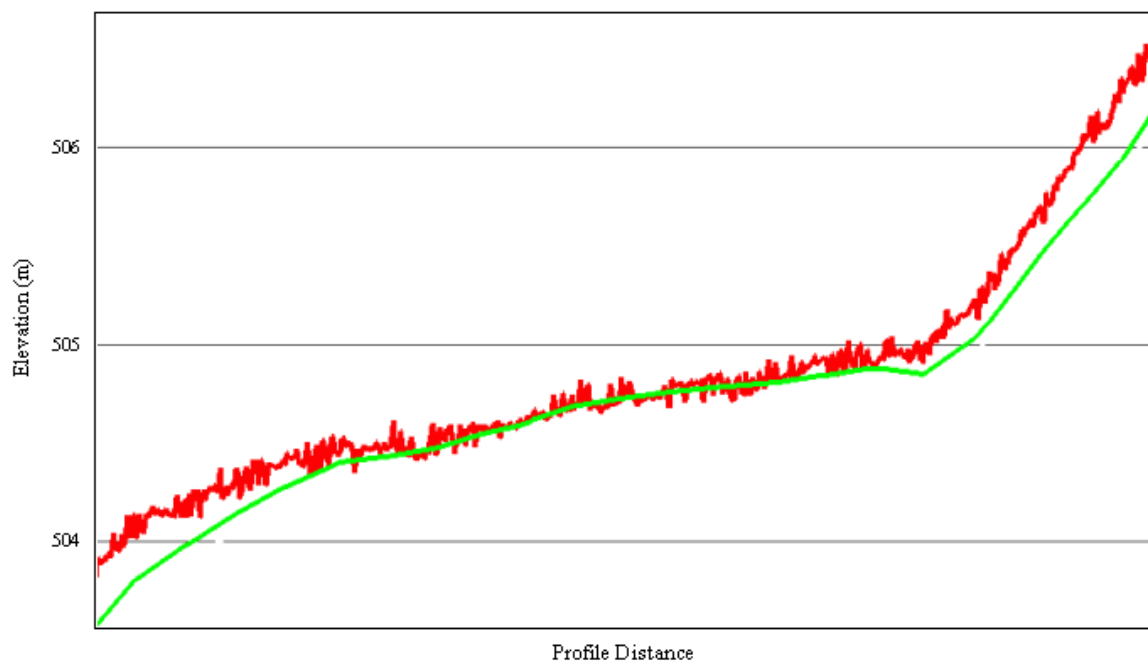


Figure 1-3: A Profile of an ALS Data Strip Exhibiting Bowing

Figure 1-3 shows an across track profile of ALS data over a known surface. The ALS data (red) rises above the known surface (green) at the edge of the scan, but appears consistent with the known surface in the middle. This type of error appears to be caused by a

systematic effect in the scan angle measurement. Other methods of ALS calibration have been proposed (Burman 2000-1, Crombaghs et al. 2000, Vosselman and Mass 2000, Morin and El-Sheimy 2001-1), but none to date have addressed this source of error.

1.4 Research Objectives

The primary goal of this thesis is to develop and implement a new calibration method for airborne laser scanners. The new method will address shortcomings in current manual methods by eliminating a need for ground control points, providing a rigorous stochastic model, modeling additional sources of error and improving the speed of a calibration. The calibration parameters arising from the new method will allow for laser strip vertical consistency of less than 0.15m. This vertical consistency will thus be an improvement over current methods derived from lengthy manual adjustments. By modelling new systematic errors, the solution will improve over existing methods as well.

With a fast and reliable calibration method, sensor parameters can be checked more frequently. This allows for more consistent data capture from the sensor, and can permit further study on the effects of calibration parameters and time. The increased accuracy from the improved calibration will also allow more reliable analysis of ALS derived data such a terrain models and forest biometric information.

1.5 Thesis Outline

The focus of this research is centred on the mathematical modeling of the airborne laser-scanning sensor measurements and the effects of error. In Chapter 2, the ALS sensor is described and broken into its components with an analysis of error sources. Although all sensor types are described, the focus is on ALS systems with opto-mechanical scanning mirrors (the most common type). Chapter 3 describes calibration methods for the sensor

components, and for their integration. In this chapter the sensor model for the new calibration method is described.

In Chapter 4 the calibration methodology is described. This includes an analysis on the effects of flying pattern on derived ground points and an optimal flight plan for calibration purposes. Chapter 5 lists the results from the calibration methods that were tested, demonstrating an improvement with the new method. Results are given using a comparison of check points and relative consistency. Chapter 6 completes the analysis with conclusions. Specific contributions and areas for future investigations are suggested.

Chapter 2

Airborne Laser Scanner Design

Airborne Laser Scanners combine several surveying technologies. While there are differences between commercial systems, the basic package remains the same: a Global Positioning System (GPS) receiver and an Inertial Navigation System (INS) as the navigation component, and a laser range finder and a scanner as the remote sensing component (Wehr and Lohr 1999). Each component requires calibration and the relationship between the components needs to be determined.

2.1 Laser Scanner Components

2.1.1 Laser Ranging

The laser ranging unit contains the laser transmitter and the receiver. The two units are mounted so that the received laser path is the same as the transmitted path. This ensures that the system will detect the target it illuminates. The target size or footprint of the laser is a function of the flying height of the platform and the divergence of light ray. The divergence

of the light thus defines the instantaneous field of view (IFOV) of the sensor. For a spatially coherent beam of laser light, the IFOV is typically between 0.3 mrad to 2 mrad (Wehr & Lohr 1999). At a flying height of 500 metres, this will result in a laser footprint of 30 cm in diameter on the ground.

Most commercial laser rangefinders employed in ALS systems operate in the 1100 – 1200 nm wavelength range (near-infrared). This is due to the common availability of lasers in that wavelength (Wehr and Lohr 1999). The transmitted energy interacts with the target surface and permits the derivation of range and reflectance measurements. The intensity of the reflected near-infrared signal can be used to form an image of the measured area. Objects with high reflectivity such as retro-reflective paint or cement contrast distinctly with objects of low reflectivity such as coal or soil. Near-infrared has the disadvantage however, of having poor penetration of water; thus making bathymetric measurements unreliable. To achieve water penetration, a blue-green laser is used (Optech 2002). The depth of penetration is a function of water turbidity and motion, but cannot exceed the normal penetration of blue-green light (~50 metres) (Optech 2002).

To obtain a range measurement from a laser, the transmission must be modulated. There are currently two methods of modulating a laser beam for ranging: pulse modulation and sinusoidal continuous-wave (CW) modulation (Baltsavias 1999, Wehr & Lohr 1999) (Figure 2-1).

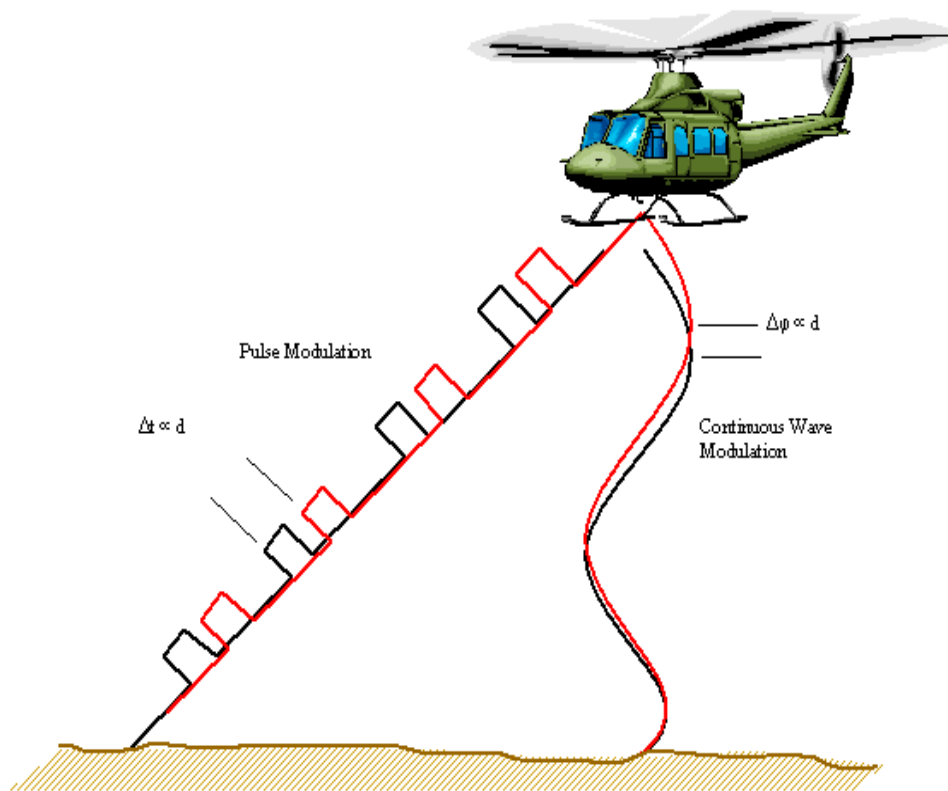


Figure 2-1: Pulse and Continuous Wave Modulation

With pulse modulation the transmitter generates a rectangular pulse with widths from 10-15ns (Wehr and Lohr 1999). The time difference between the pulse when it leaves the transmitter and is detected in the receiver is proportional to the returned distance, i.e.:

$$t = 2 \frac{D}{c} \quad (2-1)$$

where:

- t is total elapsed time
- D is the path distance or range of the pulse
- c is the speed of light

The path will be affected by atmospheric distortion and will be a function of the off-nadir scan angle and current weather conditions. The rectangular pulse that exits the laser ranger interacts with the Earth's surface and returns a complex signal. Most commercial systems analyse the signal for the first peak, which is then used to determine the distance. It has been found however, that the signal shape can convey information about the target properties; specifically vegetative properties (Hofton and Blair 2000). Some ALS systems store the shape of the returned pulse; however due to the much larger data storage and real-time processing requirements, these types of systems are not used for high density terrain height measuring.

A single modulated pulse also has the ability to reflect off multiple targets in its line of sight. This is most commonly seen over forested areas. The gaps between the leaves and branches allows some of the pulse to reflect off the upper layers, while additional energy transmits and reflects to lower layers (Figure 2-2). This feature allows ALS systems to take direct measurements of the ground's surface in forested regions. To distinguish the components of a multiple echo in the returned signal, the signal shape must contain a fall and a second rise. The second rise must be a certain distance away from the first in order to be distinguished from the initial echo. In commercial systems the minimum pulse separation is usually 2-3 metres (Leica 2002). Commercial systems can currently measure up to 5 echoes per pulse; but in practice it is unusual to receive more than 3 returns (Leica 2002).

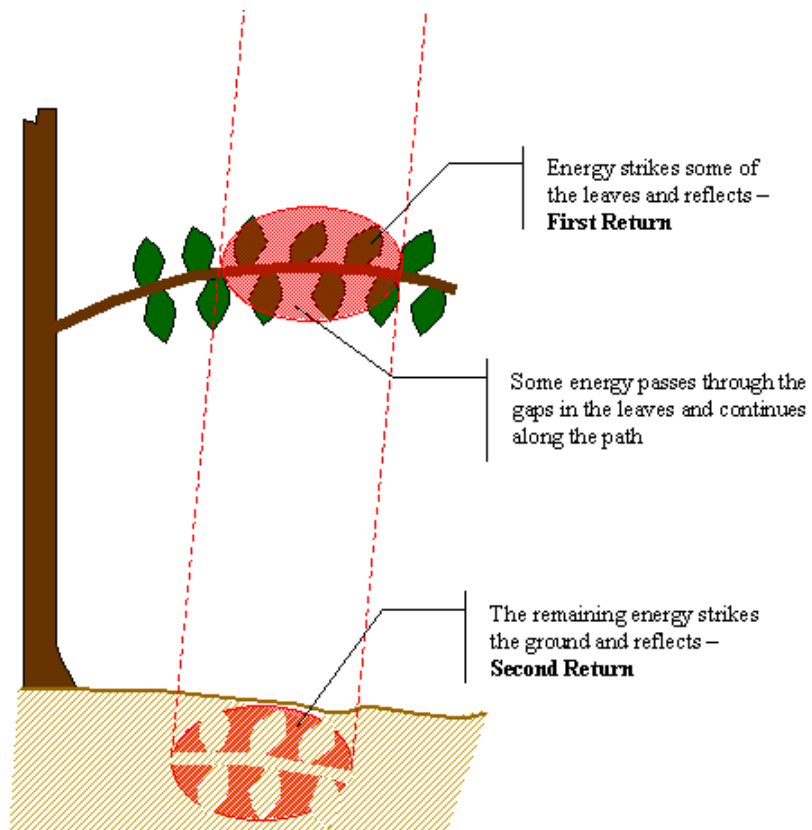


Figure 2-2: Multiple Echo from a Laser Signal

Continuous wave (CW) modulation employs a transmitter to emit a continuous light wave at a set frequency. The phase difference of the received light wave is proportional to the travel time and thus to the range, i.e.:

$$t = \frac{\phi}{2\pi}T + nT \quad (2-2)$$

where:

- t is the total elapsed time
- ϕ is the phase difference of the returned wave
- T is the period of the modulated wave
- n the number of full wavelengths included in the distance from the transmitter to the receiver

In practise, pulse modulated lasers are used much more often than CW; including all current commercial systems. This has to do with the commercial availability of pulse laser rather than any technical advantage (Baltasvias 1999). In terms of absolute accuracy, high frequency pulsed systems are dependent on how accurately the time difference can be measured (Baltasvias 1999). For centimetre measurements this current technology suffices, but sub-centimetre measurements still pose a large problem. In contrast, CW systems can obtain sub-centimetre accuracy by increasing their modulated frequency. In practice though, frequency modulated lasers are not widely available.

2.1.2 Scanning

To perform a scan of an area, the laser beam must be moved. This is achieved with rotating mirrors or other means to provide across track scanning, and the motion of the platform to provide along track scanning. The total across-track scanning angle defines the swath width or field of view (FOV). In practice commercial systems typically have FOVs from 20 to 30 degrees (Wehr and Lohr 1999) although systems with FOVs up to 75 degrees are available (Leica Geosystems 2002).

There are several scanning techniques employed in different ALS systems. The first is the use of a constant velocity-rotating mirror. This type of scanner produces measurements that appear as parallel lines on the ground (Figure 2-3). The mirror is rotated in one direction by a motor and the angle measured either directly from the motor or from an angular encoder directly mounted to the mirror. The advantage of this system is that the constant velocity does not induce any acceleration type errors in the angle observation. The primary disadvantage is that for a certain amount of time during each mirror rotation, the mirror is not pointing at the ground and observations cannot be taken. This can be partially addressed by using a mirror with multiple sides; but there will always be a time period where the laser

ranger must be stopped, or measurements discarded. The constant velocity mirror also restricts the FOV of the sensor, which makes the sensor less adaptable.

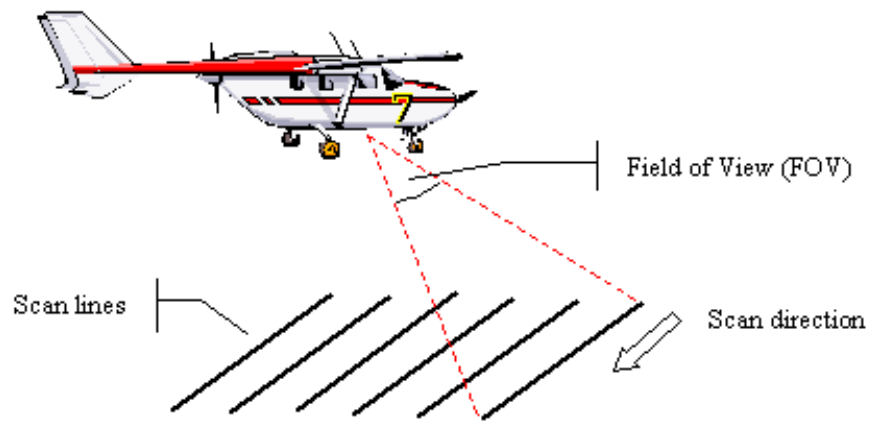


Figure 2-3: Constant Velocity Scan Pattern

A more popular method of scanning is to use an oscillating mirror. Companies such as Optech, Leica Geosystems and TopEye, who constitute a large portion of the commercial ALS market, employ this method. With this technique the mirror rotated back and forth. This has the effect of creating a 'Z' or zigzag line of points on the ground (Figure 2-4). The advantage of this method is that the mirror is always pointing towards the ground; so data collection can be continuous. The user can generally control the mirror's field of view and scan rate. There are several disadvantages however. The changing velocity and acceleration of the mirror cause torsion between the mirror and the angular encoder. The changing velocity also implies that the measured points are not equally spaced on the ground. The point density increases at the edge of the scan field where the mirror slows down, and decreases at nadir.

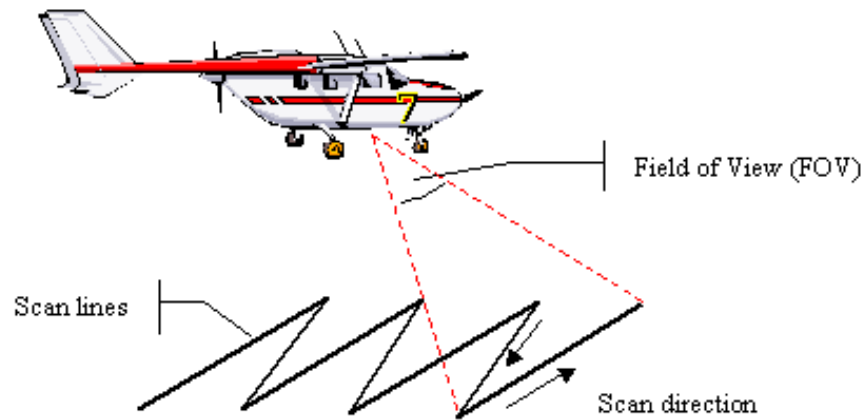


Figure 2-4: Oscillating Mirror Pattern

An additional advantage of the oscillating mirror is an ability to compensate for aircraft motion. With all forms of ALS scanners, the scan pattern on the ground shows the effects of the aircraft motion (particularly roll). The edges of the scan are ‘wavy’ (caused by roll) and areas of the scan field can appear compressed (caused by pitch). For mission planning, this is problematic because excessive aircraft motion can create gaps in the target measurement area. Oscillating mirrors can be integrated with the real-time output of the INS system to correct for roll type errors. As the aircraft rolls in one direction, the scanner control hardware module compensates the motion resulting in a more stable scan pattern.

Another method of scanning is with the use of a fibre-optical array (TopoSys 2002). Rather than moving a mirror to direct the laser onto the ground, a small nutating mirror is used to direct a laser into a linear fibre-optical array. The array transmits the pulse at a fixed angle onto the ground (Figure 2-5). The advantage of this system is that with fewer and smaller moving parts, the scan rate can be greatly increased. These systems typically have a sufficient scan rate such that points overlap in the along track position. A disadvantage is that the FOV is currently much smaller than a rotating mirror (± 7 degrees) and the across track positions are fixed. Thus the only variable is the aircraft flying height.

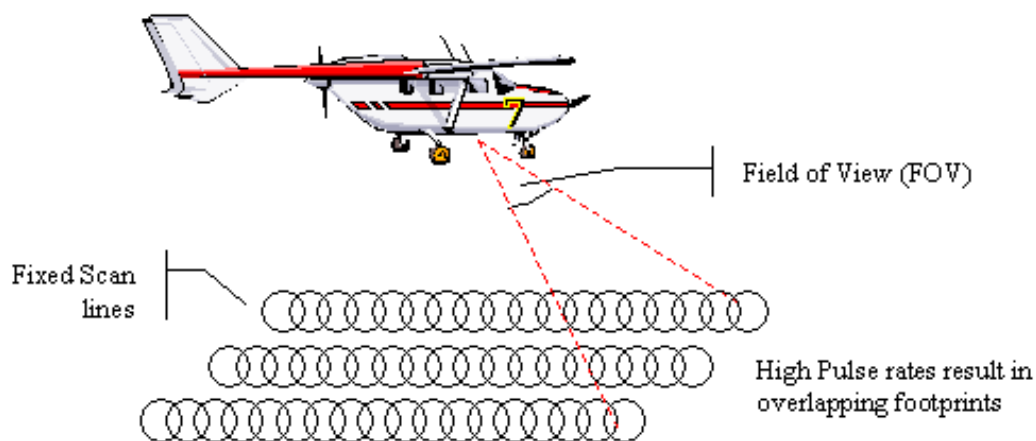


Figure 2-5: Nutating Scanner Pattern

The last scanning method is the Palmer or elliptical scanner. The system employs two mirrors to move the laser along an elliptical path around the aircraft (Figure 2-6). The advantage of this system is that the ground is often measured twice from different perspectives, thus allowing areas that were occluded on the first pass to be measured on the second. Disadvantages include the increased complexities of two mirrors plus the uncertainties that two angular encoders would have on a derived point location. This method was used in the ASLRIS system (Hu, Xue, Fang and Pan 1999).

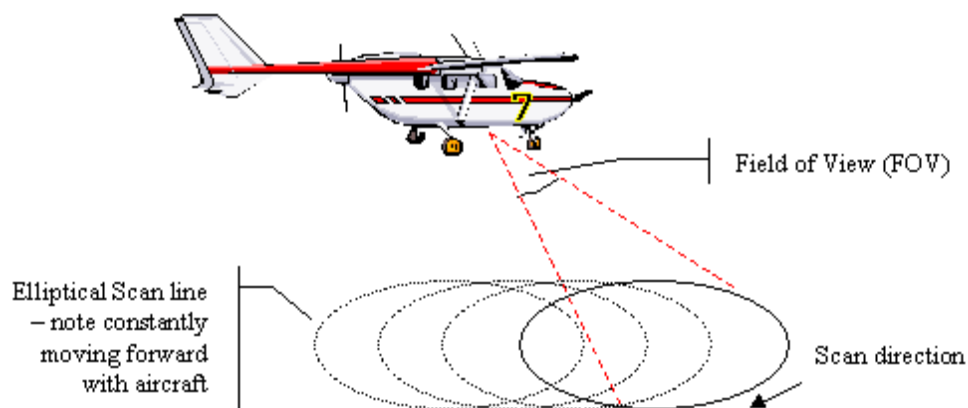


Figure 2-6: Elliptical Scanner Pattern

Due to undulating terrain and different methods, most scanners results in a random distribution of laser range measurements on the ground. Although the ground point spacing is not deterministic, they follow a general shape of the scanning mechanism; thus they are pseudo-random. The across-track point spacing is a function of flying height and ranging frequency. The along track point spacing is also dependent on flying height, scan rate and flying speed. For oscillating scanners, the most common, a system operating at 500 metres above the ground flying at approx 70 m/s with a scan rate of 25 lines/sec and a pulse rate of 18 kHz, the point density is approx 1.6 points / m². The point spacing is summarized by (Baltsavias 1999),

$$N = F/f_{sc} \quad (2-3)$$

$$SW = 2h \tan\left(\frac{\theta}{2}\right) \quad (2-4)$$

$$dx_{along} = v/f_{sc} \quad (2-5)$$

$$dx_{across} = SW/N \quad (2-6)$$

where:

- N is the number of points per scan line
- F is the scan frequency
- f_{sc} is the number of scan lines per second
- SW is the swath width
- h is the flying height
- θ is the FOV of the scanner
- dx_{along} is the along track point spacing
- v is the forward velocity of the aircraft
- dx_{across} is the across track point spacing

2.1.3 Control and Navigation Unit

The scanner and the laser ranger are linked together by the control unit. This unit typically drives the laser ranger and the mirror galvanometer. Timing is controlled by an internal clock. The internal clock is synchronized with GPS time by the use of a Pulse Per Second (PPS) signal generated by GPS receiver internal clock. Each measurement is tagged with a value from the internal clock. The tags are then referenced to the PPS and each combined range and angle measurement is assigned a GPS time tag.

The navigation unit on a modern ALS system is composed of a differential GPS system and an attitude sensor. Most systems employ an INS unit to determine the attitude (Krabill et al 2000, Vaughn et al 1996). The features of the INS (attitude determination, high data rate, e.g. often 200Hz) neatly complement the features of a DGPS system (fairly low data rate 2-10 Hz, high positional accuracy). Together they provide highly accurate and stable navigation information. Among commercial systems, the Applanix navigation system is often used for the navigation unit (Leica Geosystems 2002, Optech 2002, Mostafa and Hutton 2000). The individual sensor measurements then go into the observation model to form the target coordinates.

2.2 Observation Models and Errors

To determine the target coordinates, the data from the laser ranger, scanner and navigation unit must be combined. The basic observation equation is,

$$r_i^m = r_{nav}^m(t) + R_b^m(t) [R_S^b \cdot r^S + a^b] \quad (2-7)$$

where:

r_i^m	coordinates of laser target (i) in the mapping frame (m-frame)
$r_{nav}^m(t)$	coordinates of the combined navigation sensors in the mapping frame
$R_b^m(t)$	the interpolated rotation matrix from the navigation body frame (b-frame) to the mapping frame
R_S^b	rotation from body frame to the scanner frame (s-frame) to the body frame
r^S	laser vector from scanner in s-frame
a^b	coordinate offsets between the b-frame and the s-frame, measured by the user during system setup

Equation 2-7 describes the general computation for a target. The laser vector varies depending upon the type of scanner used. For example, in the case of a constant velocity or oscillating mirror, the laser vector equation would be,

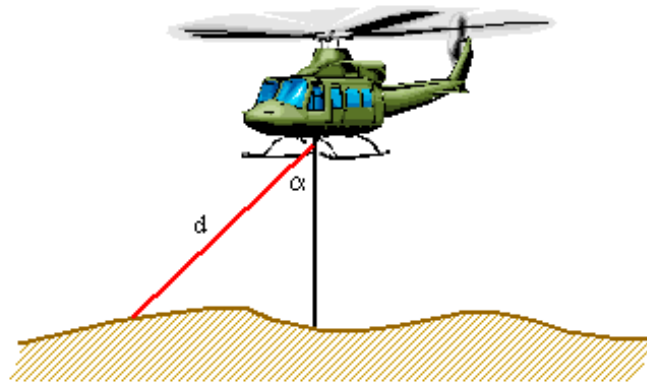


Figure 2-7: Scanner Angle and Distance Measurement

$$r^S = \begin{pmatrix} -d \cdot \sin \alpha \\ 0 \\ -d \cdot \cos \alpha \end{pmatrix} \quad (2-8)$$

where,

- d raw laser range (distance) in laser frame
- α scanner angle from nadir along y-axis of laser frame
- r^S laser vector in scanner frame

Once the relationship between the observations is expressed, we can begin looking at how individual errors contribute to the accuracy of the target coordinate. Errors can be broken down into their system components of the laser range finder, GPS, INS, systems synchronization and the command and control module.

The distance, (d), is generated in conjunction with an internal clock. This clock becomes a potentially significant source of error in the laser unit if not accounted for. These errors are manifested as modulation and timing problems. In a pulsed system, the pulse must be generated at a specified time. If there is an uncalibrated delay, the time difference will be

propagated into the distance calculation (Baltsvias 1999). Further, if the modulation is altered, either in shape of pulse or the frequency of the wave, the receiver will have problems detecting the returned signal. This would give rise to a measurement outlier, i.e. a range value that would be significantly different than its neighbours.

A more common receiver problem would be detecting a weak target. For example, a typical pulsed laser will transmit its pulse at a peak power of 2 kW; for a 750 m path the received power is only 2.4×10^{-6} W (Baltsvias 1999). Different targets exhibit various reflectivity behaviors at the infrared frequency commonly used by commercial systems. The power of the reflected signal is also a function of the terrain angle. The effect is visible over forest areas where leaves at random angles result in a wide range of reflected power levels (Figure 2-8).



Figure 2-8: Intensity Image in a Forested Area,

Many materials have a fairly low reflectivity. For this reason a laser signal detector is usually configured to expect the signal shape of a weak return. Some materials such of retro-reflective paint however, have a very high reflectivity. The power of their returned signal is very high and can saturate a laser detector that is looking for very weak signals. The effect on the ground points is usually manifested by very bright points appearing to ‘hover’ above the surrounding terrain; and is commonly referred to as ‘range walk’. To compensate for it, commercial systems implement an automatic gain control on the laser detector. High powered returns cause the detectors gain to ramp down, thus allowing for a more accurate measurement (Leica Geosystems 2002).

2.2.1 Atmosphere Model

The laser range is also affected by atmospheric errors. Like any light ray, the laser signal is refracted as it moves through the air. The amount of refraction is a function of wavelength, attitude, scan angle and atmospheric conditions (Kraus 2000). Commercial ALS manufactures tend to keep their atmospheric refraction models proprietary; but their corrections would be similar to the standard atmosphere model used in photogrammetry (Chapman 1996) and shown in Figure 2-9, i.e.:

$$\Delta\alpha = K \cdot \tan \alpha \quad (2-9)$$

where,

$$K = \left(\frac{2410H}{H^2 - 6H + 250} - \frac{2410H}{h^2 - 6h + 250} \left(\frac{h}{H} \right) \right) \times 10^{-6} \quad (2-10)$$

where,

- h elevation of ground above datum
- H elevation of scanner to datum

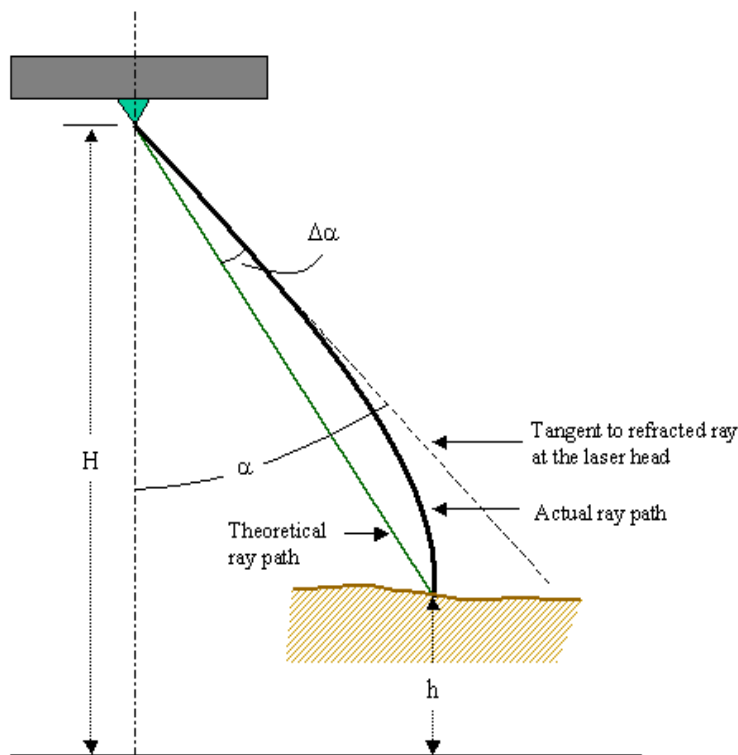


Figure 2-9: Atmosphere Refraction

Atmospheric refraction causes the laser beam to curve along its path. The amount of deflection ($\Delta\alpha$) is proportional to the scan angle. It reaches a maximum at the edge of the scan and zero for a nadir scan. The correction value, K , is a constant based on a standard atmosphere model (Equation 2-10 is the ARDC (U.S. Air Force) model (Chapman 1996), and the scan angle. In addition to the angle correction, the distance the pulse travels along the curved path is different from the theoretical path. To determine the theoretical path (which must be used in the point calculations), a correction must be made to the observed range. The correction will vary as a function of the scan angle and the atmospheric conditions (gradient index of the atmospheric refraction coefficients (Suson 2002)).

The received power of the range signal is further reduced by poor atmospheric conditions such as dust or smoke. Mission planning becomes important to reduce these kinds of errors. However, if a small amount of energy were to reach the receiver through backscatter or other

means, then the target would be incorrectly identified. In a properly functioning system working in good atmospheric conditions however, these types of errors are more likely to occur at random intervals, which could be filtered in a post-process step from the data.

2.2.2 Clock Error

A persistent timing problem in an ALS system would be the clock measurement error in a pulsed system that detects the pulse transmission time. For a path distance of 1500 metres (750 m transmit and return), the time delay would be 5×10^{-6} s. A 1% error in the clock (5×10^{-8} s) would result in a range error of 7.5 metres. Fortunately all commercial systems are much more accurate with typical accuracy between (0.05 ns and 0.2 ns) (Baltasvias 1999). This corresponds to a laser ranging accuracy of 1.5 cm. Depending on the pulse rate, clock drifts and biases may come into account. If present, they can be modeled during the calibration set-up (Krabill et al. 2000). The ultimate resolution of a pulsed laser range finder is determined by its ability to measure the time of the returned pulse, i.e.:

$$d_r = 0.5 \cdot c \Delta t \quad (2-11)$$

where:

- d_r is the range resolution
- Δt is the returned pulse time

With systematic errors removed, the common accuracy of ALS laser range finders taking measurements from 500 metres above ground level is 1.5 – 2cm (Leica 2002, Optech 2002).

2.2.3 Scanner Error

An obvious source of error in the scanner is the measurement of the scan mirror rotation angle. Several factors influence this measurement, the primary being the measurement method. The mirror's position is controlled by a galvanometer, and conversely the mirror's

position can be measured directly from the galvanometer. Such measurements systems have shown accuracies of approx. 0.02 degrees (Baltsavias 1999). A galvanometer measurement does not offer the highest accuracy however. To achieve improved results, a separate encoding device can be attached to the mirror. These angle encoders allow a measurement accuracy of 0.001 degrees (Leica Geosystems 2002). But a separate encoder introduces other sources of error.

Typically an encoder consists of a glass disc with regular etchings. A small laser similar to a grocery store checkout scanner is used to measure the etch marks on the glass (Figure 2-10). If the encoder is not mounted exactly perpendicular to the mirror's rotation angle, then the glass etches will have a projection error. Although this projection error can be modeled, in practice it is usually adjusted by modifying the relationship between the tick readings and the total number of ticks on the glass disc. Although the glass disc has a known and fixed number of etch marks, the misalignment projection causes the spacing between them to appear to change. By altering the total number of ticks per full revolution in the scanner model, the errors can be effectively eliminated.

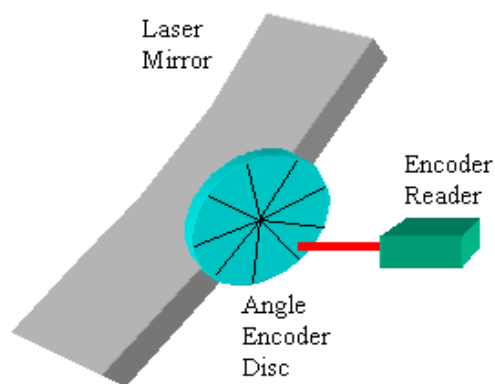


Figure 2-10: Scan Angle Encoder

2.2.4 Scanner Torsion

In addition to the encoder projection errors, there are also errors caused by the changes in velocity and acceleration that are associated with oscillating mirrors in general. The effects of this type of error on the derived ground point, as described in Chapter 1, is to produce a bowing along the across track profile of an ALS strip (Figure 1-3). In order to explain this phenomenon, it is best to explore the construction of the scanner in more detail.

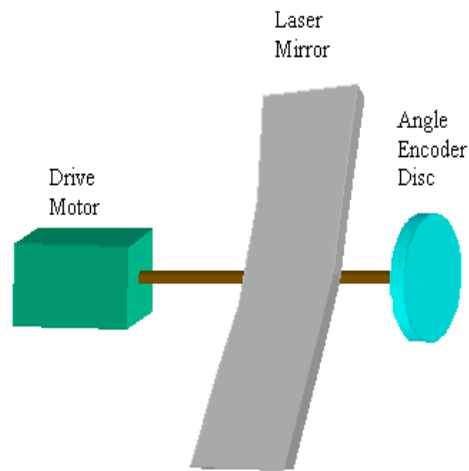


Figure 2-11: Scan Mirror Components

The scan mirror is attached to the drive motor and the encoder disc by a lever (Figure 2-11). The drive motor rotates the lever to the commanded position. During normal operation the scan mirror is in continuous motion. Due to the nature of the oscillating scan pattern however, the mirror is repeatedly accelerated and decelerated in order to reverse its direction. The mirror and the encoder have mass, thus they will have momentum. For the case of the mirror moving counter-clockwise (as viewed in profile Figure 2-12), the values for velocity and acceleration can be described at points A, B and C.

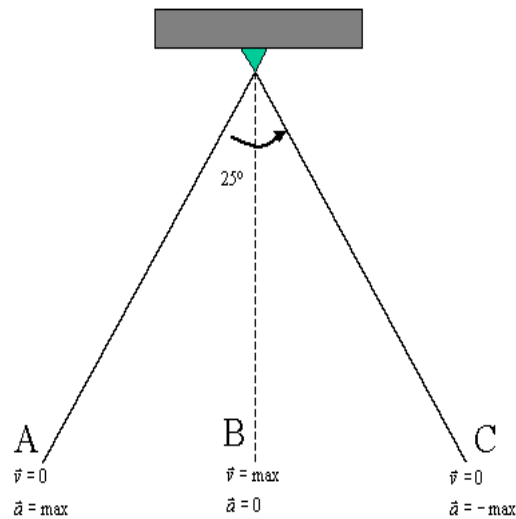


Figure 2-12: Velocity and Acceleration of the Scan Mirror

At point A, velocity would be 0 (the mirror has stopped momentarily as it reverses direction) and the acceleration would be a maximum (maximum force to stop the mirror and reverse its velocity). At point B the mirror is moving counter-clockwise, the velocity would be a maximum, and the acceleration would become 0 (just before reversing acceleration to brake the mirror).

At point B, the mirror and encoder have an angular momentum (Hibbeler 1992),

$$H = I_G \omega \quad (2-12)$$

where,

I_G is the moment of inertia about an axis passing through the combined mass center G

ω is the angular velocity of the mass

The moment of inertia is defined by:

$$I_G = \int_m r^2 dm \quad (2-13)$$

where:

r is the distance from the inertia axis for each mass element dm

The mirror assemble is mounted to the shaft and its mass is unchanging, so the moment of inertia becomes:

$$I_G = \text{constant} = c \quad (2-14)$$

Thus the angular momentum becomes:

$$H = c \cdot \omega \quad (2-15)$$

Immediately after point B, the scanner drive begins to apply a negative acceleration (a torque) to brake the mirror as it approaches point C. If the system were a perfect rigid body, the scanner would continue to follow simple angular motion. However, due to the large acceleration forces needed to move the mirror across the FOV between 15-50 times per second, the lever arm undergoes torsion (Figure 2-13, Foley 2002), i.e.:

$$T = \bar{a} = f(\text{FOV}, \text{ScanRate}) \quad (2-16)$$

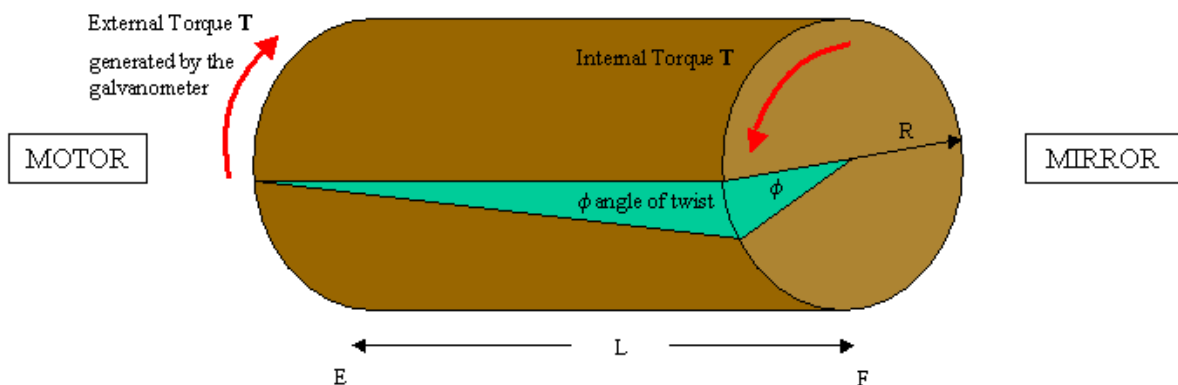


Figure 2-13: Torsion on a Shaft

The drive torque applied at point E, will be reduced by shear within the lever arm, and the mirror at point F will lag behind the direction of E by the angle, ϕ , where:

$$\phi = \frac{TL}{JG} \quad (2-17)$$

where,

- T the torque in the shaft
- L the length of shaft being "twisted"
- J the polar moment of inertia of the shaft = $(\pi/32) d^4$ (for a solid shaft)
- G the Modulus of Rigidity (Shear Modulus) for the material

The overall effect of the torsion, when viewed in profile (Figure 2-14), is that the encoder lags behind the mirror, which itself lags behind the position of the drive motor.

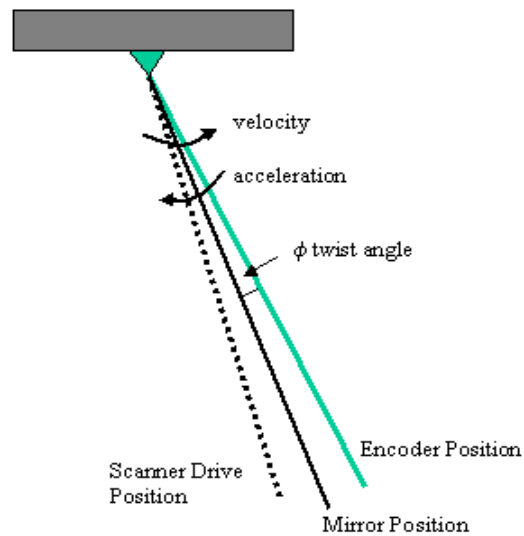


Figure 2-14: Component Lag

The difference in angular position between the scan mirror and the encoder causes a misregistration of the observed distance. As seen in Figure 2-14, the mirror sends the laser pulse in the direction of the solid black line, but the encoder perceives that the pulse came from the direction of the solid green line, which lags behind the black line by ϕ . Over flat terrain the range measurement at the mirror position will be shorter than the range measured at the encoder position, thus an incorrect short range is recorded at the encoder position. The difference between the true distance at the encoder direction and the measured distance from the mirror increases proportionally with the scan angle, the FOV and the scan rate. The observed effect in the data is the strip bowing, which is also commonly referred to as the “sensor smile” (Figure 2-15). The “smile” can be a frown however, depending on the particular design of the scanner. If the encoder is placed before the mirror, then the mirror will lag behind it, and the registered distances will be too long; produces a downward bow or a frown.

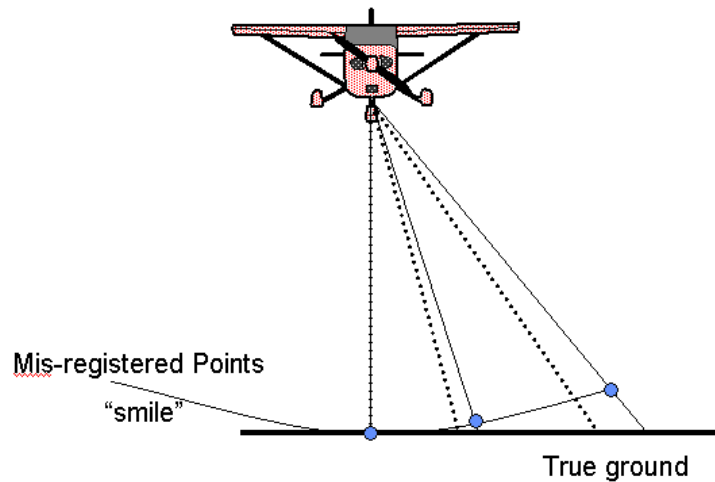


Figure 2-15: Scanner Error

Although the angular errors can be modeled using the Equations (2-12) – (2-17), it can also be noted that the accumulated effect on the ground data is that the strip has taken on a parabolic shape. By modeling the parabola, a simple correction model can be used, i.e.:

$$\beta = \beta_0 + \beta_0 \cdot c \quad (2-18)$$

where:

- β is the corrected scan angle
- β_0 is the encoder angle
- c is an angle correction constant

A positive value for c will cause the encoder to push out, thus increasing the bowing; a negative value will bring in the encoder, aligning the mirror and encoder and flattening out the bowing. Although this simplified equation may appear to only model a linear distortion (rather than the parabola), it must be noted that the corrections occur at the scan head, and are not directly applied on the ground. Thus a linear increase in the scan angle distortion, will

produce a parabolic shape in the points derived on the ground. This is demonstrated in (Figure 2-16).

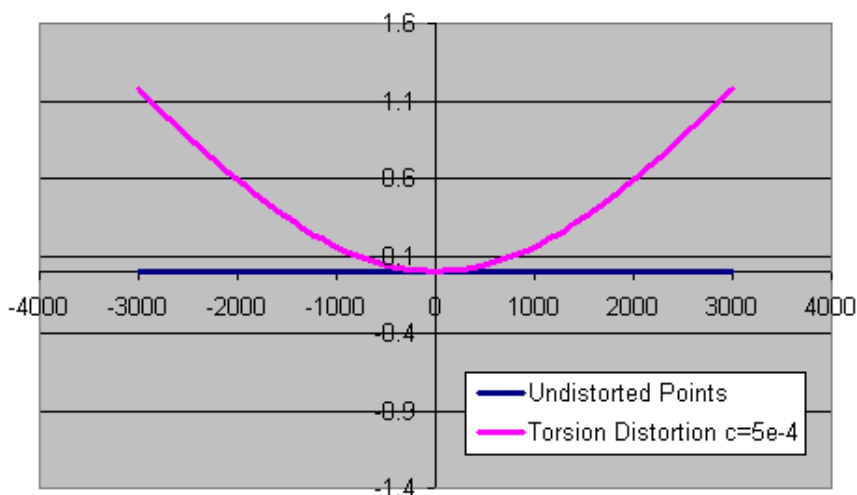


Figure 2-16: Parabolic Effect of a Linear Angle Correction

2.2.5 Encoder Latency

The angular encoder can also be affected by a timing delay in the control unit. Although the delay does not induce a physical change in the encoder, its effects result in a systematic error pattern on the derived ground points. The timing delay is the difference between when the range measurement is recorded, and when the angle is recorded. Because the mirror is moving, the time delay causes the range to be registered to an incorrect angle. When the encoder is stationary, such as at the edge of the FOV, the angle deviation is 0. As the mirror gains velocity while it travels towards nadir, the angular difference grows, up to a maximum at nadir. However, the height discrepancy decreases towards nadir as the slant range shortens to become the nadir range. The pattern, as seen on the ground, looks very much like a bow tie, with two symmetrical loops centered on the scanner's nadir point (Figure 2-17).

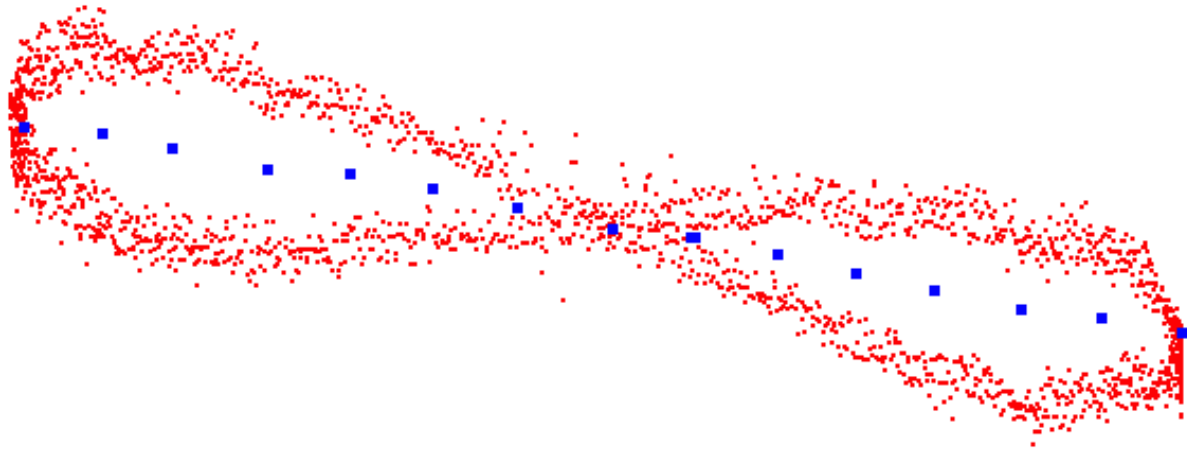


Figure 2-17: 'Bow Tie' Effect from Latency Error
 (red points are mis-registered laser hits, blue points are the true ground)

Typical latency values can range from 0 – 15 microseconds (Leica Geosystems 2002). In a system operating at 45° FOV and 20Hz scan rate, a 15 μ s latency delay would induce an angular difference of:

$$\bar{v} = 0.5 \cdot \frac{45^\circ}{1/80s} = 1800 \text{ deg/s} \quad (2-19)$$

$$\Delta\alpha = \bar{v} \cdot 15\mu s = 0.027 \text{ deg} \quad (2-20)$$

The correct latency value can be found by manually changing the magnitude and plotting the results in a profile. When the bow tie no longer appears in the data, the latency value has been determined. Because the latency is a function of the control unit, it will remain constant for a system and should only need to be determined once.

2.2.6 Navigation System

Errors in the GPS system are dependent on the operating conditions and set-up. These include the reference station baseline, number of satellites in view and whether precautions to avoid loss of lock were taken during flight-time (Cannon 1999). Ambiguity resolution is done before the mission begins, while the platform is on the ground. If loss of lock were to occur during the flight, the result would be catastrophic for the ALS system, and would require a mission delay so that the system could reacquire lock with on-the-fly ambiguity resolution (Mostafa and Hutton 2001). With correct ambiguity resolution, post-processing position accuracy is typically 5-15 cm (Wehr & Lohr 1999). Without it, the navigation solution reverts to a single point-positioning mode (no differential corrections) and the accuracy quickly degrades to several metres, which is unacceptable in ALS systems. GPS is also prone to error through tropospheric and ionospheric effects. Their residual effects contribute an error of up to 5-30cm (Applanix 2002). In ALS systems, these become manifested as offsets between the measurement frame (typically WGS84) and the local level frame. Significant errors also arise through the offsets and misalignments between the GPS antenna, INS and laser systems (see Section 2.2.7 Integration Errors).

The INS system contributes several types of errors in the ALS system. The overall accuracy of the navigation attitude will depend on the quality of the INS - typical values for a commercial system are between 0.005 - 0.01 degrees (absolute accuracy) (Vaughn et al 1996). Commercial systems often employ civilian versions of tactical military sensors such as those from Applanix Corporation (Mostafa and Hutton 2001). Current models from Applanix have accuracies of 0.005 degrees in pitch and roll, and 0.008 degrees in heading. The terrain can affect the accuracy however. Areas with a large amount of geoidal undulation will require additional processing to obtain accurate attitude information (Krabill 2000). This is due to the gravimetric gradients that distort the navigation output. These areas are usually located in mountainous terrain but can include regions elsewhere as well. Errors

in absolute accuracy may not become apparent in the ground data unless it is compared to control surfaces. An absolute error in the navigation solution does not tend to affect the relative accuracy of the points, thus allowing a post-mission adjustment of the data to model the errors.

In addition to the absolute accuracy, INS gyroscopes are subject to sensor drift. For the Applanix sensors, gyro drift rates can vary between 0.1 - 0.75 degrees/hours (Applanix 2002). The gyroscope measurements contain biases, drift error and noise. The navigation processing software will attempt to remove the biases and drifts based on previous calibrations but the noise component remains. It has been observed in ALS data that the remaining noise errors appear to be correlated with time, and their effects become manifested in the ALS data by systematic inconsistencies in laser strips. Over a long measurement time, strips may exhibit an apparent bend or torsion. Due to the systematic nature of this type of error, it can be modelled by a time dependant parameters determined in a post adjustment. The effect of this gyro error is not a stable or deterministic property however. To compensate for this error an adjustment must be made for each strip. This type of adjustment has been subject of research by Crombragh, Brugelmann and de Min (2000), Mass and Vosselman (2000) and Morin and El-Sheimy(2001).

The most critical error in ALS systems is the angular misalignment between the scanner and the INS system (the boresight error). Errors induced by the misalignment are a function of flying height, scan angle and flying direction – and must be addressed before an ALS system can be practically deployed. At a platform height of 700 metres and an off-nadir scanning angle of 15 degrees, a misalignment of 0.1 degrees will result in a height error of 32 cm and a planimetric error of 131 cm (Krabill et al, 2000). These errors are readily apparent in overlapping ALS data. Comparing areas with elevation gradients (buildings, hills etc) will reveal inconsistencies. The components (roll, pitch, heading) of the errors are illustrated in Figure 2-18.

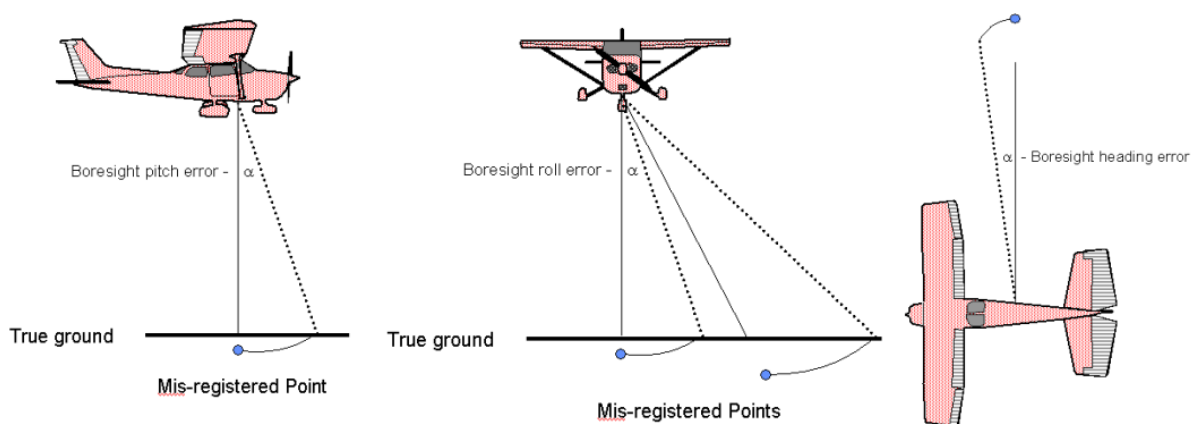


Figure 2-18: Misalignment Errors

The misalignment between the laser and the IMU causes each laser observation to be registered with an incorrect aircraft attitude. The pitch error (Figure 2-18: left) results in a laser slant range to be recorded as nadir. As the slant range is longer, the entire strip tends to be pushed down. A roll error also causes a slant range to be incorrectly registered. The elevation differences tend to increase with a larger scan angle (Figure 2-18: center). The heading error induces a skewing in each scan line (Figure 2-18: right). Unlike a photographic image, a boresight error affects each observation and cannot be removed by applying a simple affine transformation to the entire strip. Instead the differences must be modeled by observing the induced errors in position of control points or common feature points. Given that these errors are correlated with flying direction, they can be decorrelated by observing targets recorded from different directions (Section 3.4). This forms the basis of the self-calibrating model.

2.2.7 Integration Errors

The errors associated with the command and control module relate to system integration. For accurate target determination, all measurements must be referenced to a common time epoch. Each major sub-component has its own timing system, which can be coordinated with GPS time. For accurate integration, clock offsets and drifts must be determined through calibration. Any time delays must be known or they will introduce errors in the integration. Further, the sub-systems take measurements at different rates. The GPS system typically operates at 2 Hz, INS at 200 Hz and the laser measures at 10-50 kHz (Baltavias 1999). Navigation information is interpolated to match the laser measurements. In normal flight conditions the INS data usually smoothes the GPS data to give stable results. In more turbulent conditions, interpolation errors may lead to target determination errors. In such conditions, the user must be prepared to accept a lower accuracy of the ALS system.

2.3 Summary

The summary of the most common types of ALS errors is given in the table below. The type and severity dictate what errors can be, and will typically be addressed in a calibration methodology. The estimated size of the error is the effect on the derived ground point, which will depend on the flying height. For this table, a flying height of 1000m is used.

Table 2-1: Summary of ALS Errors

<i>Type of error</i>	<i>Size of error</i>	<i>Method</i>	<i>Stable</i>
<i>Scanner/INS misalignment</i>	XY: 0.5-5 m Z: 0.2 – 1.5 m	Flight calibration	Minimal change flight-to flight
<i>Gyro drift</i>	0.1-0.75deg/hr XY: 0-10cm Z: 0-10cm	Post-flight adjustment	No
<i>INS alignment</i>	0.008-0.08 deg XY: 0.1-1.4m	Flight calibration	Random but bounded
<i>DGPS</i>	XY: 5-30cm Z: 5-30cm	Post-flight adjustment	Random but usually bounded
<i>GPS – atmosphere</i>	Z: 0-30cm	Post-flight adjustment	Random but usually bounded
<i>Scanning – latency</i>	0-15 μ s XY: 0-0.5m Z: 0-0.5m	Post-flight correction	Stable
<i>Scanning – torsion</i>	XY: 0-15cm Z: 0-45cm	Flight calibration	Parameter dependent
<i>Scanning – encoder</i>	0.02-0.001 deg XY: 2-35cm Z: 2-20cm	Pre-flight	Stable
<i>Range – timing</i>	Z: 0.5-2cm	Pre-flight	Stable
<i>Range – bias</i>	Z: 0-2m	Pre-flight	Stable
<i>Range – reflectivity</i>	Z: 0-20cm	In-flight	Varies on target

Chapter 3

Calibration Methods

The accuracy of final results obtained for an ALS system depends on the entire processing chain and is influenced by the GPS system, the IMU, the scan angle encoders and the range finder. Achieving the highest accuracy requires that every component of an ALS should be calibrated before and after a mission and the data adjusted to control. In practice however, such an undertaking is impractical due to time and expense considerations, and unnecessary due to the relative stability of the calibration parameters and the magnitude of certain error sources. As summarised in Table 2-1, many of the calibration procedures can be categorized into pre-flight methods, post-flight calibration and post-mission adjustment.

3.1 Pre-Flight Calibration

Pre-flight calibration procedures include methods that would in practice be completed only occasionally, and methods that would be performed for each mission. Error sources that are

relatively stable such as range finder biases and some scanner biases are the least frequently applied; whereas navigation equipment initialisation is a standard set-up function of an ALS.

Many of the laser range finder's calibration parameters such as bias and range walk can be determined on the ground. In a procedure described by Vaughn et al. (1996) and similar experiences by Krabill (2000), the ALS platform is kept stationary on the ground while the laser is directed to a fixed target. The distance to the target is measured with a steel tape or an independent Electronic Distance Measurement device (EDM). By varying the power of the emitted laser from the detector threshold to saturation, a function curve or table can be established to model the apparent range based on received power. The corrections can then be applied either in real-time during data collection, or in post-mission during the integration of the navigation data with the range data. To model clock drift parameters, this method could be extended by taking measurements at various distances. Offsets between the different correction curves would be accounted for by clock parameters.

The navigation equipment needs to be initialized for each mission as per the manufacturers' specifications. For DGPS this involves setting up the ALS system near the reference GPS station and determining the integer ambiguities of the carrier phase measurements. Previous tests have used a set-up time of 45 minutes both before and after the flight (Krabill et al 2000), which is rather long for a static initialization, but in practice this set-up time can be less. To ensure continuous and reliable navigation data, pre-mission planning must include an analysis of the GPS constellation during the mission time. A successful mission will have several satellites in view (more than 6) during the entire mission time and their positions will be equally distributed in the sky to ensure an unbiased navigation solution (Canon 1999). Failure to consider the GPS constellation could lead to a poor navigation solution, or a navigation failure due to an insufficient number of satellites. Constellation configuration is deterministic and a number of software packages, including some based on Internet sites, offer a preview of the GPS satellite positions.

In flight considerations must be taken into account for DGPS as well. To avoid the loss of integer ambiguity, efforts must be taken to avoid large flight dynamics. This includes reducing platform rolls to less than 10 degrees and post-poning flights in turbulent air. In practice it is common to fly an entire test run without losing ambiguity resolution (Vaughn et al 1996). If loss of lock does occur during the mission however, data collection must be halted until the navigation is able to reacquire a solution using on-the-fly ambiguity resolution (Canon 1999).

The INS system also needs to be initialized so that it can detect and establish the local level frame. This is usually performed by keeping the ALS platform stable and allowing the INS gyros to detect the local level frame (Shwartz and Wei 2000). In areas of significant geoidal undulation, the INS initialisation can be affected by a large deflection of the vertical. This deflection will then bias the rest of the navigation solution. To compensate, the corrections can be entered during the integration of the navigation data with the range data, or adjusted in a post-mission strip adjustment.

The lever arm offsets between the systems can be measured with a steel tape or through total station survey. They should be measured to within 1-3 cm to minimise their impact on the solution. Any error in the offsets will be propagated as a bias onto the target coordinates. The misalignment angles between the system components remains the biggest challenge of the calibration. The angular differences between the laser and INS are solved in a post-flight adjustment

3.2 Post-Flight Processing

There are several calibration parameters that cannot be measured directly. These include the largest source of error, the misalignment angles between the INS body frame, defined by its three accelerometers, and the scanner frame, defined as a point and a set of axes on the

scanner mirror; as well as many of the scanner errors. Due to the large, but relatively stable nature of these errors, they would be determined in the field on an occasional basis. Despite the need of every ALS system to determine these calibration parameters, there is currently no standard method of undertaking the task. Techniques vary from manual adjustments, using surface constraints and forming least-squares adjustments.

Currently the most common method of calibrating an ALS system is by a manual adjustment. This method involves flying the ALS sensor over a series of control points or a known surface. Profiles are compared of the ALS data strip and the known surface. The effects of the misalignment are readily visible by an offset between the two profiles (Figure 1-3). A user then manually applies corrections and reprocesses the data. Comparing the new profiles demonstrates the effects of the corrections. Usually roll and pitch are determined by comparing profiles over flat areas. The parameters are changed until the overlap areas coincide. Heading can be determined by examining areas with large elevation gradients such as buildings. Two flight lines are flown over a building area; one flight line captures the building on the far right of the FOV; the other flight line captures on the far left. The errors in the heading induce a distortion in building location. By changing the heading parameter, the distortions will change. The heading is altered until the building sides coincide.

Once the misalignment angles are approximated, the scanner errors can be estimated. Their effects will be seen by a systematic distortion of the data profile along the control surface. Often a bowing will appear in the profile; where the edges will rise above the known surface. Again the user applies corrections depending on the error model used in the sensor; and continues to reprocess the data until the edges flatten out. The manual calibration procedure can take several iterations (10-50) and require considerable amount of time (1-2 days). The end results are usually only judged 'by eye' as the method does not produce any direct statistical information about the solution. Further, because the calibration was undertaken looking at small sections of the data, the solution may be biased by any local errors or

variations in the observed surface. Thus the calibration may not be the best solution for the entire dataset.

A boresight misalignment calibration method proposed by Vaughn et al. (1996) and Krabill et al (2000) involves flying the platform over a level surface (body of water) or a well-known surface. By varying the platform's roll and pitch between -10 and 10 degrees while taking range measurements of the surface below, the estimates for the roll and pitch misalignment can then be derived. The calibration parameters are determined by plotting the angle (roll or pitch) versus the measurement range (Figure 3-1). Fitting the data with a least-squares solution to a 2nd degree polynomial should result in a curve with 1 minima.

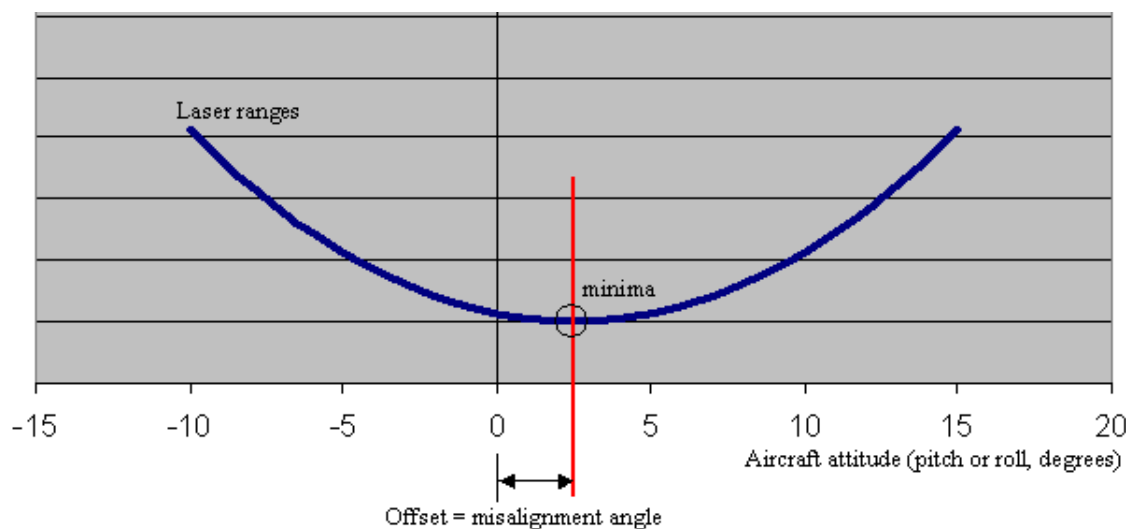


Figure 3-1: Roll and Pitch Misalignment Plot over a Flat Surface

The horizontal offset between the minima of the curve and the zero axes is the misalignment angle of the sensor. The calibration can be done quite easily on an arbitrary body of water (with the proper selection of laser wavelength (Wolf & Lehr 1999)) without the need for ground control. The lack of ground control makes this approach very appealing. A disadvantage of this method however, is that heading errors cannot be easily recovered. Attempts have been made to extend this technique (Hofton et al 2000) by solving for all three

parameters simultaneously. The complexity of the solution proved a difficult change and only approximate values for misalignments were recovered. The lack of gradients over the smooth surface also make it difficult to decorrelate the heading errors with other error sources.

The most analytical method of recovering the calibration parameters is to attempt to model the effects within an observation equation, and perform a least-squares adjustment. This method is a typical photogrammetric approach to the sensor calibration problem. Unlike photogrammetry however, several issues prohibit a simple solution. In classical frame photogrammetry, images are taken of areas with known points. By observing the known points in the images and modeling the relationship between the image coordinate and the ground coordinate through the central perspective, the position and orientation of the camera can be determined. For this same design, models for additional errors such as lens distortion or misalignment can also be determined.

ALS data also has a central projection (via the laser head), but unlike photogrammetry, control points are difficult to measure. Contrary to frame imagery where the entire frame is taken at one epoch, each point from an ALS occurs at a different epoch. This makes a position and orientation solution derived from observations impossible. Instead, points from different epochs must be combined to recover the systematic effects of the calibration errors.

Further, in frame imagery it is possible to measure control points because of the higher resolution of the image, and the continuous nature of imagery; i.e. each pixel or colour element is connected to another. In ALS data, there is no connectivity of points; points are distributed in psuedo-random pattern on the ground. The scanner can not be directed to aim at a control point, so small and precise points which would aid in calibration, are very likely to be missed during flight time. The point resolution of ALS data is also very poor. This is caused by the divergence of the laser beam as it hits the ground. From a flying height of 500 metres, a laser beam is usually 30 cm in diameter as it strikes the ground. The footprint

makes edge detection very poor; thus even if control points could be hit by the laser, their edges are often not clear and thus the measurement would not be precise.

Despite the problematic nature of measuring features on the ground, this kind of approach is still promising for several reasons. The unknown parameters can be modeled explicitly and stochastically thus permitting direct and statistical analysis of their effects. Also, because the modelling process is similar to traditional frame photogrammetry, many existing tools and techniques such as soft-copy image processing aids can be used. And from work in autocorrelation and automatic point generation, there is the prospect of automating the calibration process for ALS data as well. With this justification, several additional calibration methods have been proposed.

A simple method in use by the Dutch Survey Department (Crombaghs, Brugelmann, de Min, 2000) implicitly solves for the roll and pitch misalignment. In this method the differences between overlapping strips is modeled by a three-parameter surface, i.e.

$$\Delta H(U, V) = a + bU + cV \quad (3-1)$$

where,

- U, V are point coordinates in a local strip frame
- a is a vertical offset of the strip (GPS error)
- b, c are roll and pitch parameters

The observations for this equation are made up from ‘patches’ in the ALS data. Rather than using single points, the patches are composed of many points in a flat area. The resulting elevation is an average that will have a higher accuracy than a single point. This helps to reduce the random noise of the individual points. The ‘tie’ points are entered into a least-squares equation and 3 parameters are solved for each strip. Control points, if available and observable, are also added as observations. When not using control, the ALS data strips should be laid out and flown in a way to maximize differences between them. An intuitive

procedure would be to fly strips in opposing directions such as in photogrammetry. One set of parameters can be solved for the entire data, but better results were found by assigning 3 parameters to each strip. Thus although results using this method demonstrated a reduction in overlapping errors, further analysis showed evidence of additional systematic error. The most obvious was the need to model the heading boresight error.

A calibration method described by Burman (2000-2), adds the heading misalignment and also includes the GPS atmospheric errors (datum shift). Rather than solve for linear parameters, this method describes the boresight angles as a rotation matrix, i.e.

$$\begin{pmatrix} X \\ Y \\ Z \end{pmatrix}_l = \begin{pmatrix} X_0 \\ Y_0 \\ Z_0 \end{pmatrix} + \begin{pmatrix} X_d \\ Y_d \\ Z_d \end{pmatrix} + (R_{INS} \cdot R_{INS}^{LRF}) \begin{pmatrix} l_x \\ l_y \\ l_z \end{pmatrix}_{LRF} \quad (3-2)$$

where:

- $(X, Y, Z)_l^T$ is the ground coordinate
- $(X_0, Y_0, Z_0)^T$ is the GPS coordinate of the laser scanner
- $(X_d, Y_d, Z_d)^T$ is the datum shift
- R_{INS} is the rotation matrix with attitude information from the INS
- R_{INS}^{LRF} is the misalignment between the INS and the laser head
- $(l_x, l_y, l_z)^T$ is the laser components

This method can be implemented with or without ground control. Without ground control the datum error cannot be determined - it is therefore assumed to be zero. Unlike the previous method, which relied on a level surface, this method exploits sloped surfaces to determine misalignment. With sloped surfaces, larger differences can be seen in overlapping strips. Points of interest for tie points were found by passing a Sobel edge detector over the rasterized height image. It was found however, that vegetation and irregular structures on the surface interfered with automated point extraction. Manual intervention was required to obtain suitable observation points. The corresponding points were then found in the other

strips and the observations are added to a least-squares equation. One set of misalignment angles are then solved for the entire data set. Analysis of the results still indicated further sources of error however.

The final method described here increases the parameterization to include INS drift rates. This method presented by Behan, Maas and Vosselman (2000), like the Crombaghs method, also solves for parameters on a strip-by-strip basis. Unlike that method however, the model is based on the general ALS target Equation (2-7). This method employs tie points from the strips in a local strip coordinate frame (Figure 3-2).

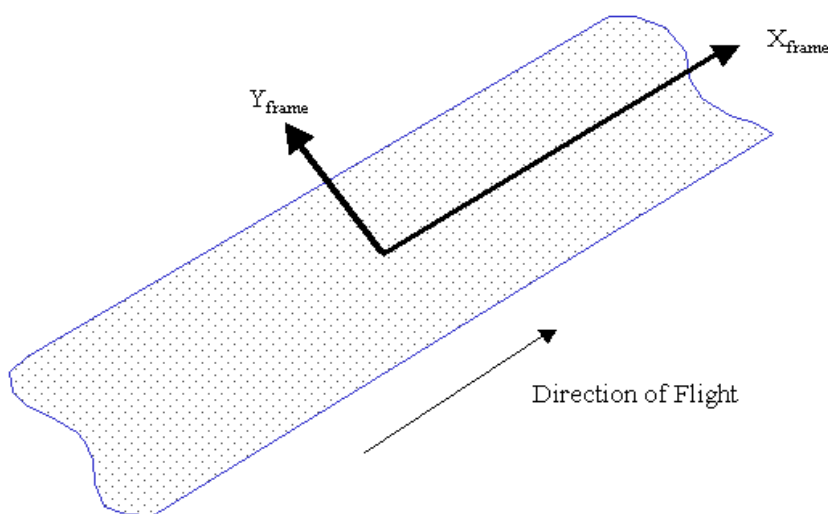


Figure 3-2: Strip Coordinate Frame

In the strip frame, the positive X axis corresponds to the line of flight of the platform. In this way the time dependent parameters of INS drift can be replaced by U, the x coordinate of a point in the strip frame, which is proportional to time. This method requires ground control points within the mission area to solve for all 9 parameters per strip. The authors attempted to implement an automated tie point extraction algorithm by searching for gradients in the elevation data. Due to problems associated with occlusion and resolution however, they resorted to manual observations. Their results showed the greatest reduction in residual

error. However, because they solved for parameters on a strip basis, this method is not truly a calibration of systematic errors, but rather a post-mission polynomial adjustment.

3.3 Proposed Method and Data Requirements

The goal of the proposed calibration method in this research is to allow the determination of the boresight misalignment angles on a global basis rather than a strip-wise basis. The new calibration model begins with the simple observation equation (as shown in Equation 2-7 and repeated here for convenience):

$$r_i^m = r_{nav}^m(t) + R_b^m(t) \left[R_S^b \cdot r_i^S + a^b \right] \quad (3-3)$$

where:

r_i^m	coordinate of laser target (i) in the mapping frame (m-frame)
$r_{nav}^m(t)$	coordinate of the combined navigation sensors (GPS/INS) in the mapping frame
$R_b^m(t)$	the interpolated rotation matrix from the navigation body frame (b-frame) to the mapping frame
R_S^b	rotation from body frame to the scanner frame (s-frame) to the body frame
r_i^S	laser vector from scanner in s-frame
a^b	coordinate offset between the b-frame and the s-frame

This equation contains the boresight misalignment angles (R_S^b). The laser components are expanded to allow include the scanner angle:

$$r^S = R_L^S(t) \cdot r^L = R_L^S(t) \cdot \begin{pmatrix} 0 \\ 0 \\ d \end{pmatrix}^L \quad (3-4)$$

where:

- $R_L^S(t)$ is the rotation from the laser frame to the scanner frame using the scanner mirror angle β
- r^L is the laser range vector in the laser mirror frame (L-frame)
- d is the corrected range measurement from the laser

Combined, the sensor equation becomes:

$$r_i^m = r_{nav}^m(t) + R_b^m(t) [R_S^b \cdot R_L^S(t) \cdot r^L + a^b] \quad (3-5)$$

where:

- $R_b^m(t)$ is a full rotation matrix with roll, pitch and heading taken from the navigation sensor (Ω, Φ, K)
- R_S^b is a full rotation matrix of the misalignment parameters (ω, ϕ, κ)
- $R_L^S(t)$ is a rotation matrix about the secondary axis with the scanner angle (β)

The equation is the base model from which additional parameters can be added. To add a parameter for the scanner error due to torsion, the scanner angle must be expanded:

$$\beta = \beta_0 + \delta + \varphi \quad (3-6)$$

where:

- β is the corrected scan angle used in the scanner rotation matrix $R_L^S(t)$
- β_0 is the raw scanner angle from the scan angle encoder
- δ is the sum of the scanner corrections (Section 2.2.4)
- φ is the atmospheric correction (Section 2.2.1)

The scanner corrections for torsion can be modeled as a function of the raw scanner angle (Section 2.2.4), i.e.:

$$\delta_{torsion} = c \cdot \beta_0 \quad (3-7)$$

where:

c is a constant correction value for torsion

The combined equation for each epoch is then:

$$r^m = r_{nav}^m + R_b^m \{ \Omega, \Phi, \mathbf{K} \} \left[R_s^b \{ \omega, \phi, \kappa \} \cdot R_L^s \{ \beta, c \} \cdot r_i^L + a^b \right] \quad (3-8)$$

The unknown calibration parameters for this equation are:

$$\bar{x} = [\omega, \phi, \kappa, c] \quad (3-9)$$

As described in the previous section, the unknown parameters can be solved by observing control points in the ALS data. The use of control points allows for a parametric least-squares model to be formed, and a unique solution to the calibration parameters found. It is highly desirable however to implement a calibration method that does not rely on known ground control points.

One way to solve the observation equation is to observe distinct, but uncontrolled features in the overlapping area. These features could be similar to those used in conventional photogrammetry such as road markings; but should avoid non-continuous features such as building edges due to the increased possibility of mis-measurement. The calibration errors result in coordinate discrepancies between the common features. A calibration solution can therefore be found by minimizing these discrepancies, i.e. for a feature observed in 4 overlapping strips:

The user observes the feature in each strip, $(X, Y, Z)_{target}^i$

If the effects of the calibration errors are uncorrelated in the feature observations, then the average of the feature coordinates should be approximately the value of the true position,

$$\begin{pmatrix} \bar{X} \\ \bar{Y} \\ \bar{Z} \end{pmatrix}_{average} = \frac{1}{n} \sum_{i=1}^n \begin{pmatrix} X \\ Y \\ Z \end{pmatrix}_{target}^i \cong \begin{pmatrix} X \\ Y \\ Z \end{pmatrix}_{True} \quad (3-10)$$

The discrepancy between the average position and observed position of the point becomes the misclosure information needed to solve the unknown parameters by least-squares minimization, using the parametric form (Krakiwsky and Abousalem 1995, Kuang 1996):

$$\hat{l} = f(\hat{x}) \quad (3-11)$$

$$\hat{r} = A\hat{\delta} + w \quad (3-12)$$

$$w = f(x^0) - l \quad (3-13)$$

$$\hat{\delta} = (A^T C_l^{-1} A)^{-1} \cdot A^T C_l^{-1} w \quad , \hat{x} = x^0 + \hat{\delta} \quad (3-14)$$

where:

- \hat{l} is the vector of adjusted observations
- \hat{x} is the vector of unknowns (Eqn 3-9)
- $f(\hat{x})$ is the observation equations (Eqn 3-8)
- \hat{r} is the vector of observation residuals to be minimized
- A is the matrix of partial derivatives with respect to x
- $\hat{\delta}$ is the vector of corrections to the unknowns
- w is the vector of misclosure
- x^0 is the vector of initial approximations
- l is the vector of average tie point values (Eqn 3-10)
- C_l^{-1} is the a priori weight matrix (Section 4.4)

As a non-linear model, this procedure must be iterated until a solution has converged, i.e.:

$$w^{n+1} = f(x^n + \hat{\delta}^n) - l, \text{ until } \hat{\delta}^{n+1} = 0. \quad (3-15)$$

If the IMU sensor is approximately oriented to the laser frame, then the boresight angles should be very small. An initial approximate of 0 for the boresight angles should be sufficient to begin the iteration process. The quality of the results depends on a sufficient amount of decorrelation of the calibration errors in the observed feature positions. In turn, this depends on the characteristics of the data determined by the flight planning.

3.4 Observations and Flight Planning

In order to solve the calibration parameters with the greatest accuracy and stability, the discrepancies between the overlapping strips should be a maximum. To achieve this, flight planning needs to be carried out while considering the calibration effects on the resulting data.

Previous work (Burman 2000, Mass 2000) has suggested that overlapping calibration flights should be undertaken over terrain with substantial sloped relief. The sloped areas provide differences in the tie points that help determine the solution. For this project, and in general commercial ALS operation, calibration flights are usually flown over airports and runways, which by their nature tend to be flat. Thus flight planning needs to take the flatness of the terrain into account when modeling the misalignment error effects.

Roll misalignment was described in Section 2.2.6. The misalignment causes the measured distance to be registered in the incorrect position. The effect on the registered over flat terrain is that it appears lower and pushed out from the center of the strip. Intuitively, the largest difference in overlapping strips would be created by a strip flown in the opposite direction. This is demonstrated in Figure 3-3.

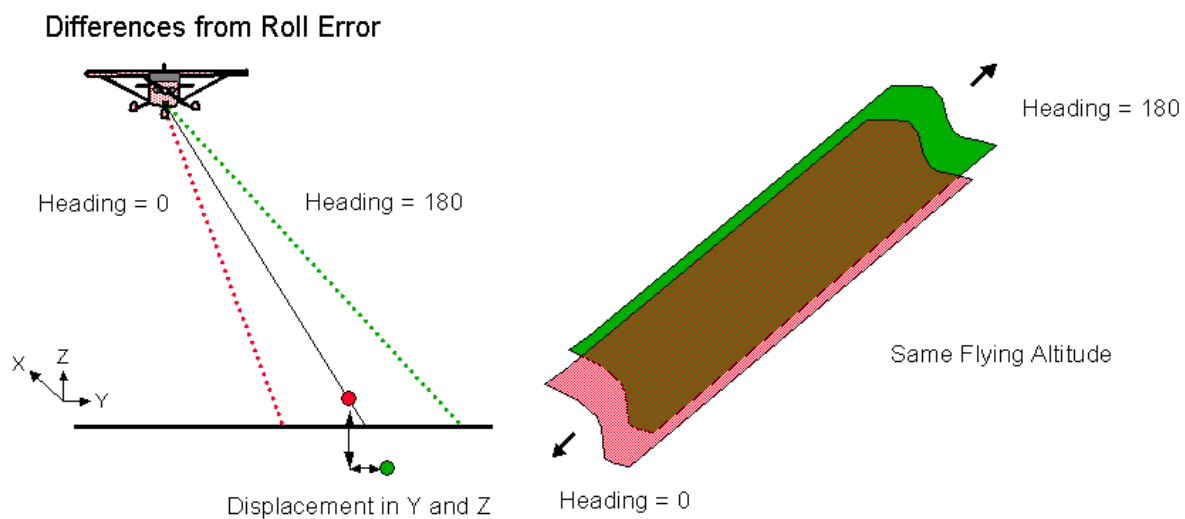


Figure 3-3: Effects of Roll Error on Overlapping Data

Over sloped terrain, the same argument for the pitch misalignment error can be made. Over flat terrain however, a point would be misregistered in the same way from two strips flown in opposite directions (Figure 3-4). Instead, an elevation difference can be generated by flying strips at different altitudes. This will generate a vertical discrepancy (Figure 3-4). The difference will be proportional to the flying height:

$$\Delta h = (H_1 - H_2) \left(\frac{1}{\cos \theta} - 1 \right) \quad (3-16)$$

where:

- Δh is the difference in elevation discrepancies
- H are the flying altitudes
- θ is the pitch error

Differences from Pitch Error

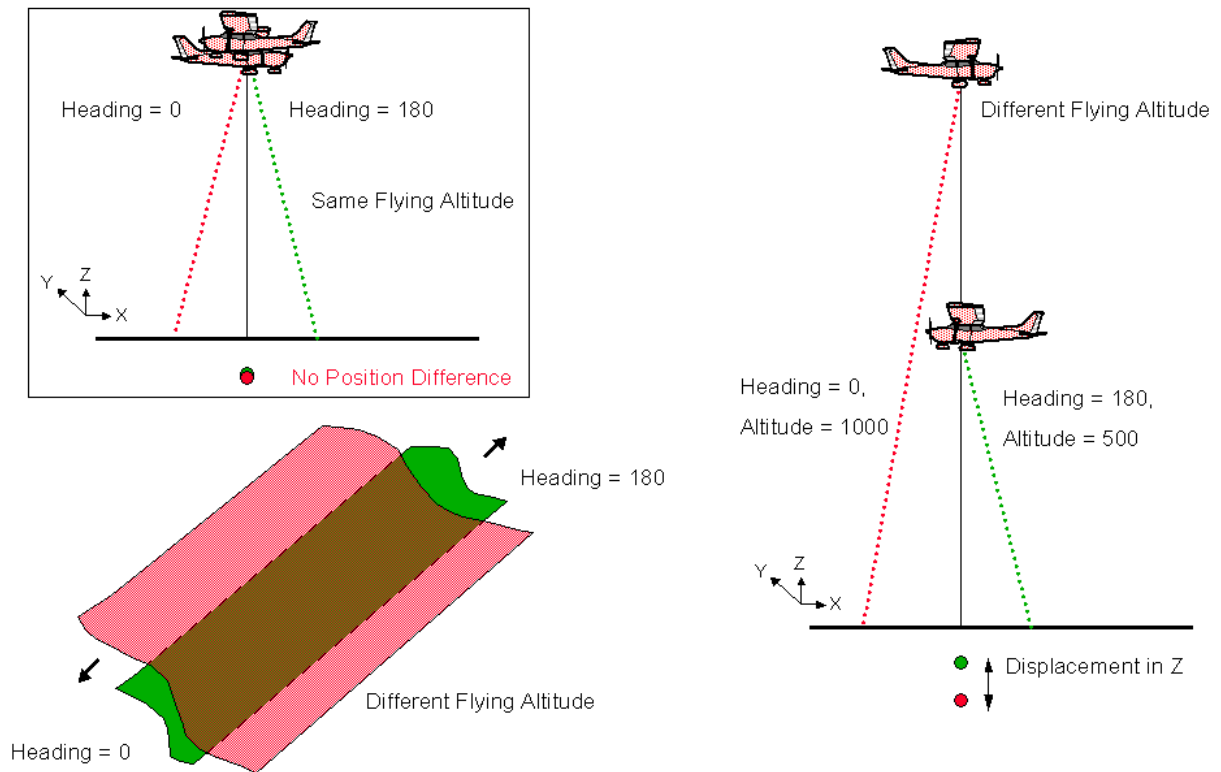


Figure 3-4: Effects of Pitch Error on Overlapping Data

The heading misalignment error is the most problematic to model from tie points. If flight strips are flown in opposite directions, the forward and reverse misalignment effect will create the same displacement on the registered point (Figure 3-5). Instead, flight lines should be flown at 90° from each other in order to maximize the differences. Planimetric features are more difficult to measure accurately however, due to the lower horizontal accuracy of ALS data. This can be observed in the variances of the heading solution.

Differences from Heading Error

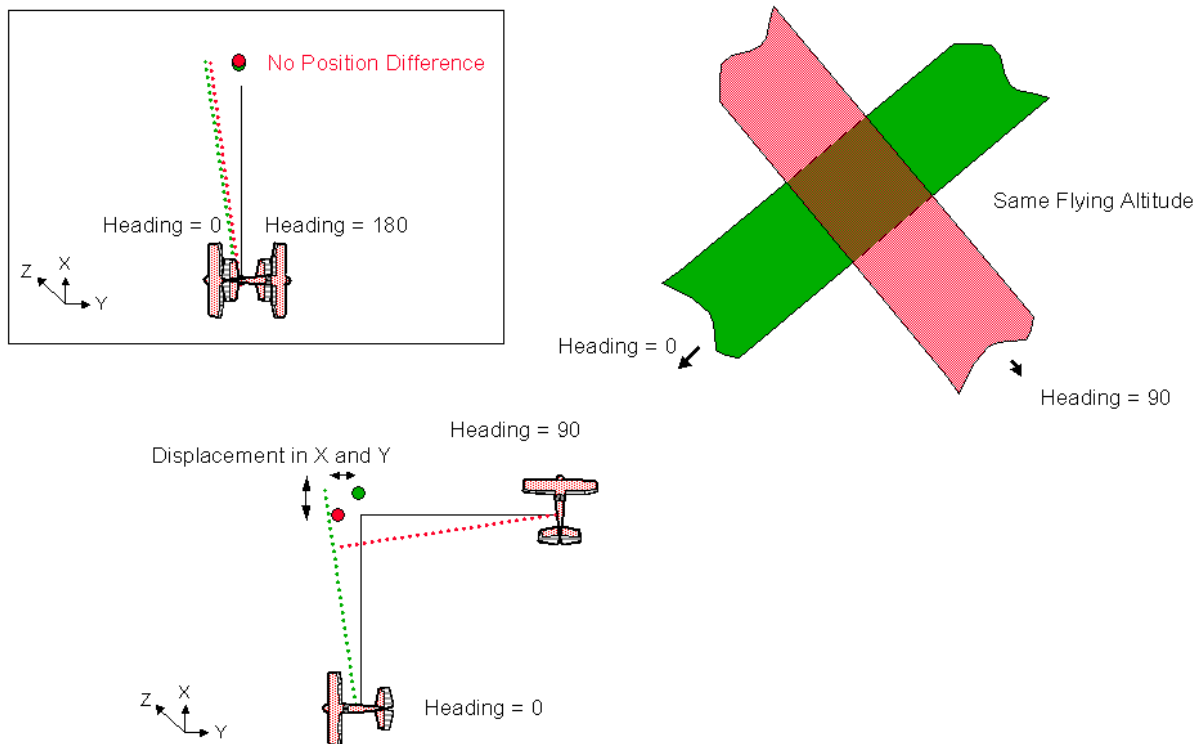


Figure 3-5: Effects of Heading Error on Overlapping Differences

The torsion error causing the bowing of the data strip is also symmetric and not modeled by a simple flight line in an opposite direction. The elevation differences from torsion errors will increase with altitude and higher scan rates. To observe the differences, flight lines should be arranged so that the edges of the strips with the move torsion error will overlap the center of the strips with minimal torsion error. Similar to the heading error, the differences are maximized by flying at 90°. The torsion error will create elevation differences however, which permit that parameter to be determined more accurately. Combining the different requirements for each parameter results in a calibration flight pattern shown in Figure 3-6.

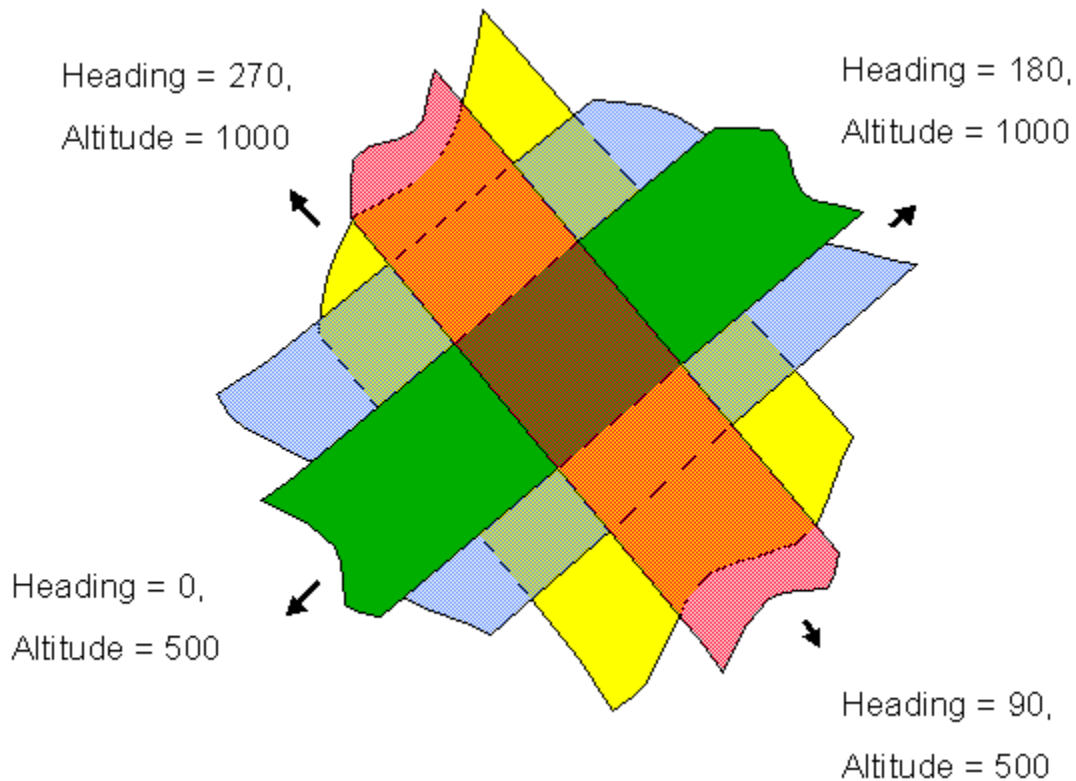


Figure 3-6: Optimal Flight Pattern for Calibration

3.5 Psuedo-Observations

Once a suitable dataset has been obtained, tie points can be observed in the overlapping areas within the strips. The non-continuous nature of the ALS data presents another challenge however. It is very improbable that laser pulses from different strips will strike a feature in the same way. In order to identify the position of a common feature from the laser data, points must be interpolated. Thus the tie points used in the adjustment are actually ‘pseudo-observations’ based on interpolated real data.

In many photogrammetric projects involving digital terrain models, the ideal representation of the surface is obtained by using an Triangulated Irregular Network (TIN). The TIN representation allows for a fast linear interpolation of any point in the surface, using the 3

nearest observed values. Due to the very large size of ALS data however (often >10 million points per strip), the triangulation and storage of the network in a computer is a very costly operation (for computers of 2002). For example, a 3-dimensional point can be represented in computer memory using 12 bytes of memory (each coordinate component being stored as word). For a dataset of 10 million the required memory is 114.0 MB ($10M \cdot 12 / 1024^2$). A TIN representation however, often uses 62 bytes or more for each point (the point, its triangle, its neighbors etc). The memory required for this representation is 591MB. Further, because a TIN is by nature triangulated, a Delaney triangulation of the data is applied upon initialization. Such a procedure requires repetitive access and searching of the raw data set. Search times grow with the size of the data; thus datasets approaching ALS sizes can take large amounts of time to set up.

To avoid the memory and time penalties associated with TINs, this research implemented a spatial indexing algorithm. Without any indexing, each interpolation on the data would require a search through the entire dataset. Instead, the data is split into 2 intersecting hash tables. The regions (or buckets) created by the hash tables 'fill up' with real data. To search for the data, a hash function quickly determines a table look-up value that reduces the search space to the size of the bucket. The memory cost of this feature is an additional 4 bytes (a pointer) for each point; thus raising the data requirement size to 16 bytes (plus some overhead for the hash table).

Interpolation of the tie points is still carried out using linear-interpolation. An algorithm was implemented that determines the nearest 3 points which form a triangle enclosing the desired interpolated point. A pseudo-observation tie point needs an interpolated elevation and needs to know what the navigation state would have been at its interpolated time. In this project, the GPS time of observation was added to each observed point. The time was then interpolated for the tie point. The interpolated time created a reference back to the navigation data which itself was time tagged. A further interpolation allows for the determination of the aircraft position and orientation at a time the tie point would have been observed.

The frequency of the navigation data is usually set by the navigation post-process; but often results in positions and orientations every 0.005 seconds (200Hz). In fairly calm weather, the aircraft will move smoothly from 1 epoch to the next; thus interpolation of the navigation data is very accurate. The greatest source of error for the psuedo-observation is from the elevation on the ground. If the points are spaced too far apart, the linear-interpolation will be a poor approximation of the true earth. If the void in one strip is covered by a real point in another strip, the inconsistencies will bias the calibration solution. Thus for calibration purposes, data of the highest density achievable from the sensor should be used. This will reduce incorrect observations in the data.

3.6 Filtering the Data

Above ground objects are problematic for tie point observations. Due to the angle of incidence, foliage and multiple echoes, vegetation is rarely observed in the same way from two different strips. To avoid poor tie points around vegetation or man made objects, the data should be filtered to extract the ground.

Although it is usually quite simple for a human operator to identify what is ground, it is not practical to manually edit large amounts of ALS data. There are several methods of automated filtering to choose from including morphological, slope based filters and least-square estimators. The results of these systems vary by terrain types (urban, steppe, mountainous) and the density of the ALS data. The systems can be compared by effectiveness of building/vegetation removal, speed of algorithm and smoothness of the derived surface.

3.6.1 Morphological Filters

Morphological filters work by splitting a terrain into small areas and trying to identify local ground points. Intermap Technologies (Intermap 2002) employs a morphological filter in its TerrainFit software and Optech Inc. (Optech 2002) appears to do the same in its ALTM REALM Lidar processing software. Although the two methods appear to be implemented differently, the results are similar.

Typically these filters ask the user to specify an area window size and a threshold value (Kilian et al. 1996). Within the window, the lowest point is taken as the ‘seed’ ground point (it is assumed to be on the ground). Points that are within the threshold of this value are then classified as ground as well. The Intermap TerrainFit method is slightly different in that rather than specifying a preset window size, the terrain is progressively ‘minified’ or averaged to a lower resolution. The lower resolution is based on the minimum values of the higher resolution. This creates a terrain pyramid. Once the top of the pyramid is reached, the algorithm reverses, and progressively adds points from the higher resolutions that fall with the user-specified height threshold (Wang 2001).

These filters can experience problems with some features such as large buildings or thick forest canopy. In such cases, a window size that is too small could be looking solely at building points thus classifying them as ground. The window can be made larger, but then the filter can potential chop off hills that have a significant slope. Kilian (1996) suggested using a series of windows to progressively filter and smooth the terrain. The effectiveness of these filters will depend on the terrain type and the parameters of the filter. Although fast and simple to implement, the results will likely require some manual filtering to remove off-ground points.

3.6.2 Slope Based Filters

A slope based filter attempts to identify ground points by comparing individual points to their neighbors. This is the filter type used in Terrasolid's TerraScan (Axelsson 2000).

Vosselman and Maas (2000), Vosselman (2000) have proposed an alternative implementation as well.

The TerraScan (Axelsson) method of slope filter works by slowly adding points to a derived surface that have a slope less than a user specified value. The algorithm starts by removing outlier points that appear below the average surface. Typically these single points can be identified by a large height difference to their immediate neighbors. Once the outliers are removed, a coarse TIN is formed based on the low points in the ALS data. From the coarse model, the algorithm iteratively adds more points based on whether the new points are within the accepted slope value. The process continues until all points are classified.

The Vosselman (2000) method tests each point against its neighbours. The height difference between points is evaluated by a stochastic function that also takes into account the distance between the points (slope). The function determines whether the point should be classified as ground. Although a purely synthetic function can be used, the method has been designed so that a training set can be used to establish a ground classifying function that is appropriate for each terrain. This creates an easily adaptable filter. A potential problem however, is that the method suffers from the inability to properly classify large buildings. Maas (2001) addressed this problem by amending the algorithm to keep track of suspected buildings. In that case, a large building will have their edges eroded but their middles will remain. The pattern of (misclassified) high ground surrounded by building, surrounded by ground, allows for the identification and elimination of the remaining building parts.

Slope based filtering is a more robust form of filtering compared to morphological filters. The parameters (maximum slopes) are less susceptible to error from local terrain changes.

These methods tend to take an iterative approach. This can require a greater amount of time to classify a dataset then a morphological filter. The derived surface also tends to be rough and contours derived from it are not smooth. Further surface smoothing is required for use in contour mapping.

3.6.3 Least Squares Estimators

The least-squares estimator filtering technique attempts to form a surface model based on a weighted least squares model. This method is used by in the SCOP software package provided by INPHO GmbH (INPHO 2002) developed by Kraus and Pfeifer (1998). Similar methods have been proposed by Lohmann et al (2000) and Schickler and Thorpe (2001).

This technique begins with an arbitrary surface model (a GRID or a TIN) with user specified spacing. In the algorithm a linear predictor relates the points to each other. Some of the methods vary by placing further constraints on the linear predictor (curvature constraints etc). A residual for each ALS observation point is then computed to the arbitrary surface. The size of the residual determines a parameter weight for each observation. Typically a point below the arbitrary surface is assigned 1, points well above are assigned 0 with different weights in between. The ALS points, along with their weights are then used to compute a new arbitrary surface. The process is iterated until all points are classified as ground or other.

This method appears to be very good at eliminating large buildings and forest canopies. The least-squares optimization tends to smooth the surface that can result in a good contouring product. A significant problem however, is the computational burden. Each grid point is an unknown in the least-squares equation. The least-squares solution can be found using a Choleski decomposition, but the number of operations is still on the order of N^2 for each iteration. Kraus and Pfeifer addressed this problem by splitting the surfaces into patches limited to 200 points each – but for a large project this could result in a large number of

patches. Despite some of these concerns however, Schickler and Thorpe state that a large-scale model can be solved in 10 minutes – although they do not indicate their data size or grid sampling.

3.6.4 Filtering Consideration for Tie Point Selection

For calibration purposes, a psuedo tie point should try to minimize errors from interpolation. Thus original observations should not be modified. This criterion eliminates least-squares methods of filtering due to their smoothing properties. The tie point also needs to ensure that it is on the ground and has a high likelihood of being observed in the same location from different strips. Hence accuracy of the ground model is important. In this respect, slope based filtering has an advantage over morphological filters.

To improve the accuracy of most filters, including slope based filtering, ALS data is usually passed through a series of initial filters to remove gross errors from the scanner. This is critical for ensuring the accuracy of tie points. These filters typically analyze individual points and compare them to their immediate neighbors. As seen in Figure 3-7 the target point (red) is compared to its neighbours (green) up to a certain radius (for this example, 5 metres). If the difference in elevation is large, such as being lower than 0.5 metres, then the individual point is removed. Although simple, this method is very effective at removing errors.

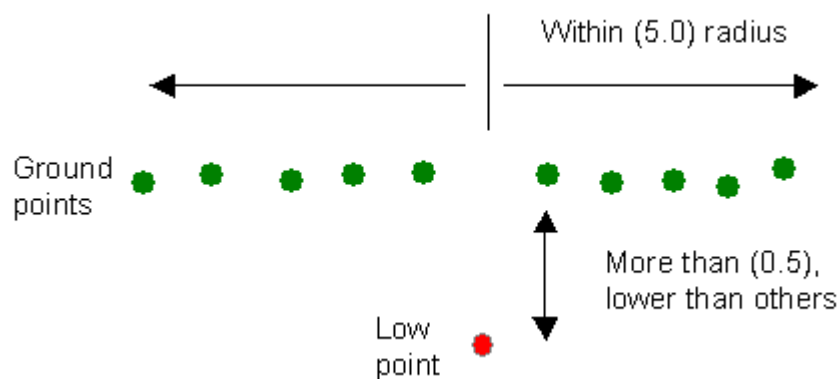


Figure 3-7: Filtering Outlier Points

3.7 Summary

Existing post mission adjustment methods vary considerably. The most common and least desirable involves the manual adjustment of calibration parameters. This method produces one set of calibration parameters, but at a high cost in time and associated uncertainties. Methods using tie points are faster and more rigorous, but many current methods produce parameters that are strip dependant, require ground control, or demonstrate the presence of additional error. The desired approach should be fast, give a global solution, work without control and model most errors.

The systematic errors of boresight misalignment and scanner torsion error can be expressed in a parametric form. To solve for the unknown values, standard least-squares techniques can be employed to determine the parameters in a redundant system. The solution can be found using ground control points, but a preferred solution involves a method based on observed differences between overlapping strips. To maximize differences and increase reliability however, overlapping strip data must be collected in a clover-leaf pattern. Pseudo tie points can then be collected by interpolating elevation and time information around features in the data. Points are then referenced back the navigation data in order to obtain all of the information needed in the parametric equation. To ensure that tie points are

interpolated to the same place in different strips, it is important to remove non-ground points from the data. This multi-step approach ultimately allows the user to observe feature points in different strips, and resolve calibration parameters.

Chapter 4

Methodology

In order to evaluate the calibration method proposed in this thesis, a review of the test data and specific implementation issues is required. Four evaluation cases are described and the criteria used to test the results of the calibrations are listed.

4.1 Test Data

Data for this thesis was collected at the Sitterdorf airstrip, outside of the City of St. Gallen in eastern Switzerland (Figure 4-1). The airstrip consists of a single runway, an adjoining taxiway and a small apron area with aircraft hangers. This airstrip is regularly used by teams at Leica Geosystems to stage tests of airborne sensors. The runway has been manually surveyed in the past using static GPS. One Hundred and ninety seven points were collected at regular intervals along the paved areas. Any markings that might have been used to locate the measured points on the runway are not visible from the ALS data (intensity images) and for the purposes of this thesis, are considered to be unsignalised.

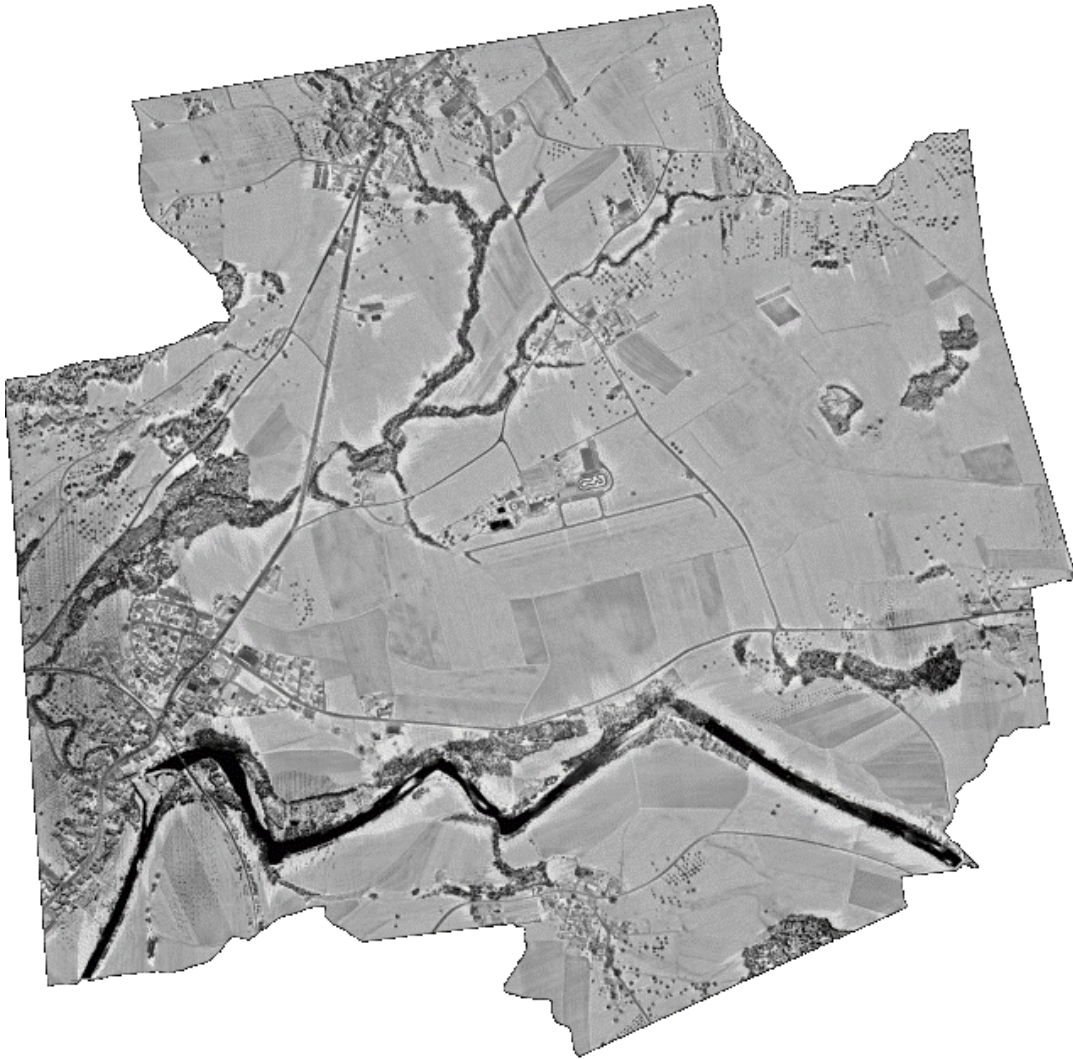


Figure 4-1: Intensity Image of Sitterdorf Airstrip and Surrounding Test Area

The airport area is situated in a rural valley setting. Most of the area surrounding the airstrip is farmland, with a small village on the western side of the test data and a rural road network throughout the test area. A small river runs along the southern side of the area, which flows against an escarpment, and a creek along the northern side of the area which flows through a local drainage depression. The slope in the central area is lightly graded, with slope gradients varying from 0 to 20%. The area surrounding the riparian features is moderately to heavily sloped, with gradients from 30-50%. The slopes in the test area can be more readily identified in the colour shaded relief map (Figure 4-2). The escarpment stands out as the

green band on the bottom of the image. The elevation of the area gradually increased from West to East.

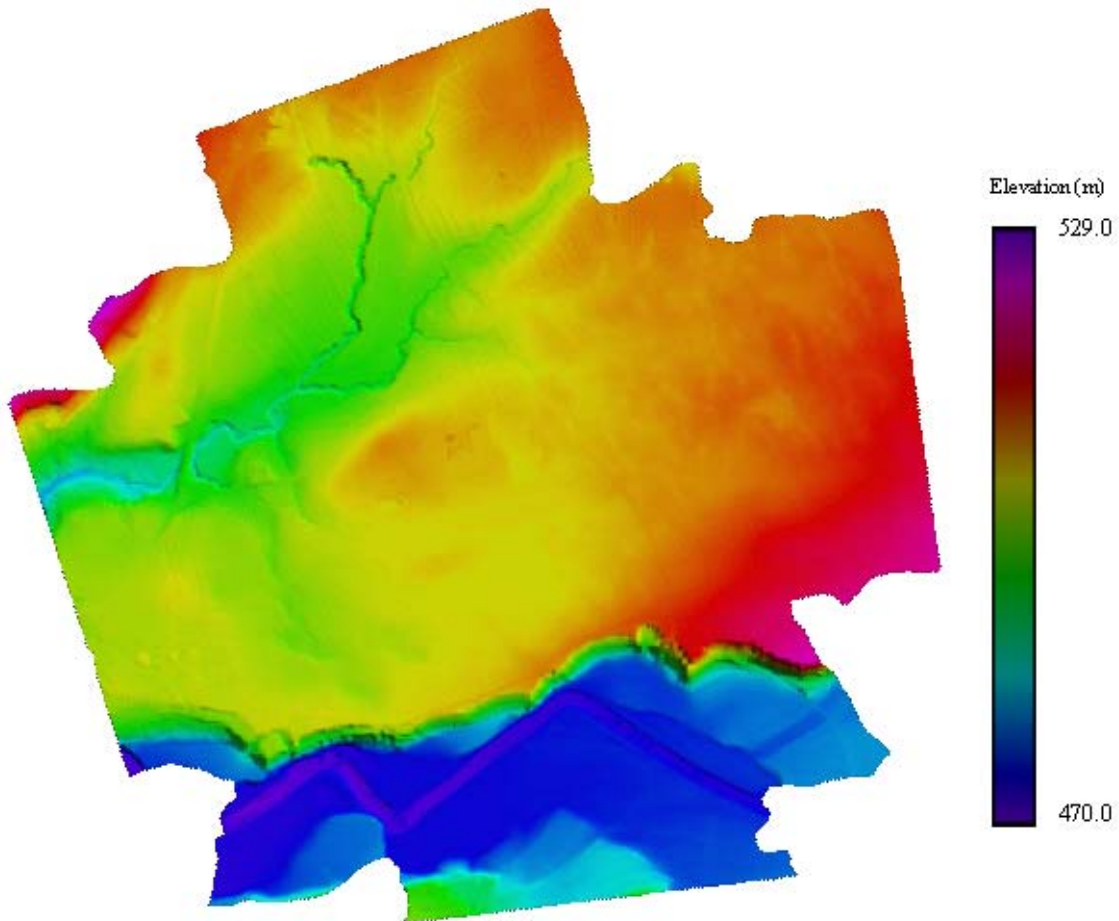


Figure 4-2: Colour Shaded Relief of the Test Area

The data was collected in the clover-leaf manner described in Section 3.4, with strip directions altering on each pass and at 2 different altitudes (Figure 4-3). The scanner used was the Leica Geosystems ALS40 (formerly known as the Azimuth AeroScan scanner). The ALS40 is a sinusoidal scanner with a field of view of up to 75 degrees and a maximum operational altitude of 6000 metres. Due to a possibility of eye injury to personnel looking up from the ground during flight, the energy output of the laser in the scanner is governed by

a set of filters based on its flying altitude. In this test, data was collected at 900 and 1500 metres. The same filter was applied at both these elevations. Any effects of the filter were not modeled in this thesis. Data was collected with a pulse rate of 38kHz and a scan rate of 19.5Hz. This resulted in 7.7 million points being recorded in the overlap calibration area.

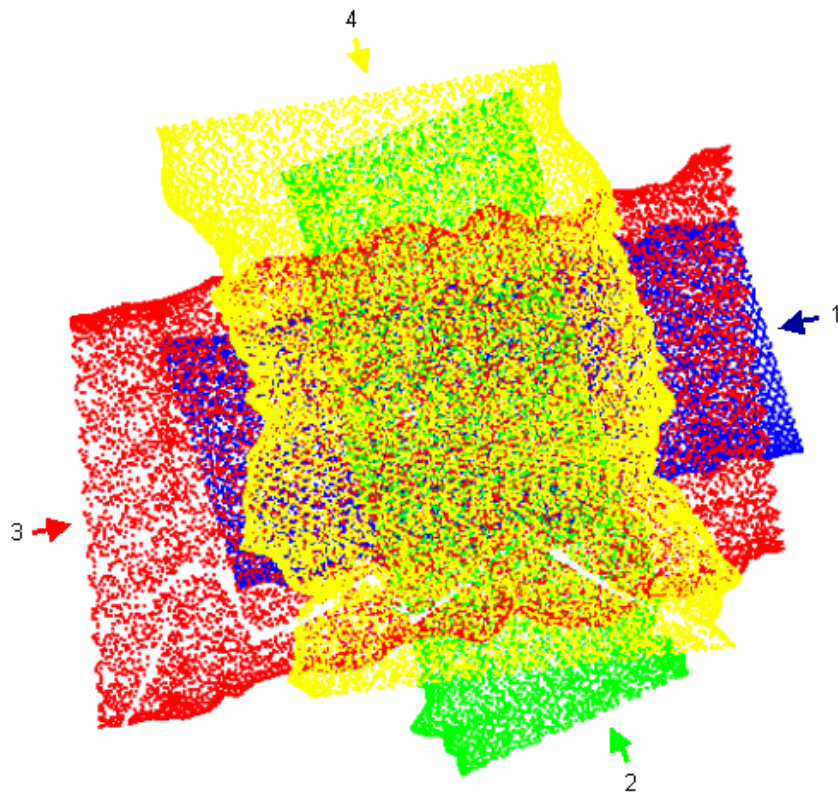


Figure 4-3: Flight Line Layout

The navigation data for the ALS40 is provided by an Applanix POS 510. This unit combines a Novotel GPS receiver with an AIMU (Applanix 2002). The navigation solution for the ALS40 uses differential GPS data collected from a base station. For this test, the base station was located next to the Sitterdorf runway that coincides with the center of the calibration area. The differential data was processed using Applanix's POS/PAC navigation software, which combines the GPS and IMU data to produce an optimal navigation solution. The lever arm between the GPS antenna and the IMU was measured approximately with a tape and a

plumb line, and was entered as a parameter to the POS/POC processing software. The offset between the IMU and the scanner frame was not measured directly. The X and Y components were assumed to be zero; the Z component was treated as a constant elevation bias of the system. Its value was determined as part of the total elevation bias in post mission processing, but was not considered in the calibration. During the collection time, the GPS constellation was well distributed in the sky with a PDOP of 2.12 (IntegriNautics 2002). There were also no known geoidal anomalies in the area that might cause problems with the IMU data.

The laser and scanner information is combined with the navigation data using Leica Geosystems' ALS40 Post Processor. The software produces files containing the X, Y, Z and intensity values of each observed point. Among various file formats, the program also outputs a file containing interpolated navigation data for each observed point. This file was used in the calibration implementation.

4.2 Pseudo Observation Collection

The point file was then loaded into Terrasolid's TerraScan (Terrasolid 2002) software package running in conjunction with Bentley MicroStation (Bentley 2002). TerraScan provides three dimensional visualization as well as filtering algorithms that can be applied to the ALS data. Each strip was processed separately in TerraScan. The gross errors in the ALS data were removed and the ground identified using TerraScan's slope-based filtering (Section 3.6.2). The ground filtering allows a comparison of the entire overlapping surface area without having to consider the effects of vegetation on the tie point observations. Of the 7.7 million points observed in the overlap area, 5 million were identified as lying directly on the ground. The remaining points are in trees, buildings, or were low-level vegetation.

With the ground points identified, the next step was to generate images from which tie points could be observed. Although images based solely on the elevation data can be created, a

much more effective image can be generated by using the intensity information in the ALS40's data. To that end, the intensity values of the randomly distributed ground points were interpolated to regular grid spacing – for this test, to 1-metre intervals. Due to the nature of the points however, the images produced are in fact ortho-rectified view of the surface (i.e. there is a direct mathematical connection between an image coordinate and the ground points). This relationship can be described in a simple affine transformation from the image coordinate system (x,y) , to the 2D mapping system. The property was exploited in the creation of software for this thesis. The interactive software, named Attune, manages the ALS intensity images and their affine relationships with the mapping frame. This permitted the next step of tie point observations.

In order to model the differences between the strips, common features must be identified. Attune was developed with an interactive point measurement tool that allows the user to mark common features in ALS data (Figure 4-4). The points were recorded in the image frame (in pixels), and later converted back to the mapping frame using the affine relationship established by the ortho-image.

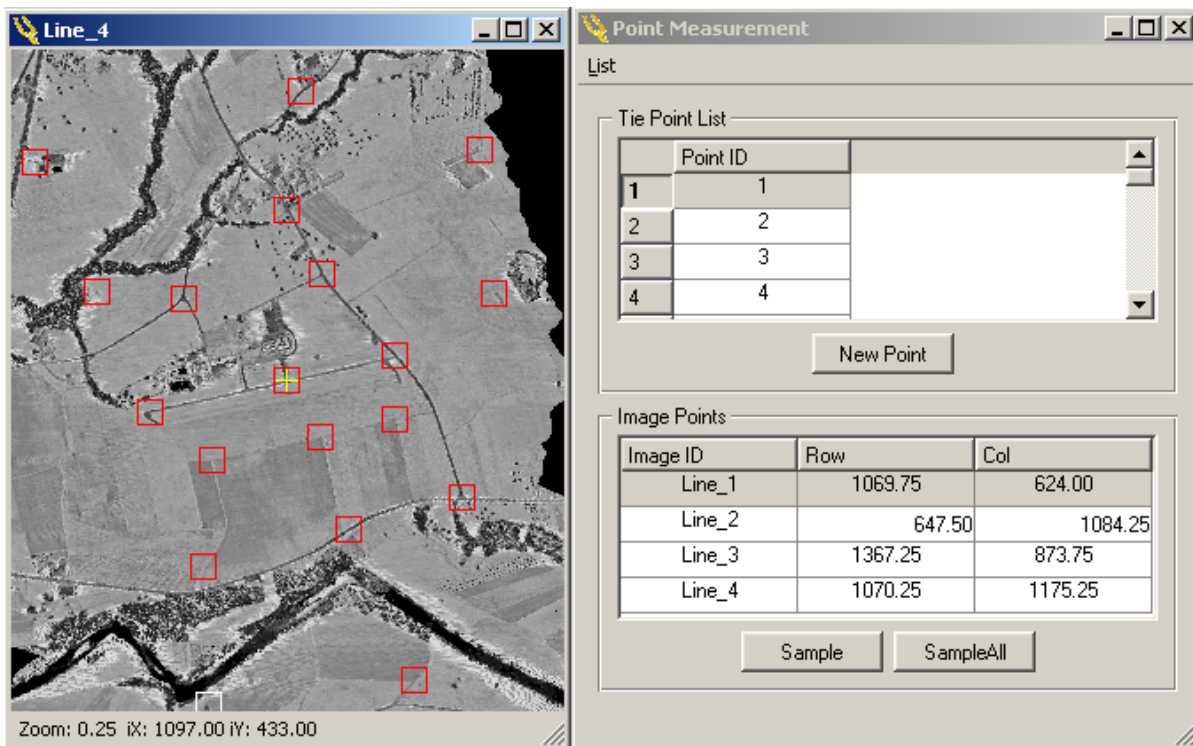


Figure 4-4: Attune Tie Point Selection

Due to the similarity to existing soft-copy photogrammetry workflows, commercial photogrammetry software, in this case Leica Geosystems SOCET SET was also used for testing the ALS boresighting. Tie points from the intensity images were identified using the Interactive Point Measurement (IPM) tool in SOCET SET. Although this tool contains a large number of features geared towards automated photogrammetry, for this test it was used to simply allow manually picking of common points visible in the intensity images. One of the IPM features is the ability to automatically collect tie points in overlapping images using auto-correlation techniques. This tool was tried, but the results were very poor. It was concluded that the low resolution, coupled by the varying response of the intensity information based on angle of incidence did not permit autocorrelation techniques to work as well as they might in a standard photogrammetry problem. However, this remains an area of research for future study.

The chosen tie points will almost certainly never coincide with a true ALS observation; thus further interpolation is needed. In order to reduce the effects of multiple interpolations however, the 2D tie points are reference back to the filtered ground points. The ground point files are loaded into a hash-table surface representation that allows for efficient searching (Section 3.5). The nearest 3 points that define a triangle in which the tie point is contained were chosen to interpolate elevation and time – using linear interpolation. Using the interpolated time, the orientation of the aircraft was determined at the “pseudo-observation” time. The psuedo-range was then computed by inversing the solution from the ground point to the aircraft position – and the scanner angle determined similarly. The ALS post processing software also corrected for the scanner error. To determine this error in the adjustment effectively, those corrections were recomputed and subtracted from the pseudo-observation values, in order that the completely ‘uncalibrated’ observation values would be used in the adjustment.

4.3 Coordinate Systems

Several coordinate systems were used in the intermediate steps of the ALS data and tie point observations. The GPS position is implicitly calculated in an Earth Centred Earth Fixed (ECEF) Cartesian system (WGS84), but the processing software only provides geographic ellipsoidal coordinates or mapping coordinates (Snyder 1987). The INS reports angles in a Local-Level reference system, which can be connected with the geographic coordinates. In order to edit the ground point data and form images however, a mapping system was needed. For this test UTM (zone 32) was chosen because of its wide usage and low distortion characteristics. Images referenced to UTM coordinates were generated through the affine transformations. The tie points from the images were then captured in the UTM projection. For precise calculations in the adjustment however, UTM was not optimal. Although the projection tries to minimize angular and scale distortions, systematic errors such as scale and angular distortions still remain; thus UTM introduces errors in position and orientation. The magnitude of the coordinate values also posed a numerical problem for a computer – large

numbers begin to lose precision with only 8 bytes to store them. The solution was to convert the tie point values into a local rectangular reference system (LSR) by transforming the ECEF coordinate system to the centroid of the data. The system preserved the scale and angles of the observations, and removed the common magnitude of the observation points. From here the adjustment could proceed.

An additional advantage of the LSR system is that it aligned the Z-axis of the reference system with the plumb line of the local level frame (assuming no deflections of the vertical). This meant that the z-component of the tie points had a real-world representation of moving up and down on the ground. Although mapping projection systems share this feature, global ECEF systems do not. This allowed an asymmetrical weighting of the observed values in the a-priori variance matrix in the least-square adjustment. The precision of the laser ranger yields a more precise estimate of the elevation component of the ground control point than the planimetric component. Thus the adjustment was weighted to reflect this fact, as will be discussed in the next section.

4.4 Observation Weighting

In the adjustment procedure, observation weights are supplied with the raw data along with estimates to the boresight angles and scanner parameters. Tie point weights were taken to be $\frac{1}{2}$ the size of the pixel resolution for the intensity images. For this data, a value of 0.5m was used for planimetric points. Elevation weighting was estimated to be 0.1m, based on the noise level of the laser, and terrain effects from the horizontal uncertainties.

The adjustment proceeded by averaging the tie point values for each observed feature, and then calculating the misclosure between the average and the observed value. After each correction, the average value of the tie points was recalculated and the misclosure formed again. In addition to this iterative procedure, the adjustment itself was non-linear due to the rotation matrix in which the boresight angles were contained. A small-angle approximation

of this rotation matrix was attempted, but the approximation contained too much error, thus the full rotation matrix was used instead. The solution typically converged within 20 iterations after which the results could be analyzed. Although 20 iterations is relatively large compared to aero-triangulation computations, the high number can be explained by the nature of the updated control points from each iteration. As an iteration completes, the control points are recomputed, causing the solution to essential ‘start over’ rather than ‘refining’ the solution in a typical adjustment.

Tie point observation outliers were identified by large residuals. The Attune software allowed quick identification and removal of bad points (Figure 4-5). The solution was repeated until no outlying points remained. For this test however, only one tie point observation was rejected.

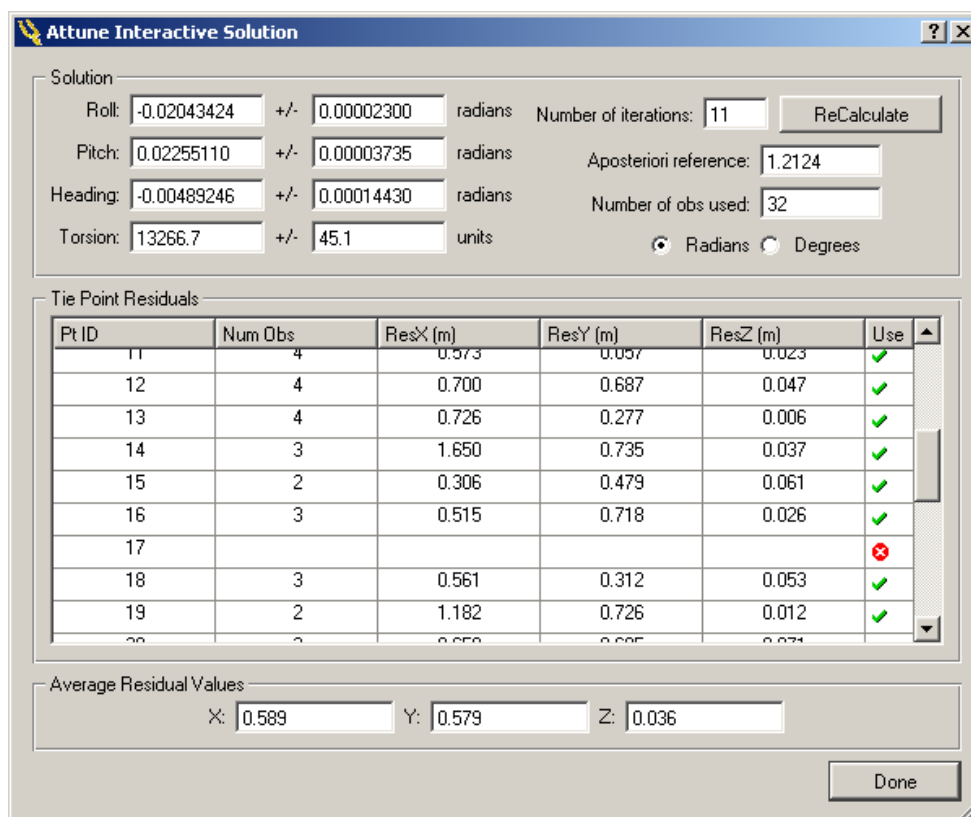


Figure 4-5: Attune Interactive Results

4.5 Solution Evaluation and Testing

To help judge the quality of the calibration method and the effectiveness of adding an additional torsion parameter, the sensor calibration was undertaken by solving for boresight angles only, boresight fixed with torsion modeled, and boresight with torsion correction solved simultaneously. The effects on the quality of the solution are judged in the following ways:

- **Residuals of the tie points**

The goal of the adjustment is to minimize the differences between the tie points. Due to observation errors and/or incorrect parameterization, a perfect minimization is not possible. Residual values remain after the adjustment, which can be used a direct measure of the quality of the minimization. The residuals can be decreased by simply adding more parameters; but care must be taken in that case. Any new parameters must describe a physical phenomenon and must not be correlated with existing parameters. Excess parameters will cause the solution to be unstable and result in overly large solution variances.

- **Control point analysis**

Once the strips have been realigned according to the updated boresight values, the elevation of the strips can be compared to known control points. If errors are being successfully removed, then the distribution of the differences should tend towards 0. In practice however, the differences are likely to center around a non-zero value; this value then being an elevation bias in the ALS system. Ideally the distribution of the elevation differences should show a Gaussian shape. This would suggest that the cause of the differences was random observation error. Deviation from normal conversely suggests that additional systematic error is present in the solution. The

goodness-of-fit of the differences to a normal distribution is undertaken using a standard chi-squared test based on histogram analysis. Detailed histogram results are listed in Appendix A.

- **Elevation differences between strips**

The elimination of elevation differences between strips is the ultimate goal of this project – achieved through a high quality calibration. For testing purposes however, there are two types of elevation differences that can be considered (Figure 4-6). If processing were to proceed such that an average surface was generated from overlapping data, then the distance to the average could be measured as an indication of the quality of the average surface. For calibration purposes however, the value of interest is the total elevation difference between surfaces.



Figure 4-6: Surface Differences

In the case of multiple overlapping areas, there are $(N-1)!$ elevation differences, where N is the number of overlapping surfaces. For this test, which has 4 directly overlapping strips, 6 elevation differences were computed at regular 5m intervals throughout the overlap area. Presented in a histogram the distribution should ideally appear Gaussian, which would indicate that elevation differences were caused by random errors only. A test for the goodness-of-fit was undertaken for each solution using the chi-squared method (detailed listed in Appendix A). The standard deviation of this distribution is the best indicator of the overall quality of the LIDAR ground points. It is used to compare the quality of the solutions.

- **Plotted profiles**

Although this analysis will not directly yield a statistical measure, plotting profiles of ALS data quickly show the effects of systematic error between strips. Effects such as torsion are easily identified by a characteristic shape in the profile (for torsion, a bowing of the strip).

- **Elevation difference plots**

Each elevation difference between strips is calculated at a regular interval, thus the difference has a planimetric location. In plotting the differences by their location, the spatial distribution of the errors is readily seen, along with patterns caused by systematic errors.

Most of these evaluation methods involve analyzing the elevation component of the solution only. The investigation of planimetric error is a more complicated issue due to the non-continuous nature of ALS data. These types of errors are not investigated in this thesis, although their effect is considered during analysis. Further work in planimetric error of ALS systems can be found in Lee and Schenk 2001, Casella and Spalla 2000, Maas 2002 and Behan 2000.

Chapter 5

Results

Before beginning the calibration, the data has been analyzed to establish some initial conditions. The pre-analysis was hindered however, because the large differences between the strips render simple comparison methods unreliable. The most relevant analysis measures are the initial tie point differences and the plotted graphic profiles. The control point differences and regular point elevation differences are affected by the large planimetric shifts between the uncalibrated strips – thus a grid point in one strip will generally not correspond to the same point in the second strip.

For this test a total of 32 points were chosen as tie points. The criteria used for the selection was based on contrasting features that were clearly identifiable to the human user such as road markings. The distribution of tie points was evenly spaced (roughly) throughout each strip. More points were collected along the edges of each strip to better model scanner errors. The tie points distribution is shown in Figure 5-1 and the initial tie point differences are given in Table 5-1.

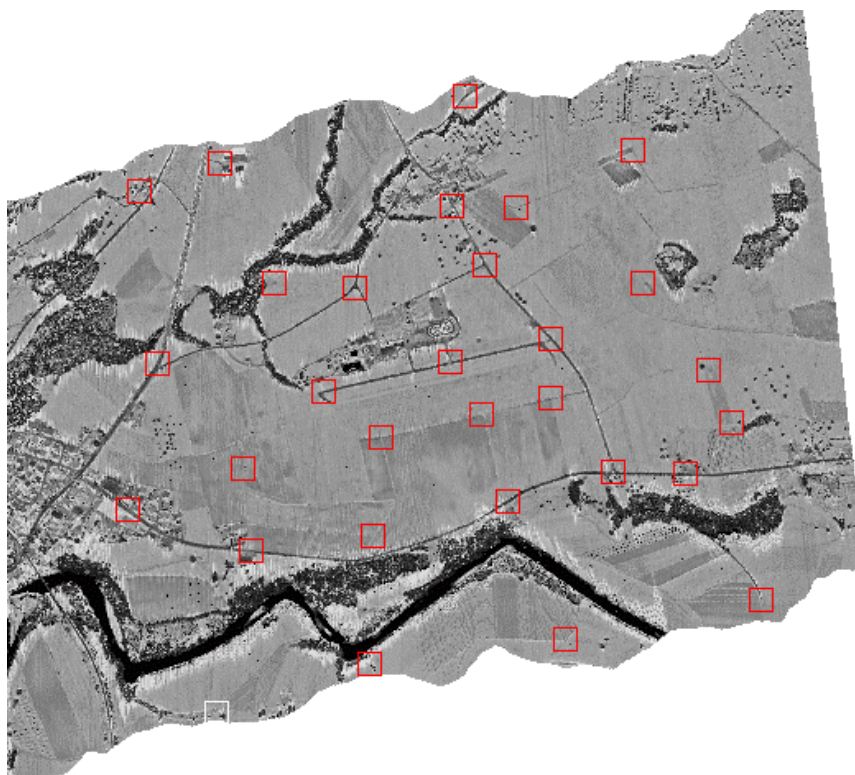


Figure 5-1: Tie Point Distribution

Table 5-1: Initial Tie Point Differences

	<i>X(m)</i>	<i>Y(m)</i>	<i>Z(m)</i>
<i>Average</i>	26.987	24.012	6.440
<i>Std Dev</i>	3.971	7.183	3.006
<i>Minimum</i>	17.250	3.500	0.306
<i>Maximum</i>	37.125	32.750	13.821
<i>Median</i>	26.569	26.322	6.446

Although less useful as noted above, the control point elevation differences distribution is shown in Figure 5-2. This shows large differences with an overall large standard deviation. By visual inspection it is plain that the distribution does not follow a Gaussian trend (red

line). The wide base reflects the presences of large elevation errors. A good solution to the calibration problem will cause the distribution to narrow significantly and begin to resemble a normal probability density function.

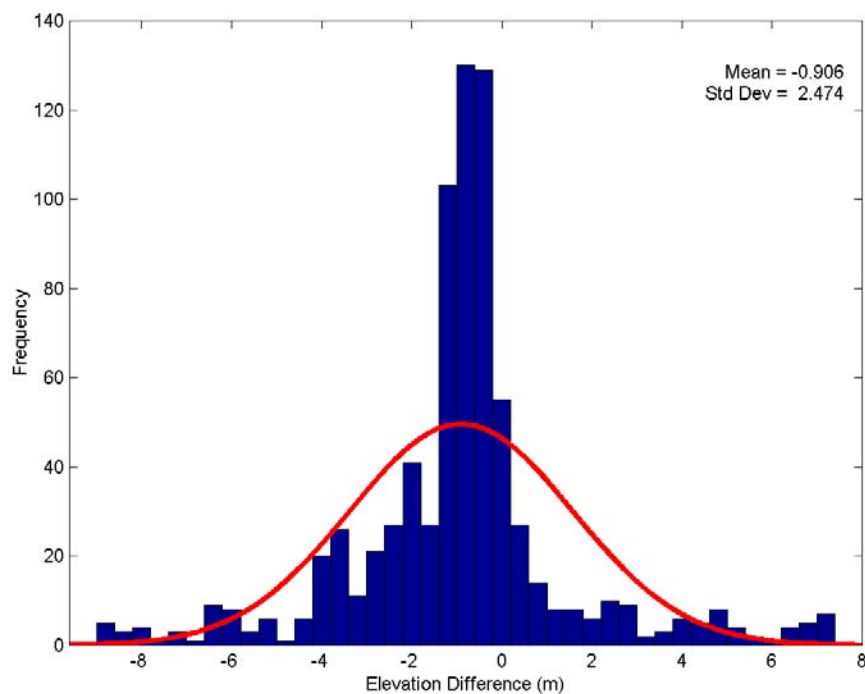


Figure 5-2: Initial Control Point Difference Distribution

The most telling indication of calibration errors can be seen in the graphical profile plot. Differences are plainly visible by plotting along structures such as buildings with peaked roofs (Figure 5-3). The plot shows a clear angular difference between the two strips, an elevation difference and a planimetric shift. What is not plain to see however, is that the strips are not simply shifted from each other, but are distorted in all 3 dimensions. Evidence of this is shown in the initial tie points where the range between the minimum and maximum planimetric differences is 20-30m;

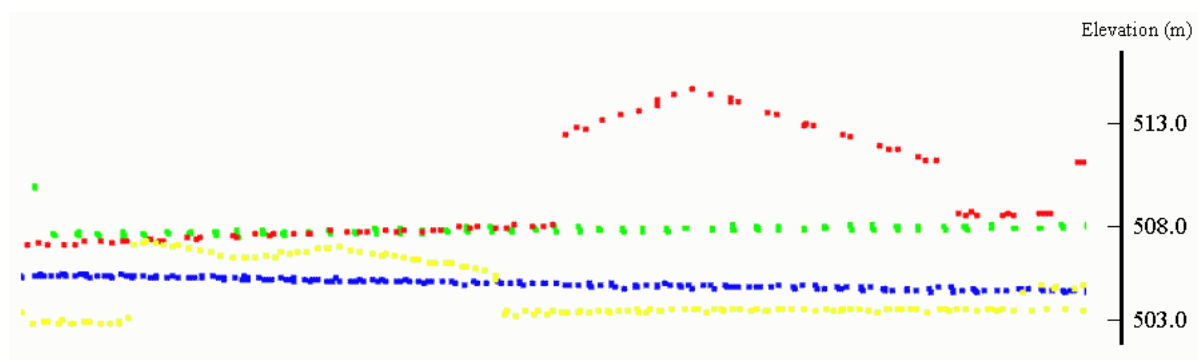


Figure 5-3: Profile of an Uncalibrated ALS dataset

5.1 Adjustment Solution: Boresight Angles Only

Using an initial approximation of (0,0,0) for the boresight values, a solution was determined using the iterative least-squares method, which converged within 11 iterations. All 32 tie points were used resulting in a total of 96 observations; the same number for each consecutive adjustment. With 3 unknowns, the redundancy for the model was 93. The solution is given in Table 5-2.

Table 5-2: Calibration Solution for Angles Only

<i>Angle</i>	<i>Value (degrees)</i>	<i>Std Dev (degrees)</i>
<i>Roll</i>	-1.17239	0.001314
<i>Pitch</i>	1.29148	0.002139
<i>Heading</i>	-0.28188	0.008288

The standard deviations from the solution immediately show that heading is the weakest component of the solution – almost by a factor of 4. This can be explained by the dependency of the heading on the planimetric quality of the tie points (Section 3.4). As the estimated standard deviation was 5 times larger than the elevation accuracy (Section 4.4), it is clear that the heading would be the poorest determined parameter. The error associated

with the selection of the tie points, reflected in the planimetric weights, reduces the precision of the heading solution. However, the standard deviation of the heading is close to the error estimate of the navigation solution of 0.008 degrees in heading. This suggests that despite the tie point selection, the solution may be nearing its resolvable precision. The standard deviation of the roll error demonstrate that this is the most well-determined parameter. As the roll induces the largest elevation differences in the tie points, it has the largest ‘signal’ to manipulate – resulting in a more precision solution. Although the pitch standard deviation is larger than the roll, it is still below the navigation pitch error of 0.005 degrees. This suggests that the data collection at different altitudes is successful in separating out the pitch error ‘signal’.

After adjusting the flight strips with the boresight solution, the analysis criteria relate the large change on the elevation surfaces. The tie points show a much better agreement with an average planimetric difference of 0.66m and an average elevation difference of 0.14m. Their values are given in Table 5-3. The planimetric difference of the tie points of 0.66m is larger than expected (0.5m) and is an early indication that some additional error may remain in the solution.

Table 5-3: Tie Point Differences Solving for Angles Only

	<i>X(m)</i>	<i>Y(m)</i>	<i>Z(m)</i>
<i>Average</i>	0.696	0.631	0.140
<i>Std Dev</i>	0.407	0.395	0.105
<i>Minimum</i>	0.075	0.049	0.033
<i>Maximum</i>	1.732	1.743	0.436
<i>Median</i>	0.655	0.700	0.100

At first glance, the control point differences still appear quite large with an average value of -0.620m ; but a review of their distribution (Figure 5-4) quickly shows that the differences are roughly distributed about the average. The standard deviation of 6.3cm suggests a good fit, but the chi-squared goodness-of-fit test for normality fails at all confidence levels. Closer inspection of the distribution shows a small bulge to the left of center (skewness = -0.52) and excess kurtosis of 0.99 , which demonstrates the departure from normal. The average value could be considered the elevation bias of the system, but the residual errors in the ALS calibration may influence the bias value by several centimeters.

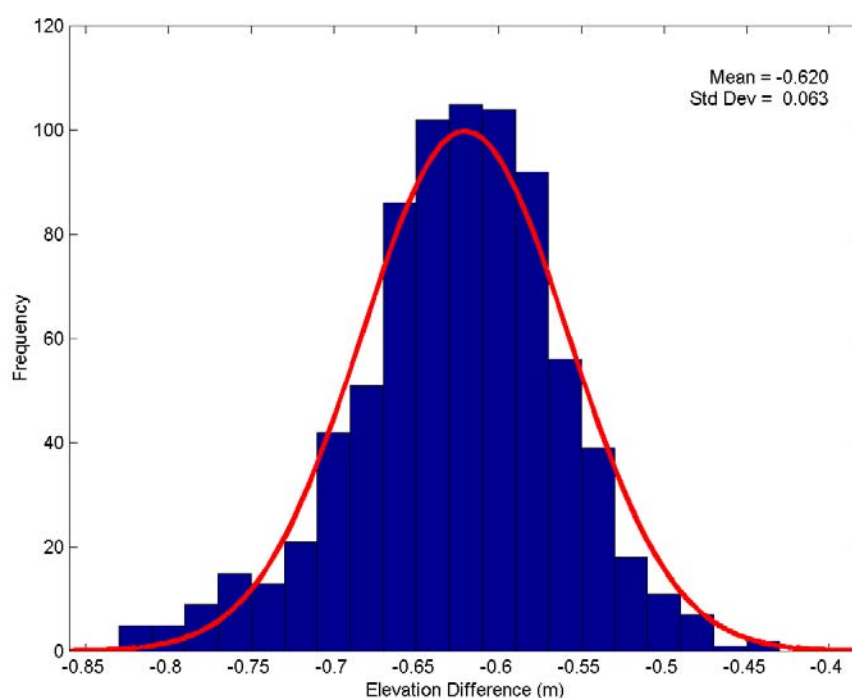


Figure 5-4: Control Point Differences Distribution (Angle Solution Only)

A plot of the strip elevation differences immediately reveals problems with the solution. The distribution is asymmetrical (skewness = 0.18) and has a wide base relative to its peak (excess kurtosis = 8.19): it is decidedly non-Gaussian (Figure 5-5). A mean of 3.6cm suggests that although the tie points were minimized, the differences between entire strips

were not. A standard deviation of 26.6cm further reflects a poor fit when compared to the expected standard deviation of <15cm.

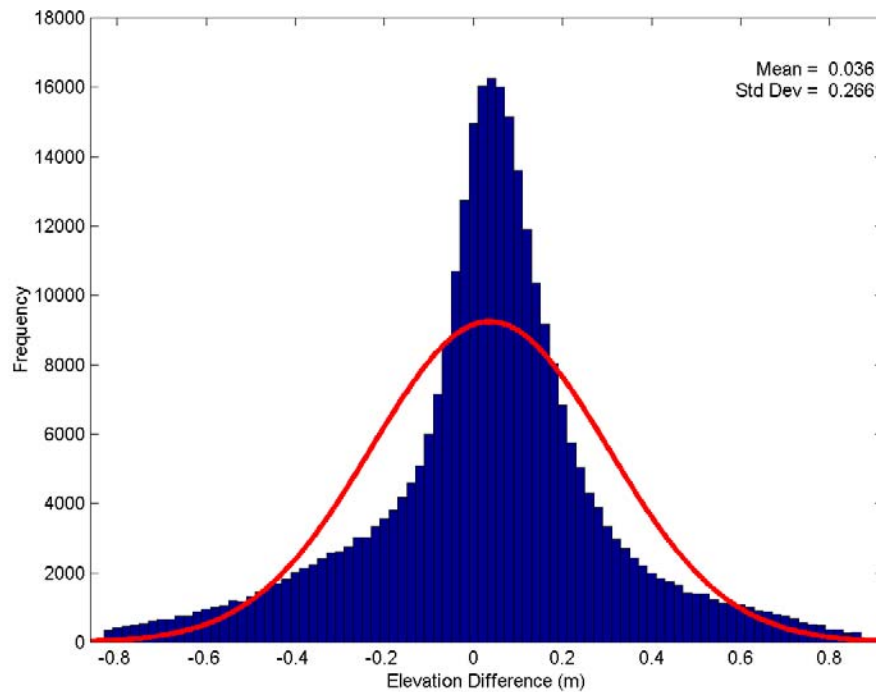


Figure 5-5: Distribution of Relative Elevation Differences Between Adjusted Laser Strips (Angle Only Solution)

The profile plot of the overlapping strips is again the most telling (Figure 5-6). A profile view along the control surface (the runway), with a height exaggeration, clearly shows additional systematic error remaining in the solution. This can be seen by the uplifted edges (the smile) of the strips profiles in across track direction. This effect is the type of effect expected from an unmodeled scanner torsion parameter.

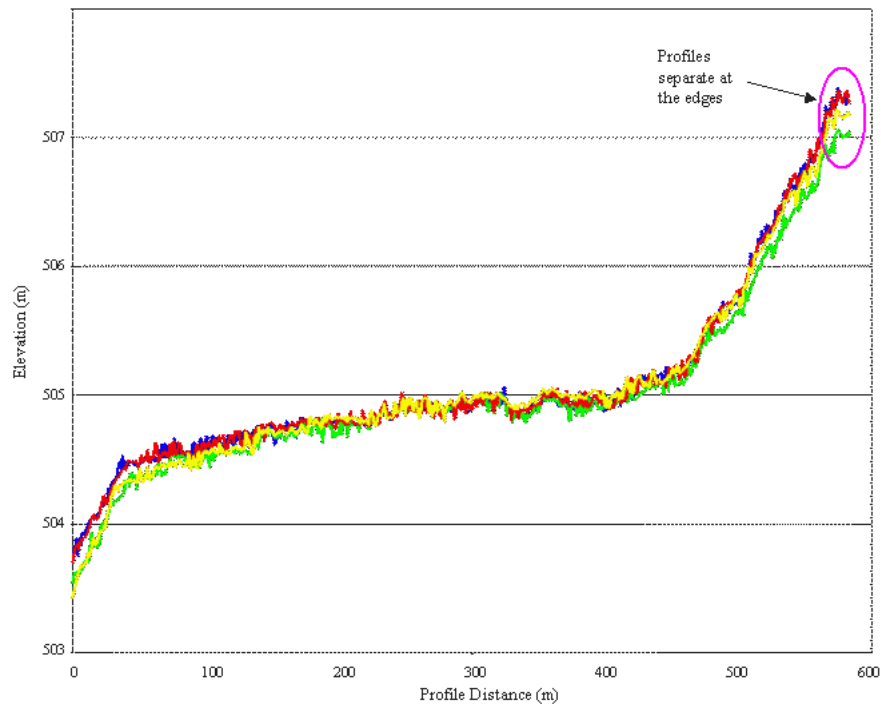


Figure 5-6: ALS Elevation Data Profile (Angle Only Solution)

A plot of the elevation differences also clearly shows errors remaining in the solution (Figure 5-7). For this plot, differences from 0-10cm are coloured green, larger differences are yellow and red. Distinct patterns are visible towards the edges of the overlapping strips. The plot indicates that the near-nadir data agrees, but the edges do not. This confirms the results from the plotted profile (Figure 5-6) and indicates that systematic errors are present in the solution. The areas showing the largest elevation differences are the edges of the strips flown at the higher altitude. This confirms that scanner torsion error increases as a function of flying height.

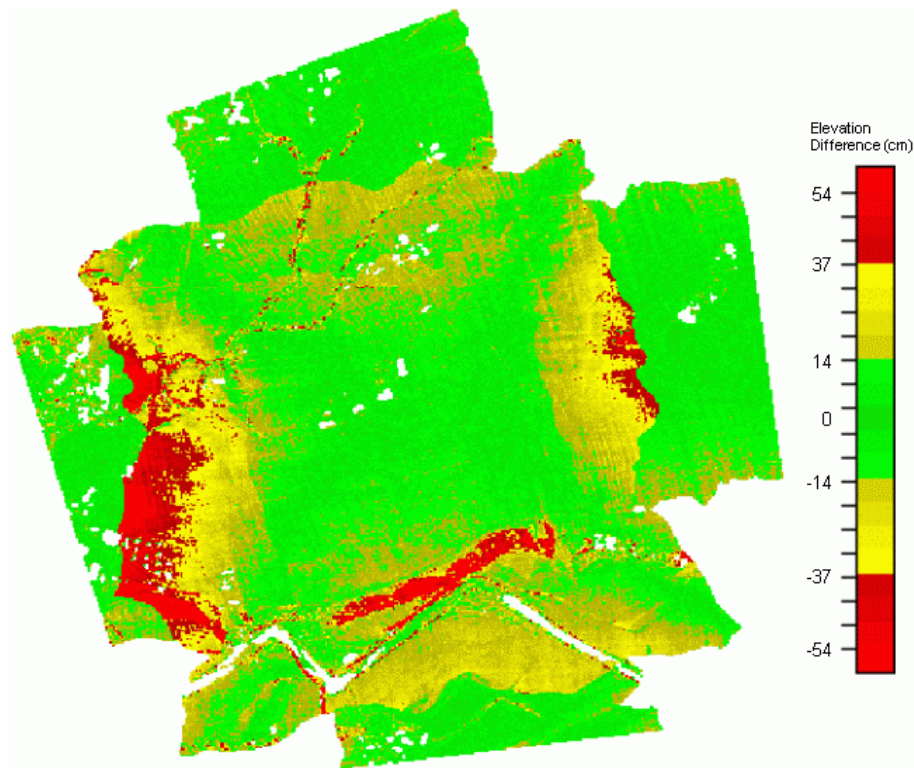


Figure 5-7: Elevation Difference Plot - Angle Only Solution

5.2 Adjustment Solution: Torsion with Fixed Angles

The next adjustment solves for the torsion parameter only. The boresight angles are fixed to the previous solution and the torsion is resolved in the least-squares minimization. The results of this solution are given in Table 5-4.

Table 5-4: Torsion Solution

<i>Parameter</i>	<i>Value</i>	<i>Std dev</i>
<i>Scanner Torsion Constant (unitless)</i>	-4.600×10^{-4}	7.330×10^{-5}

The previous angles only solution was affected by scanner torsion error. The error was most apparent at the edges, but appeared to affect the entire dataset as well. With the inclusion of the torsion in the scanner model, a large reduction in error is apparent. The tie points show a reduction in planimetric misclosure of 0.58m and a large reduction in elevation difference to 3.6cm (Table 5-5). The planimetric differences are still larger than the expected 0.5m, but 8cm smaller than the previous solution. A reduction of 10cm in elevation difference is a first indicator that the model has improved.

Table 5-5: Tie Point Differences with Torsion Correction

	<i>X(m)</i>	<i>Y(m)</i>	<i>Z(m)</i>
<i>Average</i>	0.588	0.579	0.036
<i>Std Dev</i>	0.337	0.350	0.020
<i>Minimum</i>	0.022	0.034	0.008
<i>Maximum</i>	1.679	1.711	0.079
<i>Median</i>	0.545	0.576	0.030

The elevation differences in the control points also show a reduction in size (Figure 5-8). The distribution of the residuals again shows a grouping around a central value; in this case – 0.604m, which is 1.6cm different from the angle only solution. This demonstrates that the apparent bias is composed of the true system elevation bias and a systematic component. The systematic component can be skewed by incorrect modeling of the sensor – thus the bias values changes when the torsion parameter is added. The standard deviation of the control points is only 0.4cm different from the previous solution. The lack of difference may be explained by the fact that the control points are located in the center of the test area, where most of the nadir data is situated. The elevation plots from the angle only solution show that the nadir data was the least affected by torsion error and would not demonstrate a large change in difference. The distribution however has improved. Although a bulge is still

visible to the left, it has narrowed slightly and the resulting skewness is only 0.04, with an excess of kurtosis of 0.46. This resulted in a goodness-of-fit test that passed with a confidence of 8.4%. Although this is a weak fit, it shows an improvement over the angle only solution.

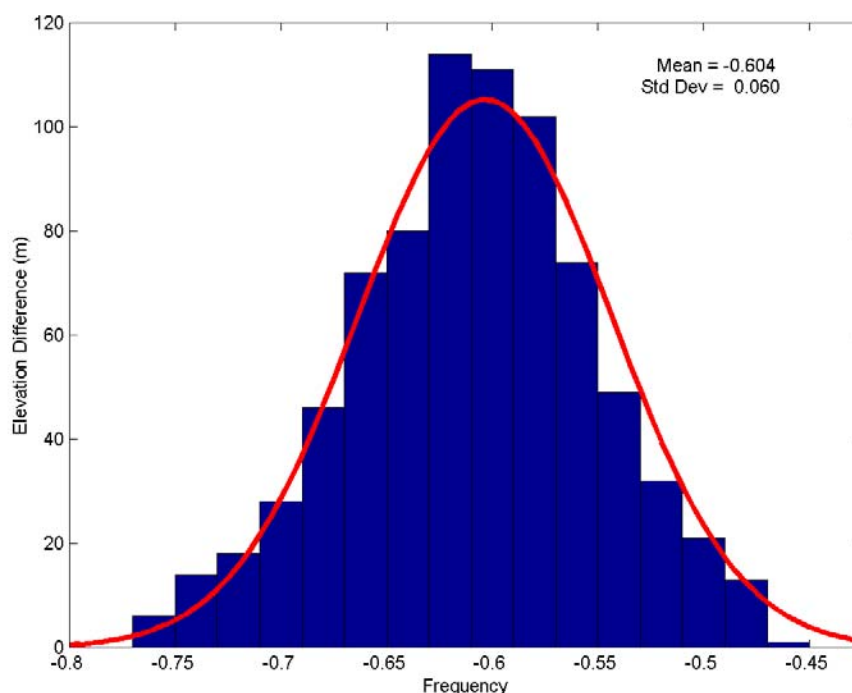


Figure 5-8: Distribution of Control Point Differences (Torsion Correction)

A plot of the strip elevation differences also shows an improvement. This distribution is much more symmetrical and appears more Gaussian in shape with a skewness of -0.08 . The mean value of approximately 0 confirms that the adjustment has minimized the differences between the strips. The standard deviation is also much smaller than the angle only solution. A value of 9.9cm is smaller than the expected value of 15cm and is consistent with an improved calibration. Despite taking on a more bell shaped curve, it is clear by the overlaid normal probability function that the distribution is not Gaussian; this is also confirmed by the

chi-squared test, which fails for all confidence levels. The wide base (excess of kurtosis = 45.05) induces an increase in the standard deviation and the width of the PDF curve, thus causing the test to fail. There is also a remaining bulge to the left of the mean.

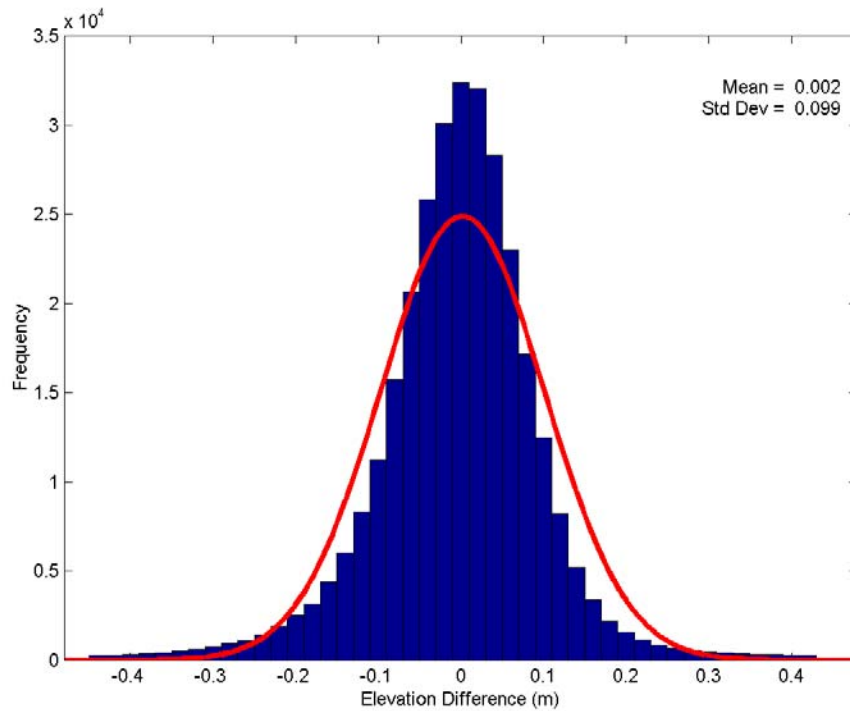


Figure 5-9: Distribution of Relative Differences Between Adjusted Laser Strips (Torsion Correction)

Significantly, the plotted profile (Figure 5-10) shows that the ‘smile’ seen in Figure 5-6, has been greatly reduced. Overlapping profiles now appear to have the same shape, further demonstrating the effect of the torsion parameter.

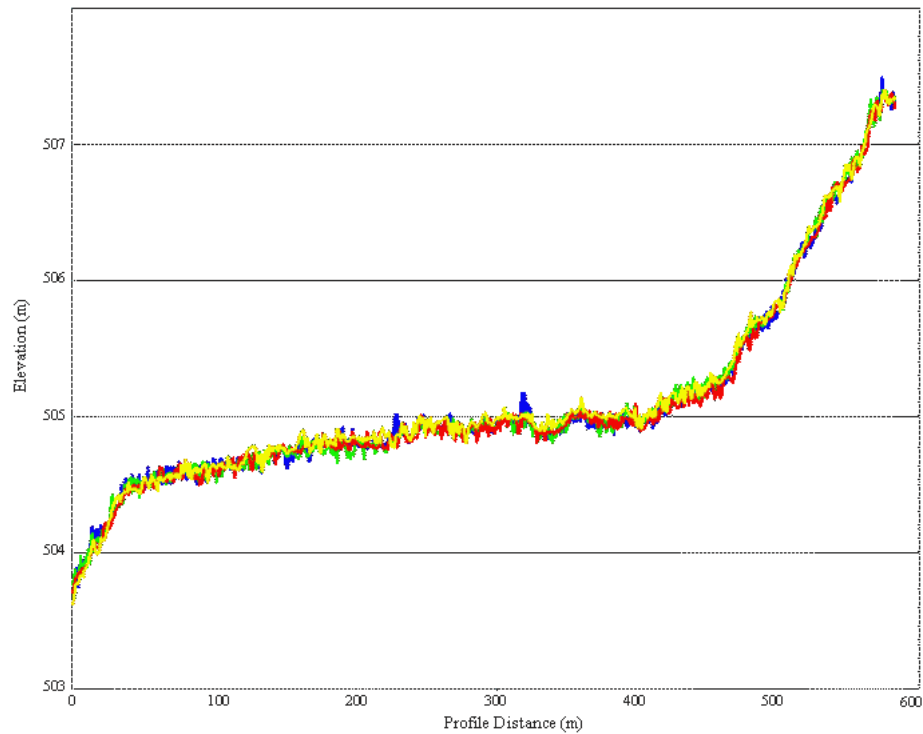


Figure 5-10: ALS Elevation Data Profile (Torsion Correction)

The plot of the elevation differences (Figure 5-11) confirms the edge agreement. Rather than patterns of yellow and red such as in Figure 5-7, the new figure shows an abundance of green; indicating differences less than 10cm. Of note however, are the large elevation differences along the riparian features. This will be explored further in Section 5.4.

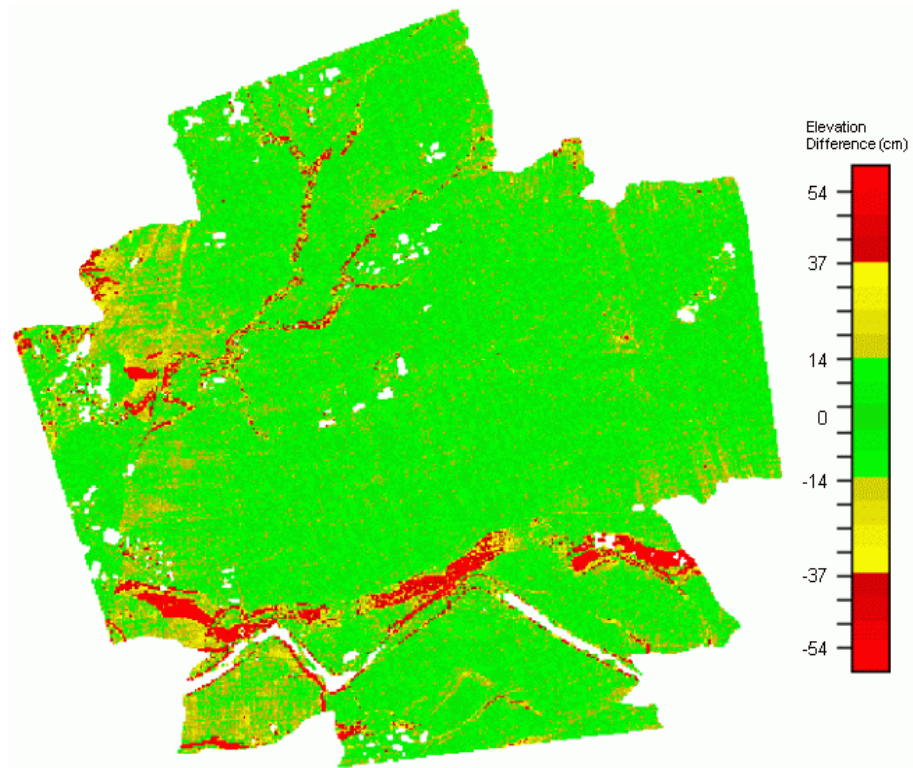


Figure 5-11: Elevation Difference Plot - Torsion Only Solution

5.3 Adjustment Solution: Torsion and Angles

This adjustment allows the errors in the strips to be distributed to all 4 parameters simultaneously, rather than constraining them to go into one place or another. For this adjustment, the initial values for the boresight angles were set to the solution in Step 1, and the torsion estimate to the solution in Step 2. The solution is given in Table 5-6.

Table 5-6: Misalignment Solution with Angles and Torsion

<i>Parameter</i>	<i>Value</i> <i>(degrees)</i>	<i>Std Dev</i> <i>(degrees)</i>
<i>Roll</i>	-1.17080	0.001318
<i>Pitch</i>	1.29208	0.002140
<i>Heading</i>	-0.28032	0.008268
<i>Scanner Torsion Constant (unitless)</i>	-4.6846×10^{-4}	7.3614×10^{-5}

The tie point residuals show no significant improvement from the torsion solution; with an average XY value of 0.58m and an average elevation value of 3.6cm. Based on the tie point values, the simultaneous solution appears to have the same quality as the sequential angle and torsion solutions.

Table 5-7: Tie Point Differences (Combined Solution)

	<i>X(m)</i>	<i>Y(m)</i>	<i>Z(m)</i>
<i>Average</i>	0.589	0.579	0.036
<i>Std Dev</i>	0.332	0.345	0.021
<i>Minimum</i>	0.058	0.057	0.005
<i>Maximum</i>	1.650	1.716	0.073
<i>Median</i>	0.567	0.557	0.031

The control point elevation differences show a small improvement from previous solution, with average value of -0.604m and a standard deviation of 5.9cm (Figure 5-12). With the same value for the mean as the previous solution, the elevation bias in the systems appears to

be sufficiently modeled. The small standard deviation suggests a better fit, and the chi-squared test passes with a confidence level of 20.9%. Although this is again a weak fit, it shows an improvement over the previous solutions. A slight skewing to the left appears evident in the histogram although the skewness calculation results in a value of 0.06, which indicates a slight bulge to the right. The excess kurtosis is 0.48 indicating a ‘peakedness’ which likely explains the weak Gaussian fit.

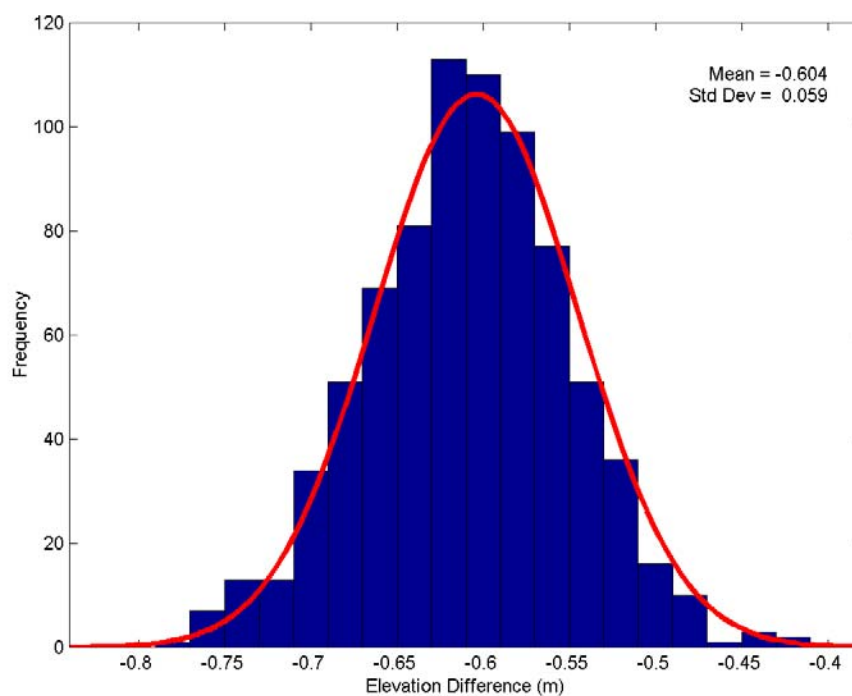


Figure 5-12: Distribution of Control Point Differences (Combined Solution)

The elevation strip differences demonstrate the same distribution as the previous solution. Although bell shaped and with very good symmetry (skewness = -0.01), the wide base relative to the peak (excess kurtosis = 44.71) induces an increase in the standard deviation, which in turn widens the normal probability curve (Figure 5-13). The standard deviation is slightly larger at 10.0cm, but the distribution still fails to pass a chi-squared goodness-of-fit test at any confidence level.

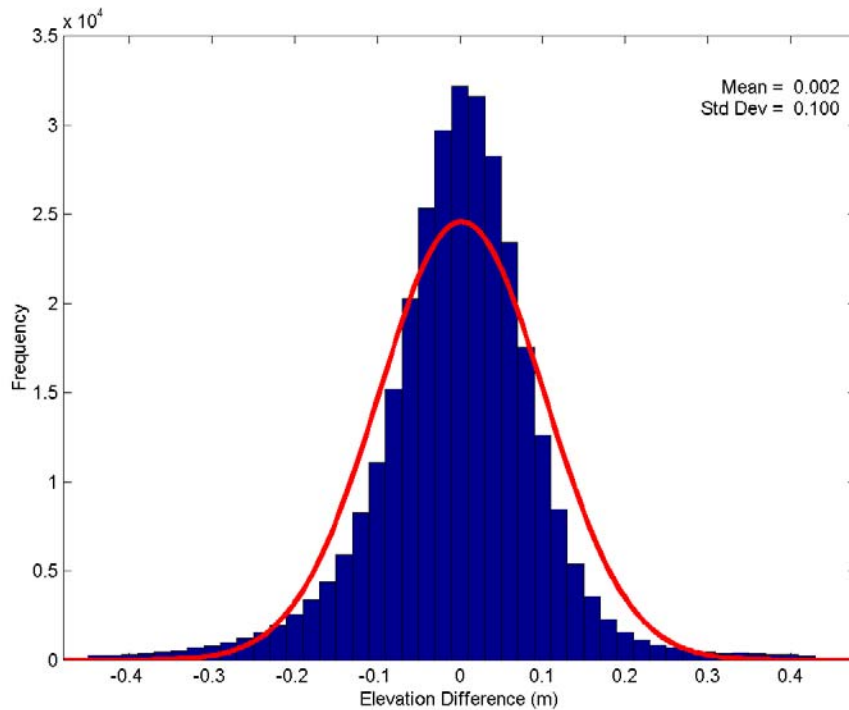


Figure 5-13: Distribution of Relative Differences Between Adjusted Laser Strips (Combined Solution)

The profile plot does not show any significant difference from the previous solution (Figure 5-14). Although the torsion value has changed, the profile plots do not show a large change. This would suggest that torsion parameter is relatively insensitive to small value differences.

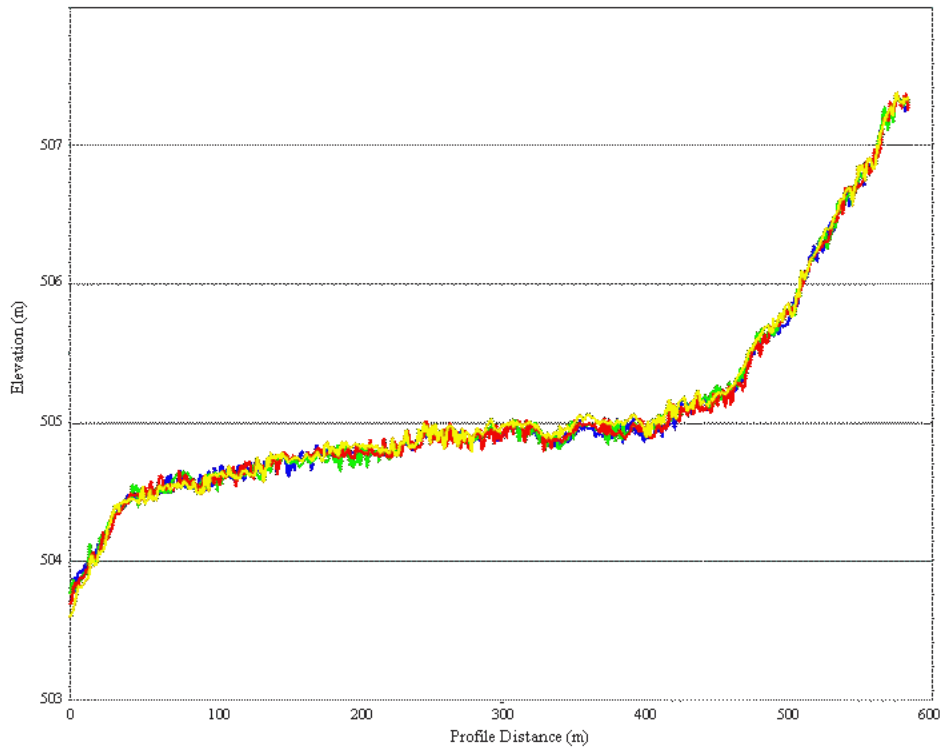


Figure 5-14: ALS Elevation Data Profile (Combined Solution)

The plot of the elevation differences also shows similar results to the torsion only solution. Most of the overlap area is coloured green indicating a difference of less than 10cm. Larger differences (in yellow and red) are again associated with the riparian features.

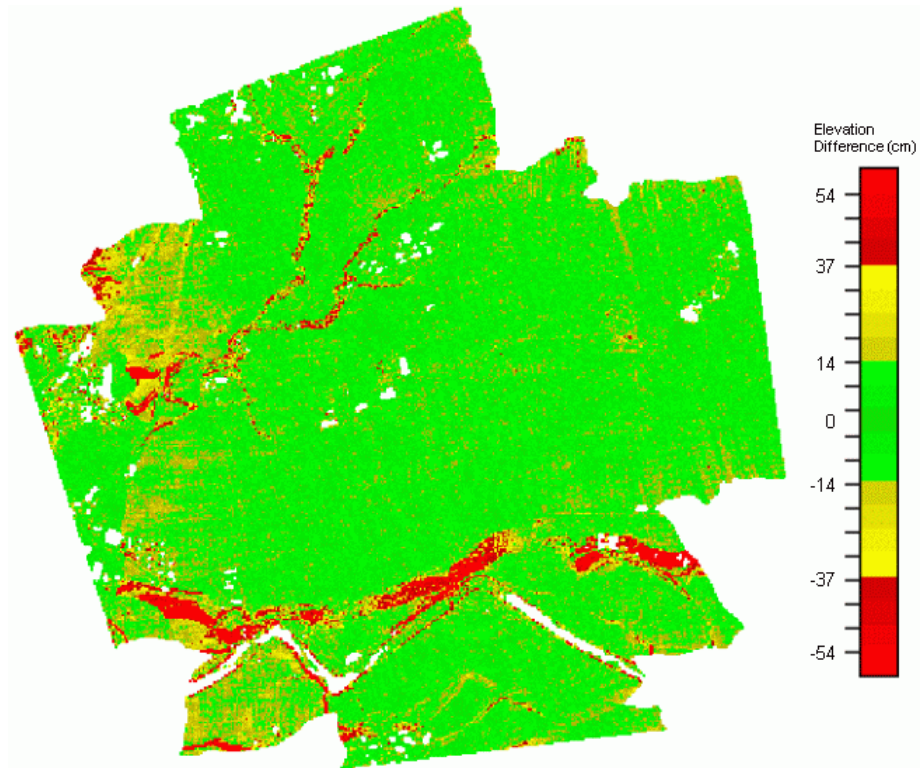


Figure 5-15: Elevation Differences Plot - Combined Solution

5.4 Terrain Effects

As noted above, an inspection of the elevation differences plots (Figure 5-15) shows that large differences between overlapping strips are spatially correlated. By comparing the areas with large differences to the intensity image (Figure 4-1) and the shaded relief image (Figure 4-2), it is clear that the highlighted areas are on terrain with a high slope aspect. This phenomenon can be explained by exploring the interaction of an ALS pulse with a sloped terrain (Figure 5-16).

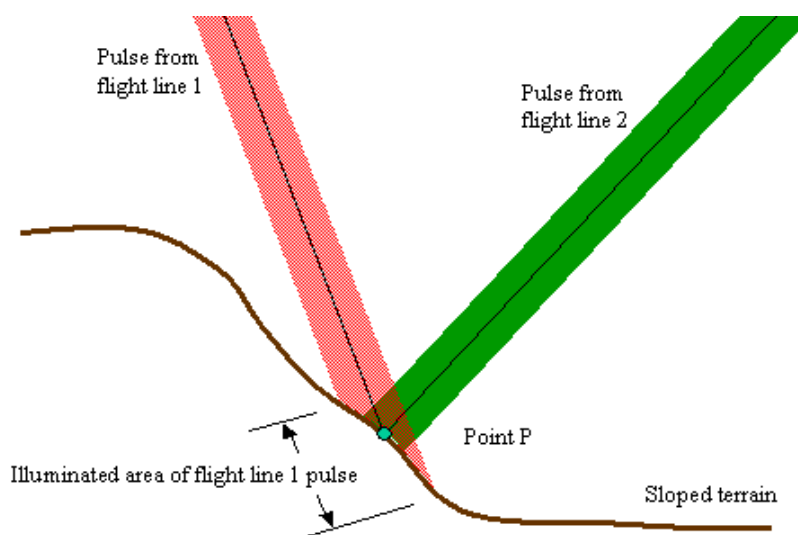


Figure 5-16: Pulse Returns from Sloped Terrain

The energy in a laser pulse will diverge through the air at a determined rate. This causes an illuminated laser footprint on the ground with a width of 0.3-1m (Section 2.1.1). In the case of two flight lines observing the same point P (Figure 5-16), different areas will be illuminated by the footprint. In the case of flight line 2, the pulse hits the ground at a right angle and the energy is returned. For flight line 1, the pulse hits the ground at an acute angle, causing an area down the slope to be illuminated. The energy that returns up the transmitted path will contain the combined reflections from the energy footprint. This creates an ambiguity – does the ALS system record a distance to the top left edge of the footprint, the bottom right or something in between? The elevation differences from Figure 5-15 suggest that the ambiguity remains in the solution, and degrades measurements on highly sloped terrain.

With the slope effect identified, an analysis of the elevation differences in areas of common slope aspects is required. Figure 5-17 shows the distribution of elevation differences between strips in the central area of the test data, over relatively flat terrain.

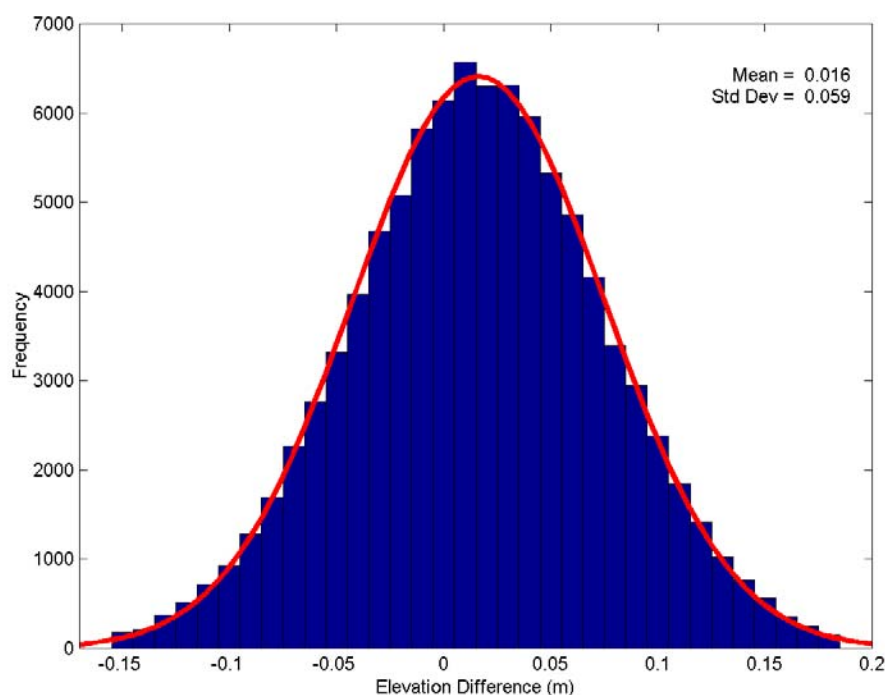


Figure 5-17: Elevation Differences of Flat Terrain

The distribution of differences over flat terrain shows an obvious Gaussian trend. The mean is 1.6cm; which can be explained from the fact that this analysis deals with only a subsection of the data – so the mean represents a local variation. The standard deviation is small than the distribution from the overall plot, measuring 5.9cm compared to 10.0cm for all data. Despite the apparent trend however, this distribution fails the chi-squared goodness-of-fit tests for all confidence levels. It has a skewness of -1.36 and an excess of kurtosis of 34.68. The trend is clear however, and suggests that the large departure from normal in the overall data analysis is caused by errors in the sloped regions.

Figure 5-18 shows the distribution of elevation differences between strips along the escarpment area in the southern part of the test data.

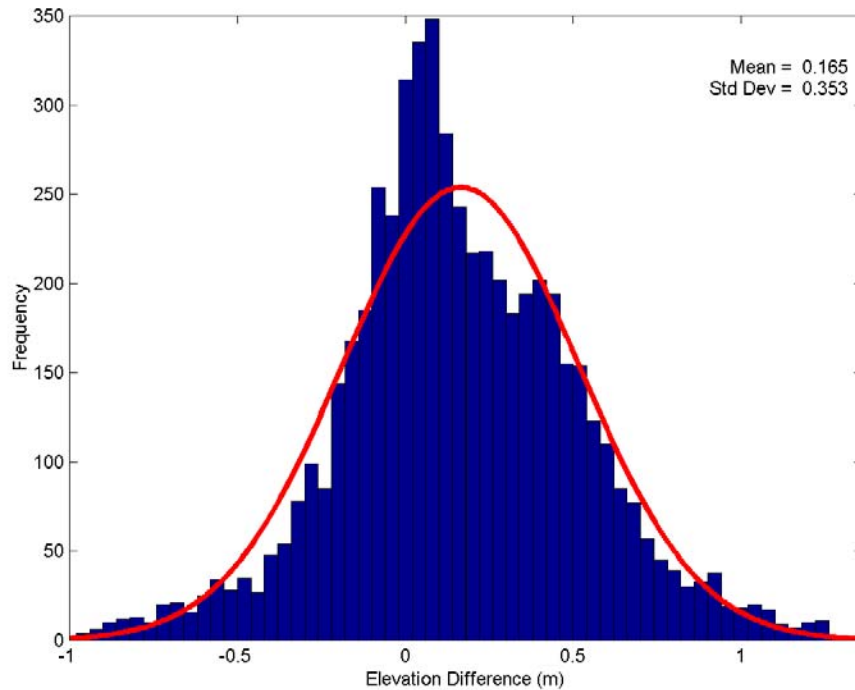


Figure 5-18: Elevation Differences Over Sloped Terrain

The plot shows an asymmetrical distribution with a mean of 16.5cm and a standard deviation of 35.3cm. The distribution fails the normal fit both by the chi-squared test and by visual inspection. It has a skewness of 1.26 and an excess of kurtosis of 11.18. The plot further confirms that elevation errors are greater in high-sloped regions than on flat terrain.

An important conclusion from the slope effect must be considered for calibration. Previous calibration methods (Burman 2000, Vosselman and Maas 2000) have suggested that strips should be compared at locations with large elevation gradients. The results above however, show that areas with large gradients are prone to greater measurement error due to the ambiguity of the laser footprint. Tie points must be collected in flat areas to reduce measurement errors and generate the highest quality calibration. The use of strips flown at

different altitudes provides sufficient decorrelation of the data to determine the calibration parameters.

5.5 Summary of Results

The addition of the torsion parameter clearly improves the calibration results. The improvement can be seen in the statistical measures and in the plots. The following table summarizes the calibration results (Table 5-8). The boresight angle only solution, which was the equivalent of previously suggested calibration methods in literature, shows a clear improvement over the uncalibrated data. The addition of the torsion parameter however, shows that a significant amount of error remained in the previous model, and could be recovered as a torsion scanner error. The combined boresight and torsion solution shows a small improvement over sequentially derived parameters, suggesting that a simultaneous solution is best for an ALS calibration.

Table 5-8: Solution Comparison

<i>Model</i>	<i>Tie Pts Residuals (m)</i>	<i>Control Points Differences (m)</i>	<i>Elevation Differences (m)</i>
<i>Uncalibrated</i>	XY: 25.50 Z: 6.44	Z: -0.906 ± 2.47	
<i>Angles Only</i>	XY: 0.663 Z: 0.140	Z: -0.620 ± 0.063	Z: 0.036 ± 0.266
<i>Torsion</i>	XY: 0.584 Z: 0.036	Z: -0.604 ± 0.060	Z: 0.002 ± 0.099
<i>Angles and Torsion</i>	XY: 0.587 Z: 0.036	Z: -0.604 ± 0.059	Z: 0.002 ± 0.100

The elevation difference criteria gives a direct measure of what kind of accuracy can be expected with this ALS sensor using the derived calibration. Although this measure only indicates vertical accuracy, errors in horizontal alignment cause elevation differences, thus it

can be used as a general quality criterion. The elevation difference plots clearly indicated a spatial correlation of elevation differences and sloped terrain. A further analysis showed that flat terrain was measured more consistently with an ALS sensor than over sloped terrain.

5.6 Scanner Operating Parameters Effect on the Calibration Parameters

For this test, data was collected with an ALS system operating with a fixed set of parameters for pulse rate, scan rate, FOV and flying speed. Changing some of the sensor parameters can affect the calibration and derived ground point accuracies. A general affect of all these parameters is that any change will alter the density of the points on the ground. As these points are then observed to derive the calibration parameters, any change in density will affect the solution; even if there is no true physical change in the calibration. Additional effects include:

- **Pulse rate**

Changing the pulse rate of the laser will increase or decrease the number of points measured. When calibrating, the highest pulse rate should be used to reduce interpolation errors when picking tie points. However, the pulse rate has no mechanical effect on the sensor, thus their would not be a physical change in the calibration parameters.

- **Scan rate**

The scan rate determines how fast the scan mirror will be accelerating and decelerating. The accelerations produce the bending effect in the connecting parts, which is modeled by the torsion parameter. The torsion model in this project is dependent on a particular scan rate; thus a new parameter would have to be derived for different rates. A scan-rate independent model would be an area of further research.

- **Field of View**

A larger field of view causes the measurements towards the edge of the scan strip to have a longer slant range. If any errors are present in the sensor model, the larger slant range will show the effects of the errors to a greater degree. Although a wider strip may appear to have different error effects, the FOV alone does not affect the sensor model.

- **Flying Height**

A change in flying height using an uncalibrated sensor model will produce elevation and horizontal differences in the data strip, which are proportional to the altitude of the aircraft. Indeed, the calibration method in this thesis leveraged these differences to decorrelate the boresight parameters. Changing the flying height after calibration will not affect the quality of the boresight solution. However, additional errors may be observed with more atmospheric propagation effects. Provided the atmosphere is well modeled by the standard equations during the observation epochs, the accuracy of the ground points should only decrease by 1-4cm (LH Systems 2001).

- **Flying Speed**

Changing the flying speed of the aircraft will increase or decrease the ground point spacing. The effect of this is similar to changing the pulse rate. Because the flying speed does not have a mechanical effect on the laser, the accuracy of the ground points will be unaffected.

5.7 Remaining errors

Despite the improved results, error still remains in the sensor model. The errors can be visualized most dramatically by taking a profile of a peaked roof building in an overlapped area (Figure 5-19).

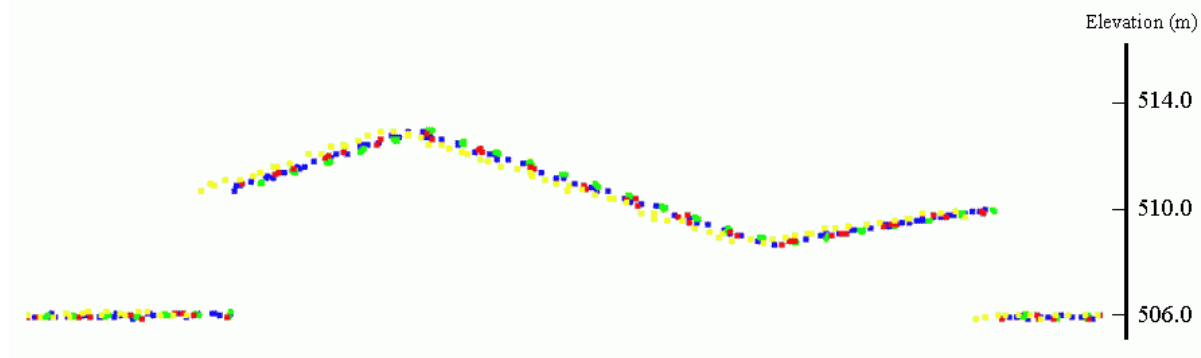


Figure 5-19: Remaining Error Effects

The profile shows that different flight lines (red, green, blue and yellow) do not match up perfectly over the peaked roof area. Due to the orientation of the profile with respect to the flying direction, the error appears to be caused by an incorrect pitch determination. Interestingly however, only 1 flight line deviates from the correct location; and the ground surrounding the building appears correct. Several attempts were made to observe buildings such as these in the data set, and force them to align by manually adjusting the pitch boresight angle and holding it fixed during the least-squares adjustment. Although this method aligned the building in question, the quality of the data everywhere else in the strips heavily degraded. The conclusion therefore, was that an additional error source is present in the data, and that the current calibration method attempts to minimize the effects of the other error sources within the 4 model calibration parameters.

One potential source of error would arise from an offset between the IMU and scanner frames and/or offset to the GPS antenna. In this thesis, the horizontal offset errors were measured or assumed to be zero. If they were not so, their effect would degrade the planimetric accuracy of the system. Alternatively several authors have suggested that the IMU drift rates could be a further source of error (Toth et al. 2001, Behan et al. 2000). A time dependent effect would explain why most of the data appears correct, while only some data in random locations appears to be incorrect. Previous attempts to model IMU error involved adjusting the data in a post-calibration phase, and applying corrections on a strip-wise basis. The goal of this thesis was to determine a set of fixed parameters that could be used on a global (project) basis. Nonetheless, IMU errors cause by gyro-drift or misalignment will always be present in calibration data – and any calibration parameters derived from that data would be affected and possible biased by the IMU. This may also account for the non-Gaussian distribution of elevation differences seen in the results above. With the random nature of IMU errors however, a question arises as to whether an unbiased calibration can ever be obtained. Despite these questions, the method derived in this thesis still provides an acceptable solution.

Chapter 6

Conclusions and Recommendations

In this thesis, a new sensor calibration model for Airborne Laser Scanners (ALS) was described. This was undertaken because current models do not adequately account for all of the observed systematic errors in the derived ground points of ALS systems. A practical method of calibrating the sensor was also described. This addresses the lack of a systematic method of calibrating ALS sensors in industry, and provides a solution with statistical measures to judge the quality of the results.

6.1 Conclusions

The new sensor model was successfully implemented and an analysis of the results yields several conclusions. These are summarized below:

- **Use of intensity information**

Previous calibration methods did not have access to, or did not chose to use the intensity information available from the laser data of the ALS system. By interpolating this data into a regular grid, a grayscale image is formed which is very

similar to standard panchromatic photogrammetric images. The similarity was further exploited by using the intensity images in custom and commercially available photogrammetric softcopy programs to manually observe common points between overlapping areas. Thus the intensity information was shown to be of high value for calibration purposes.

- **Calibration accuracies**

Although variance information was generated for the calibration parameters, the best measure of their quality is the difference between the ground point elevations of overlapping strips. Solving for boresight angles only, the average tie point difference between strips was 13.4cm. By including the new parameter for torsion the elevation differences were reduced to 3.6cm. The standard deviation for elevation differences between strips was reduced from 26.6cm for angles only, to 10.0cm with the inclusion of the torsion parameter. The torsion parameter, in its current model, is dependent on scan rate/FOV, thus the calibration must be redone when that sensor mode changes. Changes in flying height or speed will affect the density of the points used to derive the calibration parameters; but will not have a physical effect on the calibration parameters.

- **Terrain induced error**

Graphic plots of the elevation differences clearly showed a spatial correlation between vertical differences and terrain slope. Further analysis suggested ambiguity arises from measuring a sloped terrain from an acute angle. Performing analyses on separate flat and sloped terrain revealed that the standard deviation was much lower over flat terrain (5.9cm) and higher over sloped terrain (35.3cm).

6.2 Specific Contributions

Over the development of the thesis, several problems that exist in industry were discussed. The solutions are summarized as follows:

- **New Scanner model**

A review of literature suggests that this is the first attempt at modeling the scanner mirror errors in ALS systems. Although an analysis of several effects from scanner errors were described, the largest source of systematic error was deemed to come from a torsion effect on the lever arm connecting the scanner mirror and the scan angle encoder. A review of initial calibration data confirmed this effect, and a model was derived which successfully corrected the observed error.

- **Calibration flight plan**

The quality of the calibration will be dependent on how the flight planning of the overlapping areas contributes to identifying and decorrelating specific error sources. A review of literature shows that very little has been published in this area; specifically establishing a link between flight characteristics and parameter correlation. In this thesis, an optimal flight plan was derived for the purposes of maximizing the quality of calibration results. The flight plan was then used to collect the data in the thesis.

- **Tie point selection**

Previously proposed calibration methods have suggested comparing ALS strips over areas with large elevation gradients. An analysis of spatial distributed errors in this thesis strongly suggest that strips should be compared over flat areas, due to the large ambiguities associated with measurements on sloped terrain.

- **Calibration methodology**

Currently the most widely used method of ALS calibration is a tedious manual adjustment. This thesis proposed and implemented a more rigorous method, and created custom software that facilitated a swift solution. Previously, a manual calibration could take 8-12 hours. Using the method employed in this thesis, a calibration can be undertaken in 1-2 hours.

6.3 Future Investigations

The calibration method described in this thesis is entirely useful in its current state. Review of the results, and experiences during implementation provide ideas for future investigation. Specific ideas are:

- **Scan rate independent model of torsion error**

Clearly a torsion model that is independent of the scan rate would be desirable. Although in principle such a model should be simple to derive, the ALS manufacturers generally do not publicly release the specific mathematical formulation used in their scanner model.

- **IMU modeling**

An additional error source was detected in the results that could be explained by drift rates in the IMU. One area of investigation would be to try to model out these errors during the calibration. The addition of new parameters however, will increase the variance of the boresight and torsion parameters.

- **Automated point measurement**

The manual measurement of tie points is a time consuming component of this method. The pre-analysis also shows that any errors in the tie point observations will degrade the calibration solution. An automated method of extracting tie points would be desirable to eliminate the step from the calibration. An increased number of points would also provide more redundancy and improve the quality of the calibration parameters.

References

- Ackermann, Freidrich. "Airborne laser scanning - present status and future expectations." *ISPRS Journal of Photogrammetry & Remote Sensing*, V54. Elsevier (1999): 64-67.
- Applanix, "Applanix Home Page." <http://www.applanix.com>. Internet website. Visited Sep 2002.
- Axelsson, P. "DEM Generation from Laser Scanner Data Using Adaptive TIN Models." *International Archives of Photogrammetry and Remote Sensing, Vol. XXXIII, Part B3, Amsterdam*. CDROM (2000).
- Axelsson, P. "Processing of laser scanner data - algorithms and applications." *ISPRS Journal of Photogrammetry & Remote Sensing*, V54. Elsevier (1999): 138-147.
- Baltsavias, E.P. "A comparison between photogrammetry and laser scanning." *ISPRS Journal of Photogrammetry & Remote Sensing*, V54. Elsevier (1999): 83-94.
- Baltsavias, E.P. "Airborne laser scanning: basic relations and formulas." *ISPRS Journal of Photogrammetry & Remote Sensing*, V54. Elsevier (1999): 199-214.
- Behan, A. "On the Matching Accuracy of Rasterised Scanning Laser Altimeter Data." *International Archives of Photogrammetry and Remote Sensing, Vol. XXXIII, Part B3, Amsterdam*. CDROM (2000).
- Behan, A., Mass, H-G, Vosselman, G. "Steps towards Quality Improvement of Airborne Laser Scanner Data." *Internet Publication*. Delft University of Technology, Faculty of Civil Engineering and Geosciences, Section of Photogrammetry and Remote Sensing (2000).

- Bentley, "Bentley MicroStation Home Page." <http://www2.bentley.com/>. Internet website. Visited Sep. 2002.
- Berg, R., Ferguson, J. "Airborne Laser Mapping for Highway Engineering Applications." *Proceedings of the ASPRS Annual Convention, St. Louis, USA*. ASPRS, CDROM (2001).
- Brandt, S., Vosen, P. "Combined Application of Aerophotogrammetry, Laser Scanning and Dynamic Segmentation to Reconstruct Three-Dimensional Watercourse Networks." *International Archives of Photogrammetry and Remote Sensing, Vol. XXXIII, Part B3, Amsterdam*. CDROM (2000).
- Briese, C., Pfeifer, N. "Airborne Laser Scanning and Derivation of Digital Terrain Models." *Proceedings of the Optical 3D Measurement Techniques V, Oct. 1-4*. Vienna, Austria (2001): 80-87.
- Brugelmann, R. "Automatic Breakline Detection from Airborne Laser Range Data." *International Archives of Photogrammetry and Remote Sensing, Vol. XXXIII, Part B3, Amsterdam*. CDROM (2000).
- Burman, H. "Adjustment of Laser Scanner Data for Correction of Orientation Errors." *International Archives of Photogrammetry and Remote Sensing, Vol. XXXIII, Part B3, Amsterdam*. CDROM (2000).
- Burman, H. *Calibration and Orientation of Airborne Image and Laser Scanner Data Using GPS and INS, Dissertation*. Stockholm: Royal Institute of Technology, Department of Geodesy and Photogrammetry, 2000.
- Cannon, M.E. *ENGO 561: Satellite Positioning Notes*. Calgary: The University of Calgary, Department of Geomatics Engineering, 1999.
- Casella, V., Spalla, A. "Estimation of Planimetric Accuracy of Laser Scanning Data. Proposal of a Method Exploiting Ramps." *International Archives of Photogrammetry and Remote Sensing, Vol. XXXIII, Part B3, Amsterdam*. CDROM (2000).
- Cavazzini, A., Gentili, G., et al. "Application of Laserscan to Flood Mapping of an Urban Stream." *International Archives of Photogrammetry and Remote Sensing, Vol. XXXIII, Part B3, Amsterdam*. CDROM (2000).
- Chapman, M. *ENGO 431: Analytical Photogrammetry Notes*. Calgary: The University of Calgary, Department of Geomatics Engineering, 1996.
- Che, W., Nakane, T. "Modeling the Major Japanese Cities in 3D by LIDAR and Digital Camera Images." *Proceedings of the Optical 3D Measurement Techniques V, Oct. 1-4*. Vienna, Austria (2001): 111-117.

- Crombaghs, M.J.E., Brugelmann, R., de Min, E.J. "On the Adjustment of Overlapping Strips of Laseraltimeter Height Data." *International Archives of Photogrammetry and Remote Sensing, Vol. XXXIII, Part B3, Amsterdam*. CDROM (2000).
- Elberink, S., Mass, H-G. "The Use of Anisotropic Height Texture Measures for the Segmentation of Airborne Laser Scanner Data." *International Archives of Photogrammetry and Remote Sensing, Vol. XXXIII, Part B3, Amsterdam*. CDROM (2000).
- El-Sheimy, N., "Digital Terrain Models: Lecture Notes ENGO 579." *Department of Geomatics Engineering, University of Calgary*. Sep. 1998.
- Favey, E., Pateraki, M. et al. "Surface Modeling for Alpine Glacier Monitoring by Airborne Laser Scanning and Digital Photogrammetry." *International Archives of Photogrammetry and Remote Sensing, Vol. XXXIII, Part B3, Amsterdam*. CDROM (2000).
- Flood, M., Gutelius, B. "Commerical Implications of Topographic Terrain Mapping Using Scanning Airborne Laser Radar." *Photogrammetric Engineering and Remote Sensing*. ASPRS (Apr. 1997): 327-366.
- Foley, R., "STRENGTH OF MATERIALS - ON THE WEB", <http://physics.uwstout.edu/StatStr/index.htm>, *University of Wisconsin, Stout*, accessed July 29, 2002.
- Geibel, R., Stilla, U. "Segmentation of Laser Altimeter Data for Building Reconstruction: Different Procedures and Comparison." *International Archives of Photogrammetry and Remote Sensing, Vol. XXXIII, Part B3, Amsterdam*. CDROM (2000).
- Gutelius, B. "Engineering Applications of Airborne Scanning Lasers: Reports from the Field." *Photogrammetric Engineering and Remote Sensing*. ASPRS (Apr-98): 246-253.
- Haala, N., Brenner, C. "Extraction of buildings and trees in urban environments." *ISPRS Journal of Photogrammetry and Remote Sensing, vol. 54*. Elsevier (1999): 130-137.
- Haala, N., Brenner, C. "Generation of 3D City Models from Airborne Laser Scanning Data." (1997).
- Hibbeler, R. *Engineering Mechanics: Statics and Dynamics*. Sixth Edition. Don Mills: Maxwell Macmillan Canada, 1992.
- Hill, J., Graham, L, Henry, R. "Wide-Area Topographic Mapping and Applications Using Airborne Light Detecton and Ranging (LIDAR) Technology." *Photogrammetric Engineering and Remote Sensing*. ASPRS (Aug. 2000): 908-914.

- Hofton, M.A., Blair, J.B., et al. "An airborne scanning laser altimetry survey of Long Valley, California." *International Journal of Remote Sensing*, Vol. 21, No. 12. (2000): 2413-2437.
- Hu, Y., Xue, Y, Fang, K., Pan, Z. "Scanning Laser Altimeter in Airborne Scanning Laser Ranging-Imaging Sensor." *Proceedings of the Fourth International Airborne Remote Sensing Conference and Exhibition*. Canadian Symposium on Remote Sensing, Ottawa, Canada (1999): I 510-517.
- Hyypä, J., Hyypä, H., Ruppert, G. "Automatic Derivation of Features Related to Forest Stand Attributes Using Laser Scanner." *International Archives of Photogrammetry and Remote Sensing*, Vol. XXXIII, Part B3, Amsterdam. CDROM (2000).
- INPHO. "INPHO GmbH Home Page." <http://www.inpho.de>. Internet website. Visited Sep. 2002.
- IntegriNautics, "IntegriNautics Home Page." <http://www.integrinautics.com/>. Internet website. Visited Sep. 2002.
- Intermap Technologies. "Intermap Technologies Home Page." <http://www.intermaptechnologies.com>. Internet website. Visited Sep. 2002.
- Kager, H., Kraus, K. "Height Discrepancies between Overlapping Laser Scanner Strips." *Proceedings of the Optical 3D Measurement Techniques V, Oct. 1-4*. Vienna, Austria (2001): 103-110.
- Kilian, J, Haala, N., Englich, M. "Capture and evaluation of airborne laser scanner data." *International Archives of Photogrammetry and Remote Sensing*, Vol. XXI, Part B3, Vienna, Austria. (1996): 383-388.
- Krabill, W.B., Wright, C.W., et al. "Airborne Laser Mapping of Assateague National Seashore Beach." *Photogrammetric Engineering & Remote Sensing*, v. 66, No. 1. ASPRS (Jan-00): 65-71.
- Krakiwsky, E.J., M.A. Abousalem. *ENGO 361: Adjustment of Observations*. Calgary: The University of Calgary, Department of Geomatics Engineering, 1995.
- Kraus, K, Reiger, W. "Processing of laser scanning data for wooded areas." (2000): 221-231.
- Kraus, K. *Photogrammetry Volume 1: Fundamentals and Standard Processes*. English Edition. Köln: Dümmler, 2000.
- Kraus, K. *Photogrammetry Volume 2: Advanced Methods and Applications*. Fourth (English) Edition. Bonn: Dümmler, 1997.

- Kraus, K., Pfeifer, N. "Determination of terrain models in wooded areas with airborne laser scanner data." *ISPRS Journal of Photogrammetry and Remote Sensing*, vol. 53. Elsevier (1998): 193-203.
- Kuang, S., "Geodetic Network Analysis and Optimal Design. Concepts and Applications." *Ann Arbor Press*. Michigan (1996).
- Lee, I., Schenk, A. "Autonomous Extraction of Planar Surfaces from Airborne Laser Scanner Data." *Proceedings of the ASPRS Annual Convention, St. Louis, USA*. ASPRS, CDROM (2001).
- Leica Geosystems, 2002. "Leica Geosystems / LH Systems Home Page". *Leica Geosystems Inc*. URL <http://www.lh-systems.com>.
- LH Systems, "ALS40 Hardware Demonstration." *Oral Presentation by Ron Roth, Senior Engineer*. LH Systems User's Group Meeting. San Diego (2001).
- Lohmann, P., Koch, A., Schaeffer, M. "Approaches to the filtering of Laser Scanner Data." *International Archives of Photogrammetry and Remote Sensing, Vol. XXXIII, Part B3, Amsterdam*. CDROM (2000).
- Maas, H.G. "Methods for Measuring Height and Planimetry Discrepancies in Airborne Laserscanner Data." *Photogrammetric Engineering and Remote Sensing*. ASPRS, (Sep. 2002): 933-940.
- Maas, H-G, Vosselman, G. "Two algorithms for extracting building models from raw laser altimetry data." *ISPRS Journal of Photogrammetry and Remote Sensing*, vol. 54. Elsevier (1999): 153-163.
- Masaharu, H., Hasegawa, H. "Three-Dimensional City Modeling from Laser Scanner Data by Extracting Building Polygons using Region Segmentation Method." *International Archives of Photogrammetry and Remote Sensing, Vol. XXXIII, Part B3, Amsterdam*. CDROM (2000).
- Mass, H-G. "Filtering of laser altimetry data." *Internet Publication*. Technical University of Delft, <http://www.geo.tudelft.nl> (2001).
- Mass, H-G. "Least-Squares Matching with Airborne Laserscanning Data in a TIN Structure." *International Archives of Photogrammetry and Remote Sensing, Vol. XXXIII, Part B3, Amsterdam*. CDROM (2000).
- McIntosh, K., Krupnik, A., Schenk, A. "Improvement of Automatic DSM Generation over Urban Areas Using Airborne Laser Scanner Data." *International Archives of Photogrammetry and Remote Sensing, Vol. XXXIII, Part B3, Amsterdam*. CDROM (2000).

- Morin, K., El-Sheimy, N. (1), "A comparison of Airborne Laser Scanning Adjustment Methods.", *ISPRS WGII/2 Three-Dimensional Mapping from InSAR and LIDAR Workshop Proceedings*, Banff, Alberta, Canada, July 11-13, 2001.
- Morin, K., El-Sheimy, N. (2), "The Effects of Residual Errors in Airborne Laser Scanning Terrain Data on Ortho-Rectified Imagery.", *Optical 3D Measurement Techniques V Proceedings*, Vienna, Oct. 1-4, 2001.
- Morin, K., El-Sheimy, N., "Post-mission Adjustment Methods of Airborne Laser Scanning Data." *Proceedings of the FIG/ASPRS Annual Conference*. Washington D.C., Apr. 2002 (CDROM).
- Mostafa, M., Hutton, J. "Direct Positioning and Orientation Systems. How do they Work? What is the Attainable Accuracy?." *International Archives of Photogrammetry and Remote Sensing, Vol. XXXIII, Part B3, Amsterdam*. CDROM (2000).
- Murakami, H., Nakagawa, K., et al. "Change detection of buildings using an airborne laser scanner." *ISPRS Journal of Photogrammetry and Remote Sensing, Vol. 54*. Elsevier (1999): 148-152.
- Murtagh, J., Foote, M. "A Practical Application of Laserscanning Data in the Insurance Industry." *Proceedings of the Fourth International Airborne Remote Sensing Conference and Exhibition*. Canadian Symposium on Remote Sensing, Ottawa, Canada (1999): I 582-588.
- Niemann, O.K. "Development of automated techniques to extract, generalize, and access geospatial information from hyperspectral remotely sensed data." *Oral Presentation, GEOIDE Annual Conference*. Toronto (2002).
- Optech, 2002. "Optech – Laser Based Ranging, Mapping and Detection Systems". *Optech Incorporated*. URL <http://www.optech.on.ca>.
- Pereira, L.M., Wicherson, R.J. "Suitability of laser data for deriving geographical information. A case study in the context of management of fluvial zones." *ISPRS Journal of Photogrammetry and Remote Sensing, Vol. 54*. Elsevier (1999): 105-114.
- Pfeifer, N., Kostli, A., Kraus, K. "Interpolation of Laser Scanner Data - Implementation and First Results." *Proceeding of the ISPRS Conference, Part 3/1, Jul 6-10, Columbus, Ohio*. (1998): 153-159.
- Popescu, S., Wynne, R. "Estimating Tree Heights and Stand Density with High-Performance LIDAR: Initial Results from a case study in the Virginia Piedmont." *International Archives of Photogrammetry and Remote Sensing, Vol. XXXIII, Part B3, Amsterdam*. CDROM (2000).

- Roper, W. "High Resolution Terrain Characterization with Lidar and Radar Sensors." *Proceedings of the Fourth International Airborne Remote Sensing Conference and Exhibition*. Canadian Symposium on Remote Sensing, Ottawa, Canada (1999): I 885-891.
- Samberg, A., Hyypya, J. "Assessing Tree Attributes from the Laser Scanner Data: The High-Scan Case." *Proceedings of the Fourth International Airborne Remote Sensing Conference and Exhibition*. Canadian Symposium on Remote Sensing, Ottawa, Canada (1999): II 251-258.
- Schickler, W., Thorpe, A. "Surface Estimation Based on LIDAR." *Proceedings of the ASPRS Annual Convention, St. Louis, USA*. ASPRS, CDROM (2001).
- Schwarz, K.P. *ENGO 421: Fundamentals of Geodesy Lecture Notes*. Calgary: The University of Calgary, Department of Geomatics Engineering, 1996.
- Schwarz, K.P., Wei, M., "INS/GPS Integration for Geodetic Applications: Lecture Notes ENGO 623." *Department of Geomatics Engineering, University of Calgary*. May 2000.
- Snyder, J. *Map Projections – A Working Manual*. U.S. Geological Survey Professional Paper 1395. Washington: United States Government Printing Office, 1987.
- Strang, G., K. Borre. *Linear algebra, geodesy, and GPS*. Wellesly: Wellesley-Cambridge Press, 1997.
- Suson, D. "Fibre Optics: Gradient Index Optics." <http://physics.tamuk.edu/~suson/html/4323/fiber.html>. Internet website. Visited: Nov 2002.
- Terrasolid, "Terrasolid Inc. Homepage." <http://www.terrasolid.fi>. Internet website. Visited: Sep. 2002.
- Toth, C., Berning, S., Leonard, J., Grejner-Brzezinska, D. "Integration of LIDAR Data with Simultaneously Acquired Digital Imagery." *Proceedings of the ASPRS Annual Convention, St. Louis, USA*. ASPRS, CDROM (2001).
- Vaughn, C.R., Bufton, J.L, Krabill, W.B., Rabine, D. "Georeferencing of airborne laser altimeter measurements." *International Journal of Remote Sensing, Vol. 17, No. 11*. (1996): 2185-2200.
- Vosselman, G. "Slope Based Filtering of Laser Altimetry Data." *International Archives of Photogrammetry and Remote Sensing, Vol. XXXIII, Part B3, Amsterdam*. CDROM (2000).

- Vosselman, G., Mass, H-G. "Adjustment and Filtering of Raw Laser Altimetry Data." *International Archives of Photogrammetry and Remote Sensing, Vol. XXXIII, Part B3, Amsterdam*. CDROM (2000).
- Wang, Y., Mercer, B., Tao, V., Sharma, J., Crawford, S. "Automatic Generation of Bald Earth Digital Elevation Models from Digital Surface Models Created Using Airborne IFSAR." *Proceedings of the ASPRS Annual Convention, St. Louis, USA*. CDROM (2001).
- Wehr, A., Lohr, U. "Airborne laser scanning - an introduction and overview." *ISPRS Journal of Photogrammetry & Remote Sensing, v54*. Elsevier (1999): 68-82.
- Weishampel, J., Blair, J., et al. "Volumetric lidar return patterns from an old-growth tropical rainforest canopy." *International Journal of Remote Sensing, Vol. 21, No. 2*. (2000): 409-415.
- Williams, T. *The History of Invention: From Stone Axes to Silicon Chips*. Slovenia: Macdonald & Co, 1987.
- Williamson, R., Baker, J. "Lending a helping hand: Using remote sensing to support the response and recovery operations at the World Trade Centre." *Photogrammetric Engineering and Remote Sensing*. ASPRS, (Sep. 2002): 870-875.
- Ziegler, M., Wimmer, A., Wack, R. "DTM generation by means of airborne laser scanning - an advanced method for forested areas." *Proceedings of the Optical 3D Measurement Techniques V, Oct 1-4*. Vienna, Austria (2001): 97-102.

Appendix A

Histogram Analysis Details

Histogram analysis is used in this project to visualize the distribution of surface differences between ALS flight lines, and to determine whether the differences following a normal (Gaussian) distribution. If the differences are caused purely by random observation error, then the distribution will be normal. Additional unmodeled errors can cause the shape to vary.

The goodness of fit test used in this project is the chi-squared test. This test computes a test statistic based on the observed and expected frequencies of a normal probability density function, i.e.,

$$y = \sum_{i=1}^k \frac{(o_i - e_i)^2}{e_i}$$

where,

o_i is the observed value

e_i is the expected value

k is the number of histogram bins with accumulations >5

The normal distribution is defined by a mean and a variance; but in this project, the sample mean l and the sample variance s^2 of the elevation differences are used. This reduces the degrees of freedom by 2.

The statistic y is then tested against the chi-squared distribution with ν degrees of freedom and a specific confidence interval α (Krakiwsky and Abousalem 1995),

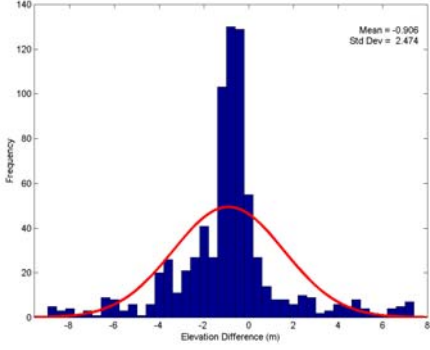
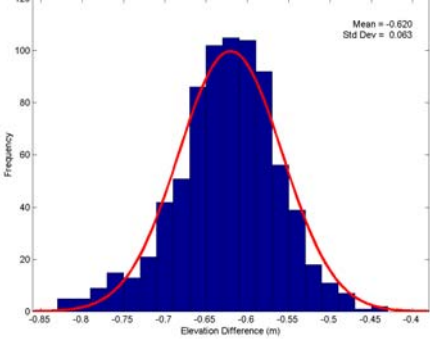
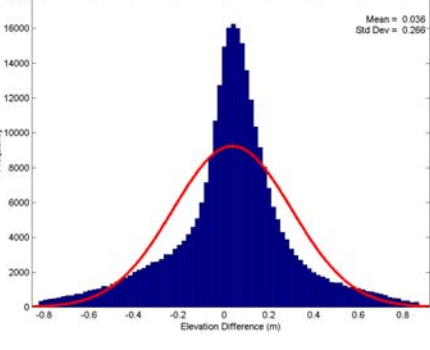
$$0 < y < \xi_{\chi^2_{\nu, 1-\alpha}}$$

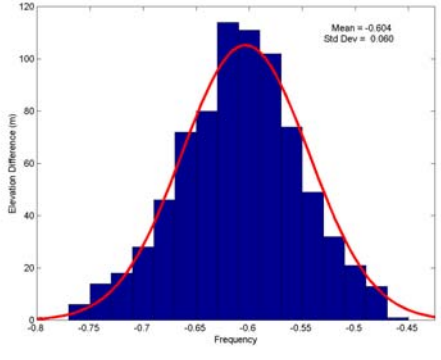
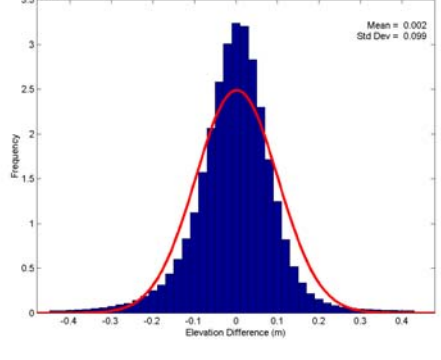
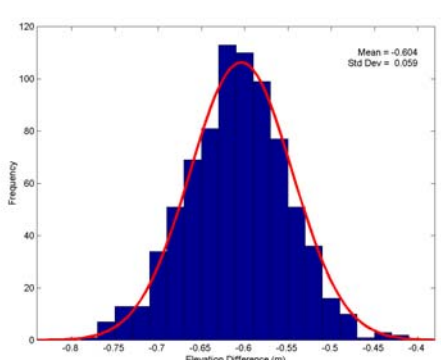
where,

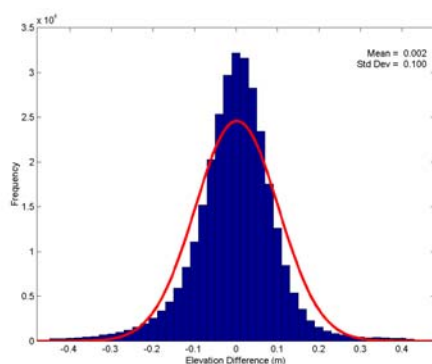
ν is the number of histogram bins minus 3 (loss of freedom for sample mean, sample variance and test statistic)

For the following histograms, variables are defined as:

l	sample mean (m)
s	sample standard deviation (m)
n	sample size
$nbins$	number of histogram bins
$binWidth$	width of each histogram bin (m)
$y-stat$	test statistic
dof	degrees of freedom
$chi2conf$	the chi-squared confidence interval that equals $y-stat$

	<p><u>Pre-Analysis Control Point Differences</u></p> <p>interval: -9.089 - 7.299</p> <p>$l = -0.906$ $s = 2.474$</p> <p>$n = 769$ $dof = 22$</p> <p>$nbins = 43$ $binWidth = 0.400$</p> <p>$y\text{-stat} = 659.7052$ $chi2\ conf = 0.000$</p>
	<p><u>Angle Only Control Point Differences</u></p> <p>interval: -0.835 - -0.408</p> <p>$l = -0.620$ $s = 0.063$</p> <p>$n = 784$ $dof = 13$</p> <p>$nbins = 23$ $binWidth = 0.020$</p> <p>$y\text{-stat} = 26.5180$ $chi2\ conf = 0.014$</p>
	<p><u>Angle Only - Strip Differences</u></p> <p>interval: -0.820 - 0.890</p> <p>$l = 0.036$ $s = 0.266$</p> <p>$n = 307614$ $dof = 83$</p> <p>$nbins = 88$ $binWidth = 0.020$</p> <p>$y\text{-stat} = 67905.176$ $chi2\ conf = 0.000$</p>

	<p><u>Torsion Control Point Differences</u></p> <p>interval: -0.800 - -0.407</p> <p>$l = -0.604$ $s = 0.059$</p> <p>$n = 787$ $dof = 12$</p> <p>$nbins = 22$ $binWidth = 0.020$</p> <p>$y\text{-stat} = 19.1963$ $chi2\ conf = 0.084$</p>
	<p><u>Torsion Strip Differences</u></p> <p>interval: -0.443 - 0.444</p> <p>$l = 0.002$ $s = 0.099$</p> <p>$n = 308897$ $dof = 42$</p> <p>$nbins = 47$ $binWidth = 0.020$</p> <p>$y\text{-stat} = 198199.77$ $chi2\ conf = 0.000$</p>
	<p><u>Combined Solution - Control Point Differences</u></p> <p>interval: -0.800 - -0.407</p> <p>$l = -0.604$ $s = 0.059$</p> <p>$n = 787$ $dof = 12$</p> <p>$nbins = 22$ $binWidth = 0.020$</p> <p>$y\text{-stat} = 15.6278$ $chi2\ conf = 0.209$</p>



Combined Solution – Strip Differences

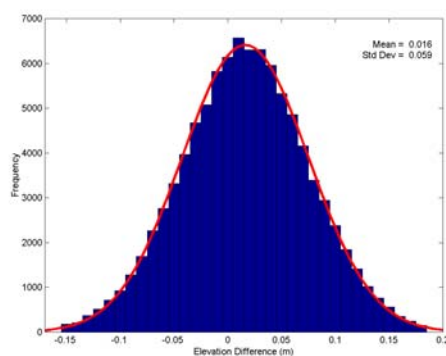
interval: -0.446 - 0.447

$l = 0.002$ $s = 0.100$

$n = 308795$ $dof = 42$

$nbins = 47$ $binWidth = 0.020$

$y\text{-stat} = 170033.45$ $chi2\ conf = 0.000$



Combined Solution – Flat Region Strip Differences

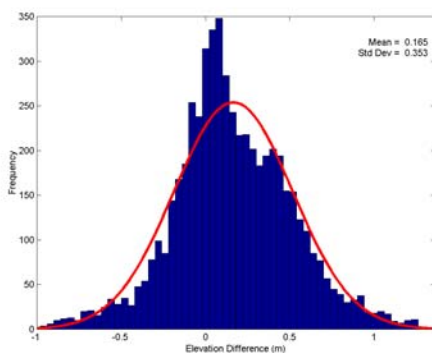
interval: -0.153 - 0.185

$l = 0.016$ $s = 0.059$

$n = 94503$ $dof = 31$

$nbins = 36$ $binWidth = 0.010$

$y\text{-stat} = 149.6162$ $chi2\ conf = 0.000$



Combined Solution – Sloped Region Strip Differences

interval: -0.959 - 1.311

$l = 0.165$ $s = 0.353$

$n = 5609$ $dof = 52$

$nbins = 58$ $binWidth = 0.040$

$y\text{-stat} = 366.0863$ $chi2\ conf = 0.000$